Interface investigation between hydrocarbon and hydrocarbon-like molecules on semiconductor surfaces.

Dissertation

zur Erlangung des Doktorgrades der Naturwissenschaften

der Fakultät Physik der Technischen Universität Dortmund

vorgelegt von

Daniel Christopher Weier

- Januar 2010 -

Contents

Parts of this work have already been published in:

D. Weier, C.R. Flüchter, A. deSiervo, M. Schürmann, S. Dreiner, U. Berges, M.F. Carazzolle, A. Pancotti, R. Landers, G.G. Kleiman, and C. Westphal, *Photoelectron spectroscopy (XPS) and phototelectron diffraction (XPD) studies on the system hafnium silicide and hafnium oxide on Si(100)*, Mater. Sci. Semicond. Process. **9** (2006), 1055

D. Weier, T. Lühr, A. Beimborn, F. Schönbohm, S. Döring, U. Berges, and C. Westphal, *Photoelectron spectroscopy (XPS) and photoelectron diffraction (XPD) studies on the local adsorption of cyclopentene on Si(100)*, Surf. Sci. (2009), accepted for publication

D. Weier, T. Lühr, A. Beimborn, F. Schönbohm, S. Döring, U. Berges, and C. Westphal, *Structural analysis of the system pyridine/Si(100) by means of photoelectron spectroscopy and photoelectron diffraction*, Phys. Rev. B (2009), submitted

Acronyms

AES ..... Auger Electron Spectroscopy

AFM ..... Atomic Force Microscopy

CEM ..... Channel Electron Multiplier

DELTA ..... Dortmunder Elektronen Speicherring Anlage

DFT ..... Density Functional Theory

EXAFS ..... Extended X-ray Absorption Fine Structure

FET ..... Field Effect Transistor

GA ..... Genetic Algorithm

GCA ..... Gradual Channel Approximation

HE ..... High Energy

HOMO ..... Highest Occupied Molecular Orbital

HREELS ..... High-Resolution Electron Energy Loss Spectroscopy

IL ..... Inter Layer

LE ..... Low Energy

LEED ..... Low Energy Electron Diffraction

LUMO ..... Lowest Unoccupied Molecular Orbital

MOSFET ..... Metal-Oxide-Semiconductor Field Effect Transistor

PE ..... Photoelectron

PED ..... Photoelectron Diffraction

PES ..... Photoelectron Spectroscopy

RT ..... Room Temperature

SEM ..... Scanning Electron Microscopy

STM ..... Scanning Tunneling Microscopy

TEC ..... Total Energy Calculation

TDS ..... Thermal Desorption Spectrometry

UHV ..... Ultrahigh Vacuum

UPS ..... Ultraviolet Photoelectron Spectroscopy

XPD ..... X-Ray Photoelectron Diffraction

XPS ..... X-Ray Photoelectron Spectroscopy

XRF ..... X-Ray Fluorescence

1 Introduction

Due to the micro-technologic revolution switching elements became smaller and smaller the last 60 years. The number of electronic components per square unit area doubled every 18 months resulting in an exponential increase of the density of logical elements on a silicon microchip. This exponential growth was predicted by Gordon Moore in the year 1965. Nowadays microcontroller can be found in almost every electronic device including automobiles and home appliances, to means of communication and equipment in our doctors office [1].

Up to the present day the logical elements have been downsized thus far, that the switching elements themselves are in the magnitude of molecules. In the context of the in 1999 published Technology Roadmap for semiconductors [2] it was proposed that the switching elements would reach a lateral size of only 35 nm in 2014. However, this magnitude is already reached nowadays. On the basis of this magnitudes it is easily predictable that the future of switching devices will be in the area of organic molecules, because the order of magnitude of organic molecules is already reached.

The combination of an organic molecule with a semiconductor surface is genereally referred to as a hybrid device. These hybrid devices are of great interest as promising candidates for future developments in various areas of research. Possible applications are in the field of biotechnology, nanoelectronics, high density data storage, and medical diagnostics. First applications of hybrid devices have already been realized in light emitting diodes and field effect transistors [3,4]. However, for all already known and possible future applications very important factors are the properties and quality of the interface and the adsorption sites. A well defined structure in this region is essential in order to guarantee and improve the stability and functionality of hybrid devices.

Among the organic molecules there is a wide range of possible candidates available for these kind of devices, because approx. 95% of all known chemical components are in the organic regime [5]. On the substrate side of the hybrid devices silicon is by far

the most important substrate in the semiconductor industry. One of the main reasons is the high pureness and availability in industry. Especially the Si(100) surface is preferred for these applications. In order to investigate the special characteristics at the interface inside those hybrid devices its very important to understand the interaction between the organic molecules and the semiconductor firstly. For this reason we studied small organic ring molecules as a fundamental research for hybrid device interfaces. In this study a pure hydrocarbon molecule (cyclopentene) as well as an organic ring molecule with functionalized atoms (pyridine) were investigated. For these molecules different investigations have been performed, but none of this methods could excess the structure of the important interface.

For the studies of interfaces and structures of adsorbates at their bonding sites the methods of photoelectron spectroscopy(PES) and x-ray photoelectron diffraction (XPD) have been proved to be very effective [6–8]. For this reason these methods are chosen to study the surface and interface between the molecules and the semiconductor substrate. A detailed discussion on the methods and its advantages in comparison to real space methods (eg. scanning tunneling microscopy (STM)) will be discussed in Chap. 2.2. The drawback of this method regarding the time effort which is necessary to access the final structure model will also be discussed.

In detail, in the second chapter of this work the theory of the used methods will be presented. This includes an overview of the photoelectric effect (PE) and its application in photoelectron spectroscopy. The different signal types of photoelectron spectroscopy and their line shapes are explained. Finally, the theory of the x-ray photoelectron diffraction (XPD) and its interpretation is introduced.

The third chapter provides a detailed look on the computational physics which are necessary in the simulation of diffraction patterns. The simulation program MSPHD [9] is introduced and its method in calculating diffraction patterns is discussed. Afterwards, the used genetic algorithms and its probabilistic evaluation is discussed. The implementation of the algorithm to the studied system as well as the analysis of many different possbible structures within the simulations was one main part of this work.

The fourth chapter gives an overview on the experimental setup used in this work. This includes the ultra high vacuum (UHV) chamber as well as the detector unit and analytical components at the chamber. Additionally, a short overview of the setup of beamline 11 is given.

Starting with the fifth chapter the results obtained from the measurements, fitting procedures and simulation calculations are discussed. In the first part the role of radiation damage to molecules due to synchrotron light and solutions to reduce the radiation damage are introduced. Furthermore, a detailed overview of the properties of the clean silicon(100) surface is given and the general adsorption behavior of molecules to this surface is discussed. In chapter 5.4 and chapter 5.5 the results obtained for cyclopentene and pyridine on Si(100) by XPS and XPD are described in detail. This study allowed us to determine geometric parameters of this systems for the first time, including atomic distances and tilting angles between the different layers. These results allowed us to present a coherent picture of this system including adsorption sites and structural parameters.

In the sixth chapter the new findings regarding the interface and adsorbate structures are summarized and final conclusions are drawn. Additionally, an outlook regarding a possible continuation of this work at other molecules or multi-layer molecules is introduced.

2 Theoretical Part

2.1 Basics of Photoemission

In this work thin molecular hydrocarbon films on silicon have been prepared and studied using XPS (X-Ray Photoelectron Spectroscopy) and XPD (X-Ray Photoelectron Diffraction). The basic process for both of the techniques is the photoelectric effect first observed by H. Hertz. In a study about the expansion of electric waves in a conductor he realized that the number of sparks in one electric discharge could be increased when irradiating the cathode with ultraviolet light [10]. This is called photoelectric effect now. In 1905, this effect was theoretically described by Einstein [11] and in 1921, he received the Nobel Prize for this work. In his theory, he assigned particle characteristics to light, so that every particle (photon) holds the energy $h\nu$. If this photon reacts with a metal surface, all of the energy is transferred to an electron. If the transferred energy is higher than the sum of the binding energy E_B and the work function ϕ, the electron can leave the surface holding the kinetic energyE_kin [11]:

$$E_{kin} = h\nu - E_B - \phi \tag{2.1}$$

,

with E_{kin} as the kinetic energy of the electron, $h\nu$ as the energy of the incoming light, E_B as the binding energy of the electron inside the material and ϕ as the work function.

Einsteins equation 2.1 offers a direct connection between the kinetic energy of the electrons and the energy of the bonding states if the energy of the incoming light is known. This relationship is taken advantage of in photoelectron spectroscopy.

2.2 Photoelectron Spectroscopy

In photoelectron spectroscopy, the intensity of escaping electrons is depending on the kinetic energy. Plotting these two values together leads to a photoelectron spectrum [12], which contains information about the analyzed bonding states inside the surface. In general, photoelectron spectroscopy is roughly divided into two types:

- **UPS**: UPS is the abbreviation for Ultraviolet Photoelectron Spectroscopy and denotes photoelectron spectroscopy where valence bands of atoms are studied. The energy of the incoming light is typically below hν = 100 eV. Usually, a gas discharge lamp or the synchrotron is used as a source for the incoming photons. In contrast to synchrotron light, gas discharge lamps deliver very high flux and a very good energy resolution. Another advantage over the synchrotron is the permanent availability of the photon source. A big disadvantage for the gas discharge lamp is their inability to vary the energy of the incoming light. If this is necessary for the investigation, synchrotron light is required.
- **XPS**: XPS is the abbreviation for (X-Ray Photoelectron Spectroscopy) and is used to study the core levels of atoms. The energy of the incoming light is typically above hν = 100 eV, because the electrons in the core levels of the atoms are bonded more strongly than the valence band electrons. Photon sources for this type of spectroscopy are x-ray tubes and synchrotron light. The synchrotron light is the preferred source, because of its variable energy and much higher photon flux. The advantage of the x-ray-tube is its permanent availability, whereas the availability of synchrotron light is limited. The energy range of the XPS allows the study of the core levels of atoms, because each of the atoms have a specific core level binding energy and it is therefore possible to obtain a quantitative information about the composition of the elements at the surface.

In both processes, an electron is removed from its binding state in the surface, and a hole is left. This hole is refilled with an electron from a higher atomic shell. During the transition from the energy state j to the energy state i, a photon is emitted. The energy $h\nu$ of the emitted photon is given as the energy difference between the two binding states.

$$h\nu = E_i - E_j \tag{2.2}$$

This photon can either leave the surface as fluorescent radiation (cf. Fig. 2.1 (b)) or release another electron from a higher atomic shell. The second process is called the Auger-effect (cf. Fig. 2.1 (c)) and occurs due to coulomb-interaction inside the atom [13]. Elements with an atomic number $Z < 30$ favor the Auger-effect, whereas elements with an atomic number $Z > 60$ have a significantly higher probability for fluorescent radiation [14].

Photons from fluorescent radiation are not visible in XPS, because it only detects electrons. However, Auger-electrons are visible in the XPS spectra. The main difference between the core level emitted electrons shown in Fig. 2.1 (b) and the Auger-electrons is visible when the energy of the incoming light is varied. A variation of the photon energy of the incoming light varies the position of the core level signal as explained in equation 2.1, but does not change the position of Auger-signals. This needs to be taken into consideration for measurements when the energy of the incoming light is chosen.

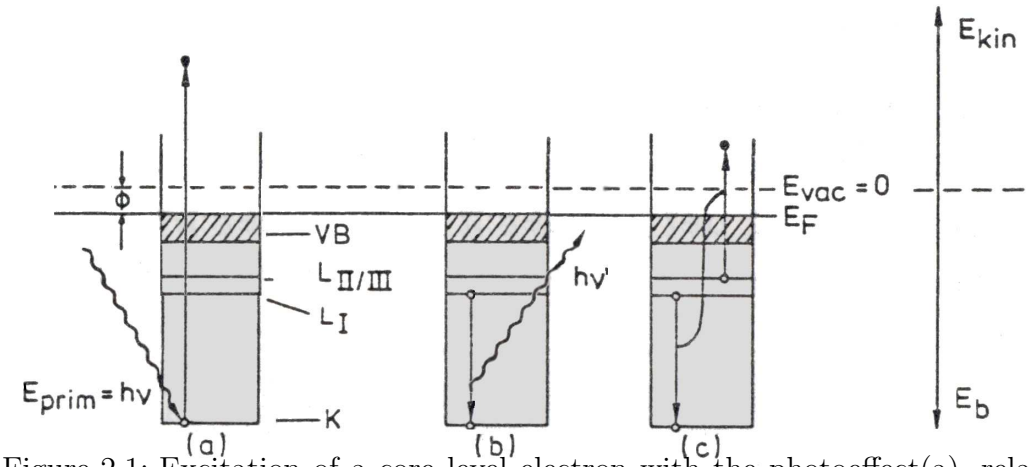

Figure 2.1: Excitation of a core level electron with the photoeffect(a), relaxation of the systems by emission of fluorescent radiation(b), and relaxation of the systems by the Auger-effect (c) [12]

Fig. 2.2 shows a typical XPS spectrum obtained from a metal surface. In XPS spectra the binding energy or kinetic energy is plotted against the count rate. The spectrum contains different features and some of them can be easily understood with the core level emission and the Auger-effect explained above. However, there are additional features visible in the spectrum, that cannot be understood by these two effects. The interpretation and understanding of these additional signals is crucial to avoid mistakenly using them as core level signals in surface level analysis. The additional signals in Fig. 2.2 are due to energy loss, plasmons and shake-ups, which should be explained below:

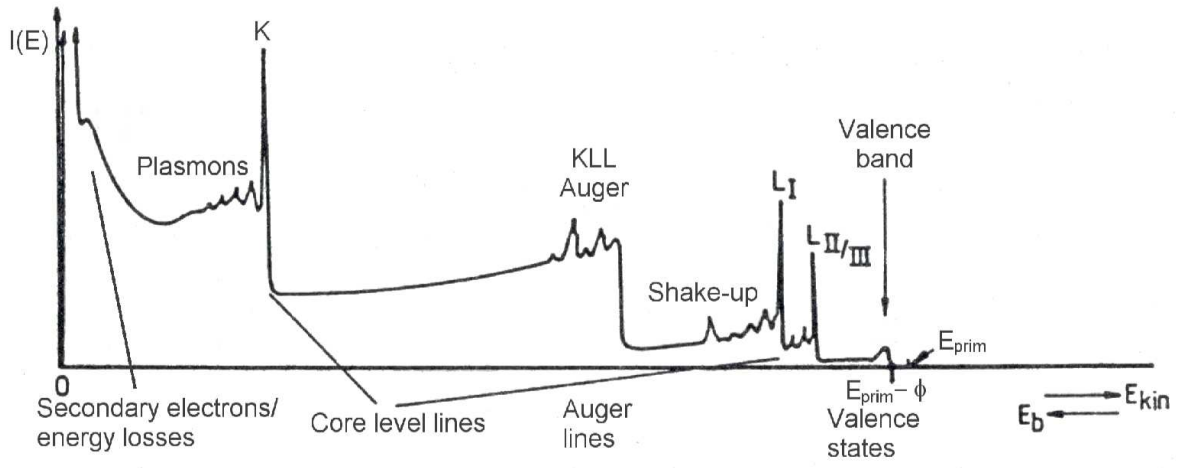

Figure 2.2: Typical XPS spectrum of a metal surface. The different signals included in the spectrum are explained in the text.

- **energy loss**: In the low energy range of the spectrum, a strong increase in intensity is observed. This observation can be explained by two different effects. One effect is due to to secondary electrons. These electrons are emitted from low bonded energy states, for example the valence band, by other electrons that are leaving the surface. The second effect results from inelastically scattered electrons which prevents an energy loss during this process.
- **plasmons**: Plasmons are collective excitations of electrons in metals and semiconductors. The excitation can occur because of two effects. Firstly, during the photoemission process, the positive core hole is refilled from the fermi-sea instead of the atom itself. These plasmons are called intrinsic plasmons. Secondly, an electron leaving the surface can excite plasmons inside the bulk or the surface. These kinds of plasmons are called extrinsic plasmons. During this procedure, the electrons lose different amounts of energy, which results in asymmetric line shapes of the plasmon signal in the XPS spectra.
- **shake-up**: In contrast to the plasmon, a shake-up process reflects the excitation of one or more electrons. The photoelectrons escape from the atom by changing the ground state of the system. This process is not yet completely understood.

If these effects are considered carefully, and if the elements in a surface are not bonded to other elements it is possible to obtain their position in the XPS spectra directly from Einstein's equation (Eq. 2.1). With the photon energy $h\nu$ of the incoming light and the kinetic energy of the electrons, it is possible to determine the binding energy of the elements from the XPS spectra.

Due to some limitation in the equipment for XPS analysis (for example the work function of the detector), it is generally very challenging to obtain an absolute value for the binding energies. Therefore, the binding energy position of the different features is usually given with respect to well known energy levels.

2.2.1 Chemical Shift

If the analyzed system contains elements that are chemically bonded to other elements inside the surface, a chemical shift of the XPS signal occurs. One of the most famous examples is presented in Fig. 2.3:

In the case of ethyl-trifluoracetate all the carbon atoms are bonded to different elements. Each of the elements sustains a different electronegativity, and therefore the value of the chemical shift added to the C 1s signal differs significantly. In Fig. 2.3, each of the different signals can be clearly separated from each other. Unfortunately, for typical samples studied with XPS, the chemical shift is much lower than in Fig. 2.3. Fig. 2.4 shows a photoelectron spectrum of oxidized silicon that includes the different oxidation states within the surface. In addition to the bulk component (Si^0), several other chemically shifted components are observed. The amount of the chemical shift depends on the number of bindings to oxygen atoms. If just the line shapes of the spectra in Fig. 2.3 and Fig. 2.4 are compared, it is clearly visible that the position of the different components in spectrum 2.4 cannot be separated as easily as in spectrum 2.3. The separation of the different components is limited by the combination of the chemical shift and the full width at half maximum of each component. If the full width at half maximum is high and the chemical shift is small an overlap of the different signals is observed in the XPS spectra. A fitting procedure of the data is required for a decomposition of those signals. Possible functions for carrying out fitting procedures are described in section 2.2.2.

2.2.2 Line Shapes

The intrinsic line width of photoelectron signals is at first determined by the lifetime of the electron systems excitation and thus the uncertainty relation. The shape of such a peak can be expressed as a Lorentzian function:

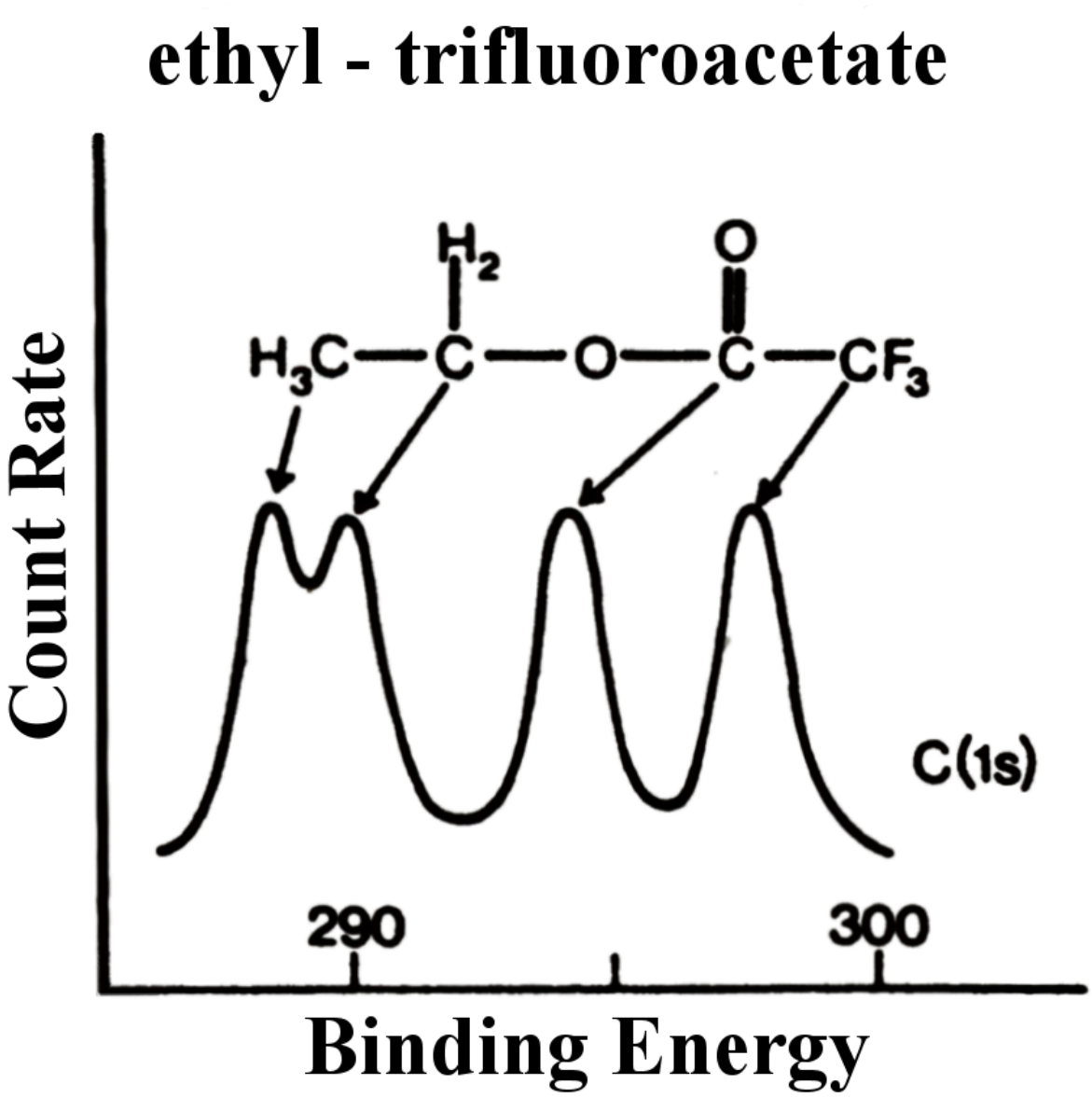

Figure 2.3: Chemically shifted C 1s signal in ethyl-trifluoracetate. Due to the strong chemical shift this molecule is a standard example for explaining the effect [15].

$$L(x) = \frac{1}{\pi} \frac{0.5 w_L}{(x - x_c)^2 + (0.5 w_L)^2} \tag{2.3}$$

In addition to the inherent line width, other phenomena can influence the resulting peak shape. Moreover, the peak can be broadened by the limited energy resolution of the electron analyzer. Most extrinsic effects add a Gaussian energy distribution of the form:

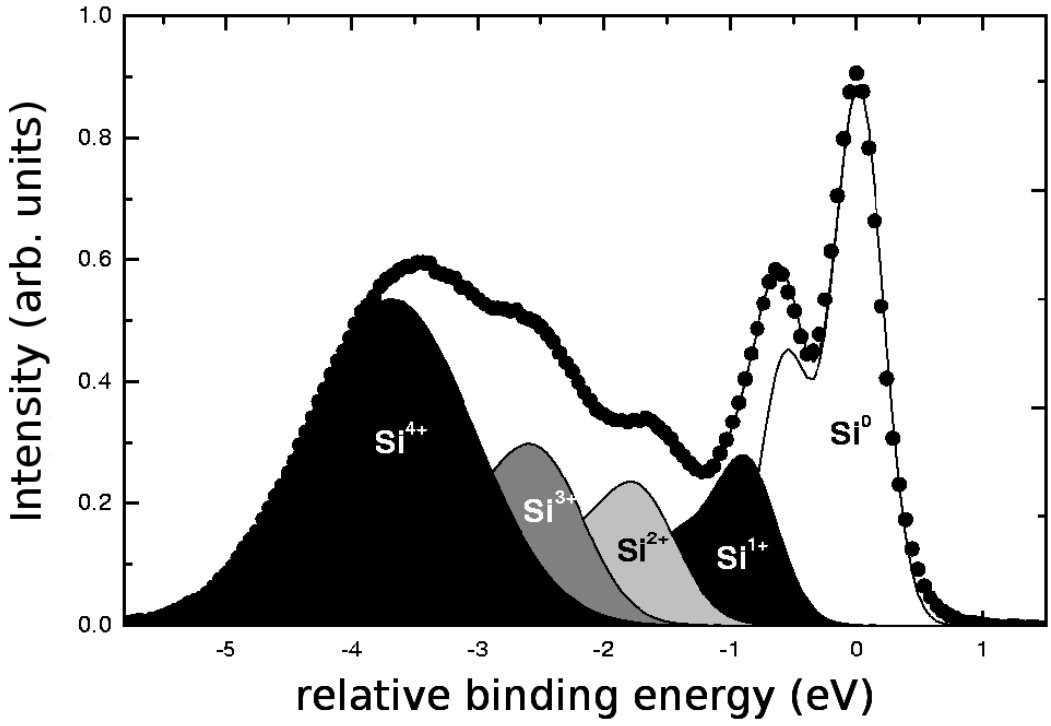

Figure 2.4: Photoelectron spectrum of the oxidized silicon(111) surface. The line shape of the spectrum indicates different components, which belong to different oxidation states.

$$G(x) = A \cdot exp\left(-\frac{(x - x_c)^2}{2w_G^2}\right) \tag{2.4}$$

A combination of these effects results in the deconvolution of the functions:

$$V(t) = \int_{-\infty}^{t} L(x)G(x - t)dx \tag{2.5}$$

This function is called a Voigt-profile. This profile is mainly used for fitting procedures in XPS analysis. However, a direct implementation of Eq. 2.5 is not possible for the fitting procedures. Therefore, numerical formulas have been invented to describe the analytical formula as well as possible. The so-called Pseudo-Voigt-Function used in this work is shown in Eq. 2.6:

$$pV(x) = A\left[\mu\frac{2}{\pi}\frac{w_L}{4(x-x_c)^2+w_L^2} + (1-\mu)\frac{\sqrt{4\ln 2}}{\sqrt{\pi}w_G}\exp\left(-\frac{4\ln 2}{w_G^2}(x-x_c)^2\right)\right] \tag{2.6}$$

For most of the studied surfaces, a fitting procedure using a Gaussian or Voigt-profile is sufficient. In some special cases, additional profiles are needed. One of these examples is the analysis of unsaturated hydrocarbons studied in this work. In the analysis of the carbon 1s signal of unsaturated hydrocarbons, vibrational splittings resulting from the C-H molecular bonds have to be included. The effect of vibrational splittings on the spectroscopic signal was shown both for gaseous [16–19] and adsorbed molecules [20, 21].

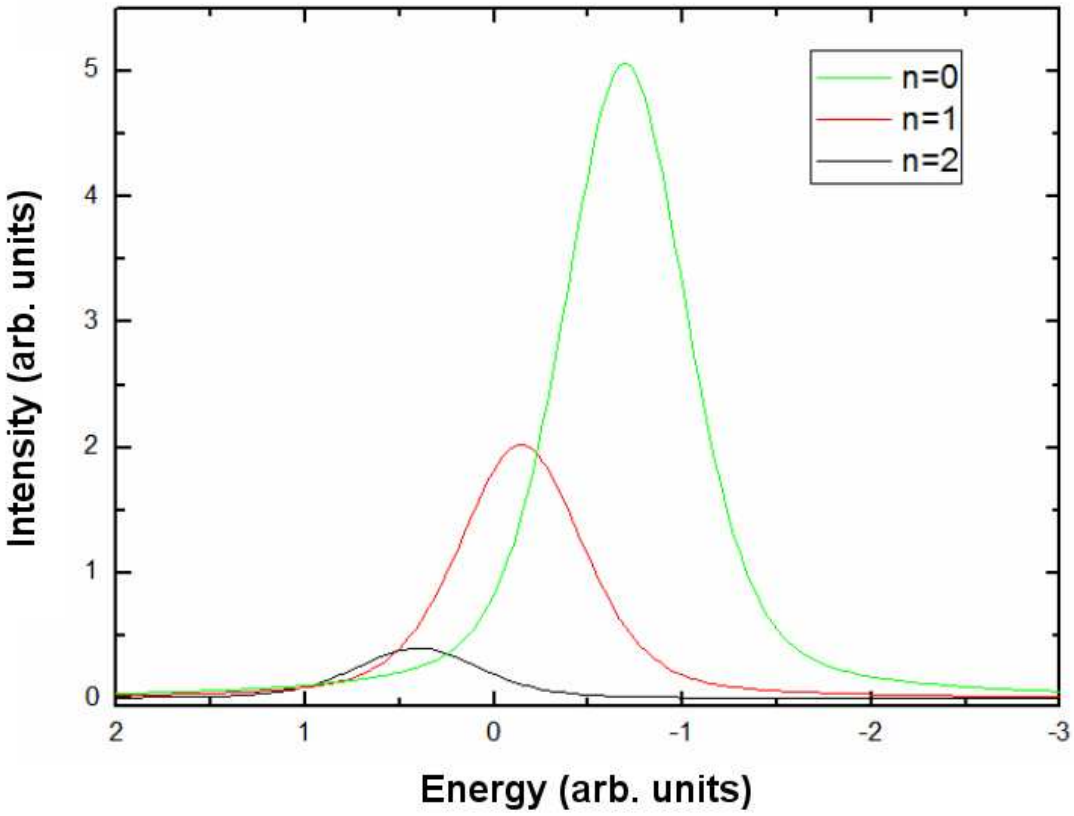

Figure 2.5: Examples for shifted Voigt-Profiles as explained in the text.

An accepted argumentation explaining this effect in XPS spectra can be achieved by the application of a linear coupling model where the excitation process is a Frank-Condon process [20]. For the fitting procedure the linear coupling model is realized via a composition of three Voigt functions that are equally spaced by ΔE in energy. The intensity of

each function is given by $I_n = e^{-S}S^n/n!$, where the factor S is defined as $S = \delta^2\mu\omega/2\hbar$ [20] and n=0,1,2. The parameters δ, μ, and ω describe the normal coordinate of the core excitation, the reduced mass, and the vibrational frequency, respectively. As an example for the change in the line shape of the Voigt-Profile, the parameters for n=0,1,2 , S=0.4 and ΔE are presented in Fig. 2.5. In Fig. 2.6, the resulting fitting function is presented as well. Compared to the normal Voigt-Profile on one hand the resulting fitting function has an asymmetric line shape on the left side. Additionally, the maximum of the resulting fitting function is not at the same position as the maximum of the Voigt-Profile.

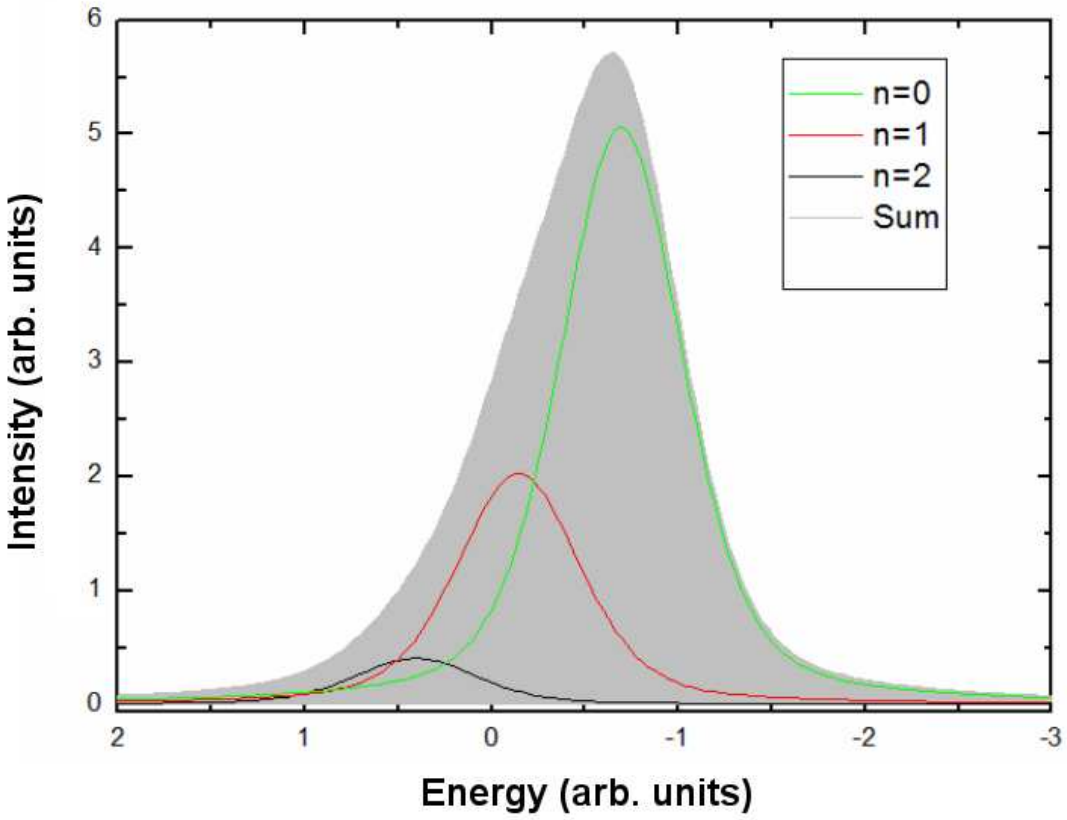

Figure 2.6: Resulting asymmetric fitting function used for the fitting of C1s XPS spectra of hydrocarbons.

2.3 Photoelectron Diffraction

X-Ray Photoelectron Diffraction (XPD) is based on photoelectron spectroscopy. However, XPD takes into account that the electrons emitted by the incoming light have different ways of leaving the surface. Fig. 2.7 schematically shows the different ways for the

electron to leave the surface. As shown in the figure, the electrons may scatter at other atoms inside the bulk or surface. This scattering results in intensity variations in the XPS spectra if the detector is positioned at different observation angles. The reason for these intensity variations is discussed in the follwing.

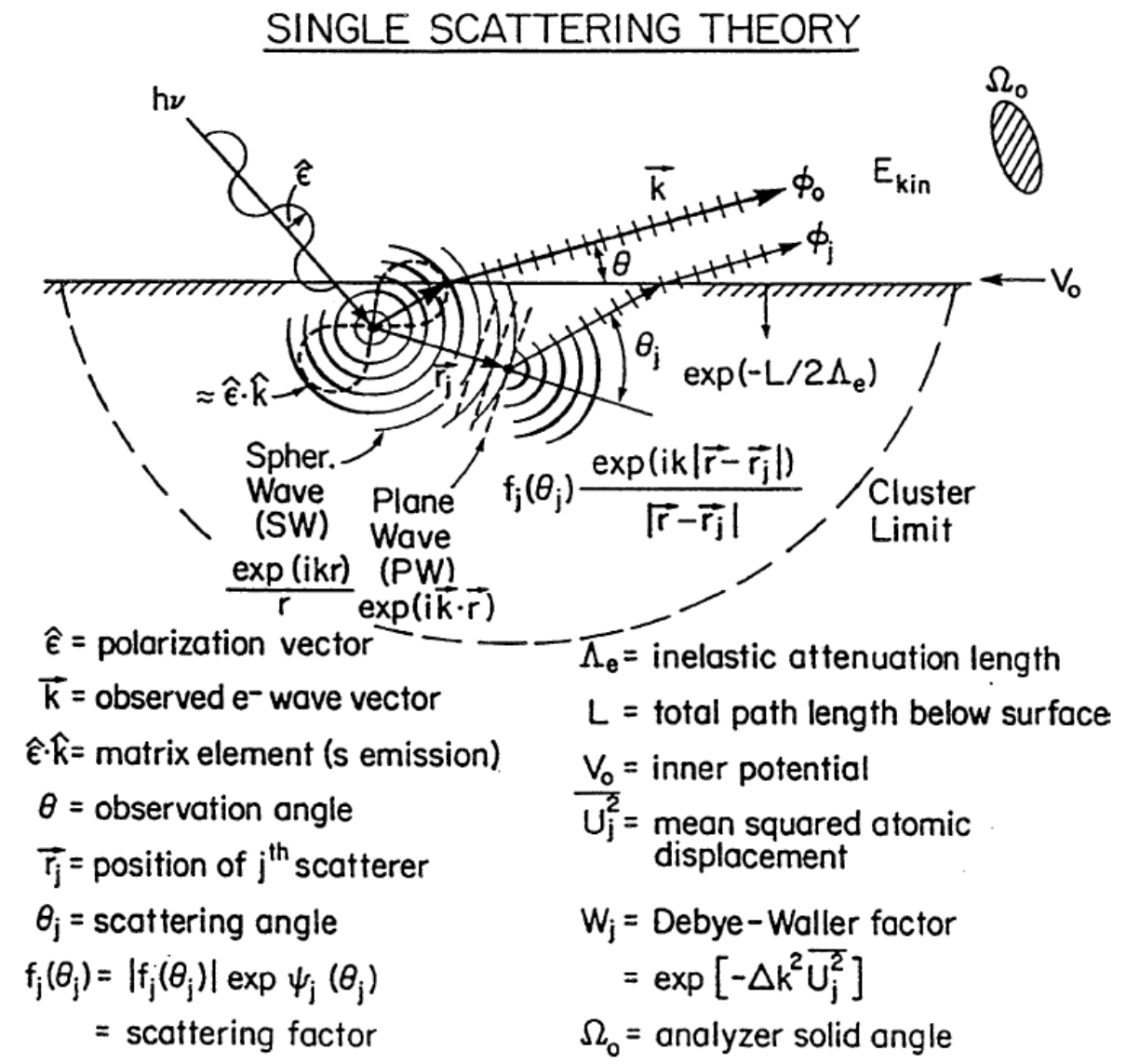

Figure 2.7: Schematic principle of photoelectron diffraction. The different parameters involved in the process are discussed in the text [6].

For consideration of the diffraction effects, only elastically scattered electrons are taken into account, because the inelastically scattered electrons are not coherent to each other and therefore diffraction is not possible. To understand the diffraction effects the electrons are considered as electronic wave functions. The electronic wave functions for the scattered

and unscattered electrons retain an optical path difference after leaving the surface. If the direction of the emission and the energy of the incoming light is fixed, the optical path difference only depends on the position of the detector to the surface and the scattering behavior of the atoms in the substrate.

The first description of the dependence of the intensity on the orientation was given by Siegbahn in 1970, who studied NaCl with a MgK_α X-ray-source [22]. In 1974, Liebsch recognized the possibility of inverting the process and obtaining information about the geometrical surrounding area of the emitting atom from the intensity variation [23]. With these studies, he was the first to provide a theoretical model for photoelectron diffraction.

In the theoretical description of photoelectron diffraction, single and multiple scattering events need to be considered. However, in most cases, a model considering single scattering effects is sufficient. In the single scattering model, it is assumed that the emitted electron only scatters once elastically before leaving the surface. In this case, the resulting wave function $\Psi(\vec{k})$ can be seen as the sum of the unscattered part and the sum of all scattered parts:

$$\psi(\vec{k}) = \psi_0(\vec{k}) + \sum_i \psi_i(\vec{k}) \tag{2.7}$$

$$\vec{k} = \vec{k}(E_{kin}, \Theta, \Phi) \tag{2.8}$$

In the formula ψ_0, ψ_i, $\vec{k}$, θ, and Φ denote the unscattered wave function, the scattered wave functions, the wave vector, the polar angle, and the azimuth angle, respectively. The combination of θ and Φ describes the emission direction of the electrons.

If the distance between the emitter and detector, or rather the scatterer and detector, is large, the resulting spherical wave functions can be considered as a plane wave instead of a spherical wave. For the unscattered wave, the source of the spherical wave is in the center of the emitting atom. With these assumptions, the wave functions gets the form:

$$\Psi_0 \sim \frac{e^{i\vec{k}\vec{r}}}{r} \tag{2.9}$$

The scattered waves are also considered as spherical wave functions, but the center of the wave is in the corresponding scattering atom instead of the emitting atom. This leads to the following equation for the scattered wave function:

$$\Psi_i = \Psi_0 \cdot f_i(\theta_i, k) \cdot \frac{e^{ik\triangle\varphi}}{|\vec{r} - \vec{r_i}|}, \tag{2.10}$$

with θ_i as the scattering angle, $\vec{r_i}$ as the distance between the emitter and the scatterer i, $\triangle\varphi$ the phase shift between Ψ_i and Ψ_0, and $f_i(\theta_i, k)$ as the complex atomic scattering factor.

The phase shift between these two wave functions is composed of the geometrical path difference $\triangle g$ and one component belonging to the scattering atom φ_i:

$$\triangle\varphi = r_i(1 - \cos\theta_i) + \varphi_i(\theta_i, k) \tag{2.11}$$

The wave functions cannot be measured directly, and therefore a formula for the resulting intensity is needed. The intensity of the electrons can be related by squaring the modulus of the amplitude of the electronic wave functions:

$$I(E_{kin}, \theta, \phi) = |\Psi(\vec{k})|^2 = |\Psi_0(\vec{k}) + \sum_i \Psi_i(\vec{k})|^2 \tag{2.12}$$

with $I(E_{kin}, \theta, \phi)$ as the intensity of the overall wave function, $\Psi(\vec{k})$ as the overall wave function, $\Psi_0(\vec{k})$ as the unscattered wave function, and $\Psi_i(\vec{k})$ as the scattered wave for each i.

Within the modulus, all parts are the result of a combination of the unscattered and scattered waves. As a result, the intensity variation is given relative to the interference of both wave functions. Measuring the intensity with this formula allows conclusions to be drawn about the emitting atom's geometric surrounding.

This formula gives a preliminary result for the intensity variation in photoelectron diffraction, but a more detailed analysis of the effect is necessary to achieve the real

intensity variation. Until now only elastically scattered electrons were considered for the resulting intensity. As explained above, inelastic scattered electrons do not contribute to the interference effect itself. However, the overall intensity is lowered by the amount of electrons that are lost due to inelastic scattering. This damping of the intensity can be described by a factor $\exp(-L_{0,i}/2\lambda)$, with $L_{0,i}$ as the length of the pathway the electrons need to travel inside the surface and λ as the inelastic mean free path.

The inelastic mean free path is the mean length that an electron can travel inside the surface between two inelastic scatterings. This parameter is mainly dependent on the kinetic energy of the electrons inside the substrate, as shown by Fig. 2.8. Each point in the figure denotes an atomic element for which the inelastic mean free path was measured. The continuous line in the figure is the so called universal curve of the mean free path. The minimum of the mean free path is around 50 eV, which means that most of the elastic scattered electrons that leaves the surface at this energy are emitted from the uppermost layers. From this follows that XPS measurements concentrating on the surface should choose an energy for the incoming light that results in a kinetic energy of the electrons of about 50 eV.

If this exponential decay of the intensity is taken into account and only emission from a s-state is allowed the final formula for the intensity variation in photoelectron diffraction is [6]:

$$I(\vec{k}) \sim |\hat{\epsilon} \cdot \hat{r} \exp(-\frac{L_0}{2\lambda}) + \sum_i \frac{\hat{\epsilon} \cdot \hat{r}_i}{r_i} |f(\theta_i, r_i)| W_i \cdot \exp(-\frac{L_i}{2\lambda}) \cdot \exp(ikr_i(1 - \cos\theta_i)| \quad (2.13)$$

with W_i as the Debye-Waller-Factor and $\hat{\epsilon}$ as the polarization vector.

This factor considers the effect of lattice vibration on the scattered wave function and therefore the resulting intensity. The Debye-Waller-Factor more specifically is part of the cross section of x-ray, electron or neutron waves that scatters in a crystal. In this case, the Debye-Waller-Factor describes the probability of a coincidence of the initial and final states of the lattice vibration scattering process. As the quantity of lattice vibration depends on the temperature of the crystal, the Debye-Waller-Factor can also be understood as a description of the temperature, dependent on the intensity.

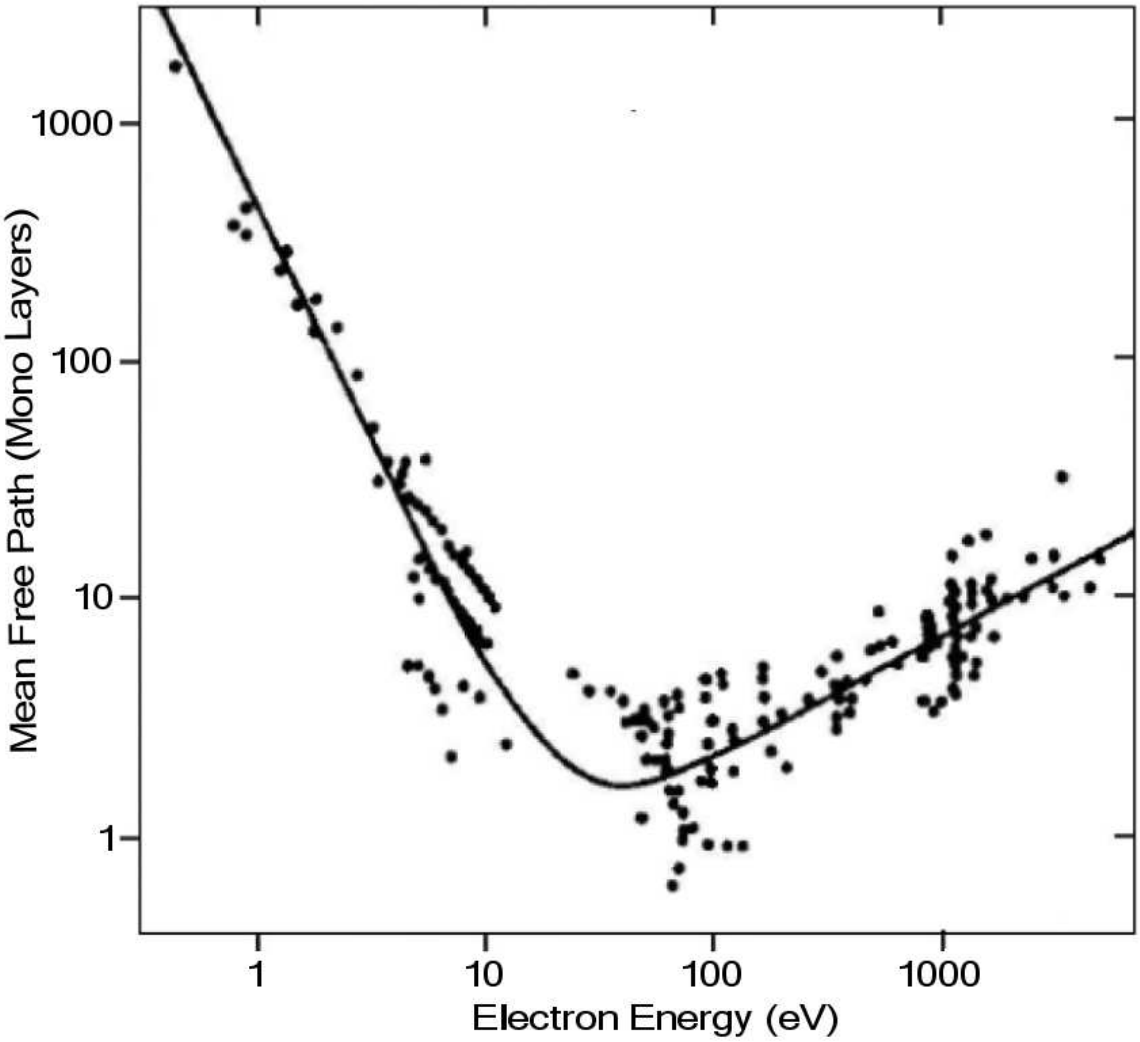

Figure 2.8: Universal curve of the inelastic mean free path of the electrons in the substrate relative to the kinetic energy [24]

The inelastic damping and the $\frac{1}{r^2}$-dependency of the spherical wave results in a strong decrease in intensity with increasing distance to the emitting atom. This means that mainly the atoms next to the emitting atom contribute to the overall intensity. Therefore, photoelectron diffration is very sensitive to the geometrical environment close to the emitting atom.

An additional factor in the intensity in Eq. 2.13 is the complex atomic scattering factor $f(\theta_i, r_i)$. Generally, this factor consists of the atomic scattering factor and a complex phase shift. In the calculation of this factor, the scattering of a plain wave at a circular potential is considered. The resulting Schroedinger-Equation is solved by its decomposition into partial waves [6]. This leads to a strong dependence of the complex atomic scattering

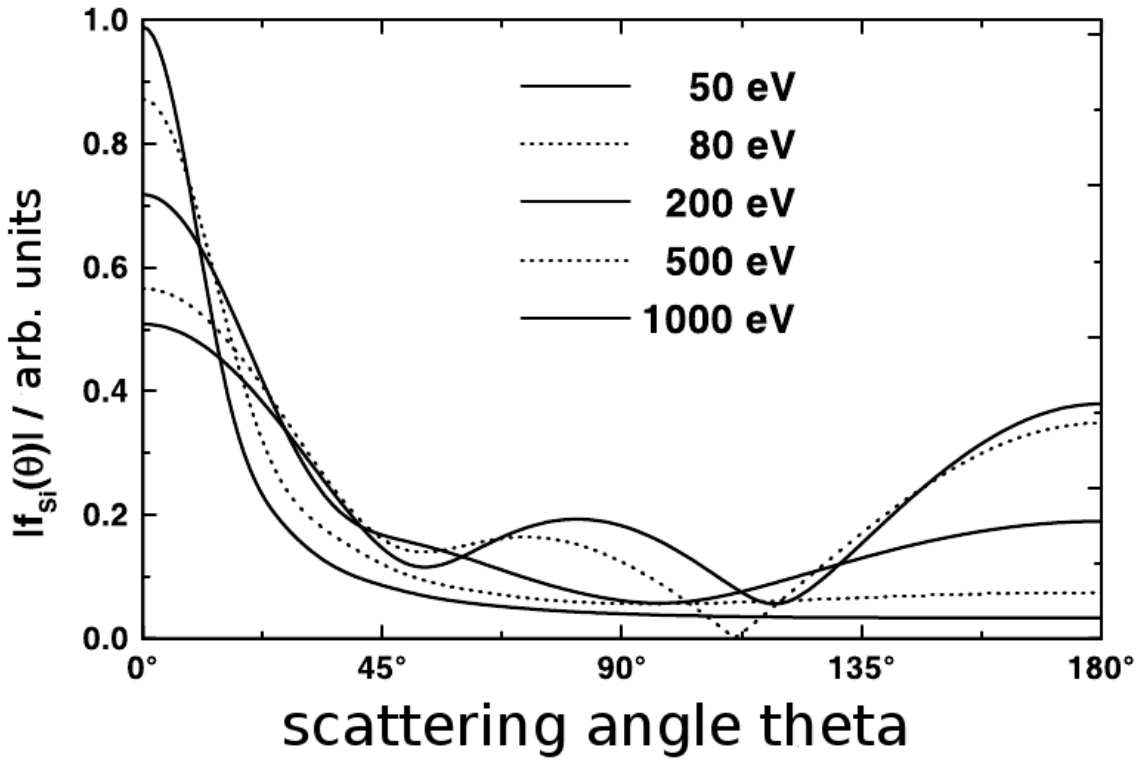

Figure 2.9: Si-scattering amplitude dependent on scattering angle and kinetic energy of the photoelectrons. The amplitude was calculated with a program by Salvat and Mayol [25]

factor on kinetic energy. At high kinetic energies, scattering is mainly observed along the emitter-scatter-axis. Scattering along this axis is called forward scattering. At lower kinetic energies the scattering is observed to be more isotropic. Fig. 2.9 shows the complex atomic scattering factor of silicon for different energies.

2.3.1 XPD Measurement and Data Treatment

A measurement of the resulting intensity variation described in section 2.3 over the hemisphere over the sample is called a diffraction pattern. In principle, the hemisphere over the sample can be scanned in two ways. Either the detector can be moved with respect to the sample, or the sample can be rotated with the detector in a fixed position. In this work the second solution is chosen. A schematic of this procedure is shown in Fig. 2.10. To cover the whole hemisphere, XPS spectra are typically recorded in 2° steps for the polar and azimuth angle. This leads to $\sim$ 8000 XPS spectra for one diffraction pattern.

For this amount of data, an adequate illustration is needed. Therefore, a so called anisotropy-function is defined:

$$\chi(\Theta, \Phi) = \frac{I(\Theta, \Phi) - I_0(\Theta)}{I_0(\Theta)} \tag{2.14}$$

In this formula $\chi(\theta, \phi)$, $I(\theta, \Phi)$, and $I_0(\Theta)$ denote the anisotropy-function, the intensity of each XPS spectra, and the mean intensity per polar angle, respectively.

Additionally, a maximum anisotropy is defined as follows:

$$\chi_{max} = \chi_{max}(\Theta, \phi) - \chi_{min}(\Theta, \phi) \tag{2.15}$$

In a linear grey scale model the lightest point is referred to $\chi_{max}(\Theta, \phi)$ and the darkest point is referred to as $\chi_{min}(\Theta, \phi)$. As shown in Fig. 2.10(b), the anisotropy function delivers one value for each position of the hemisphere. Each of these points is the result of a XPS spectrum as shown in Fig. 2.10(c) and explained above. Due to presentation considerations the hemisphere is normally projected into the 2d-plane, as shown in Fig. 2.10(d). All XPD results shown in this work are presented as a 2d-projection and are referred to as diffraction pattern.

There are two ways to draw conclusions regarding the atomic structure from the diffraction patterns. On one hand, a Fourier-transformation into real space can be performed to directly obtain information from the diffraction patterns. On the other hand, simulation calculations with varying structures can be performed until the resulting pattern matches the measured data. For the first method, the phase of the electrons is needed, but the phase cannot be measured within the normal photoelectron diffraction. Therefore, this method is not possible in this work. For the second method, a simulation tool and a standard to compare the experimental and simulated data is needed. The simulation program used in this work is called MSPHD and is discussed in section 3.1. The standard to compare the experimental and simulated data is the reliability-factor(R-factor):

$$R = \sum_i \frac{(\chi_{th} - \chi_{exp})^2}{\chi_{th}^2 + \chi_{exp}^2} \tag{2.16}$$

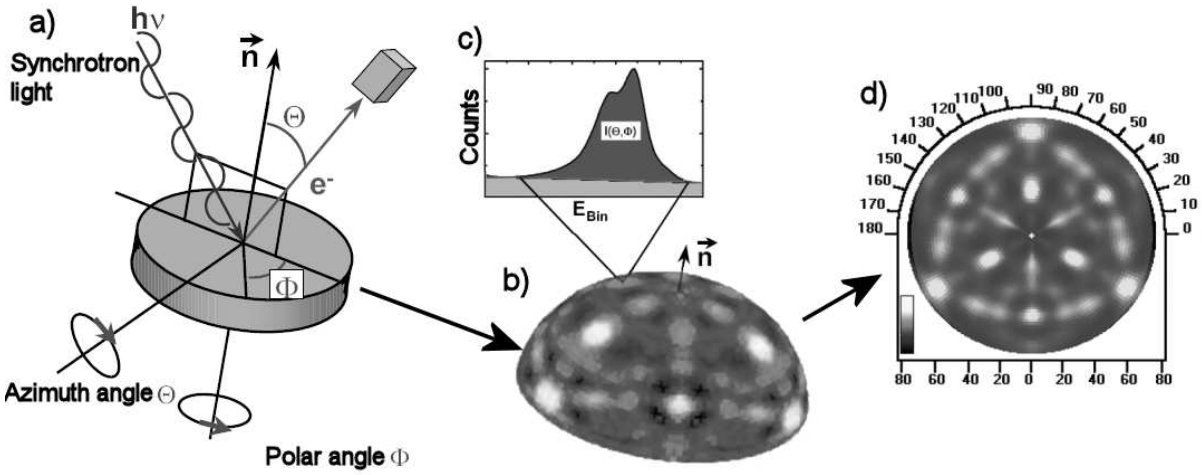

Figure 2.10: Schematic of an XPD experiment(a), plot of the anisotropy function in the hemisphere(b), XPS spectra associated with one point of the hemisphere(c), and projection of the anisotropy function into the plane(d)

Due to the definition of the R-factor, it will be 0 when the experimental pattern and the simulated pattern are exactly even. An R-factor of 1 means that the patterns have nothing in common and an R-factor of 2 means the patterns are anticorrelated. Therefore, the goal in an R-factor-analysis is to bring the R-factor as close to 0 as possible. Different methods to reduce the R-factor and enhance the structure models are discussed in section 3.2.

3 Theory of Simulation Calculations and Algorithms

As explained in section 2.3, the phase information of the electronic wave function is lost during the experimental measurements. Therefore, it is impossible to determine the atomic structure by turning the recorded diffraction pattern back to real space with a Fourier-Transformation. Due to this, it is necessary to select out the atomic structure from different atomic model clusters. The simulated diffraction pattern of these model clusters is then compared to the experimental data. In this work, the simulation calculations were performed with the program MSPHD (full Multiple Scattering code for low energy PHotoelectron Diffraction) [9]

3.1 Simulating Patterns with MSPHD

The MSPHD software is specially designed for the simulation of low energy diffraction patterns. Energy ranges up to ∼2000 eV are possible, but the program is optimized for the energy range between 30 and 200 eV. In the MSPHD package the photoionization cross section is calculated in the following way:

$$\frac{d\sigma}{d\hat{k}} = const(k,\omega) \sum_{m_0} | \sum_{j} \sum_{LL'} M_L^{L_0} \tau_{LL'}^{oj} i^{l'} Y_{L'}(\hat{k}) e^{i\vec{k}\cdot\vec{R_{jo}}} \tag{3.1}$$

This equation describes the creation of a scattering wave field in three steps:

First, the origin of the field is set by an emitting atom with the index o. From this position, a spherical electron wave is emitted. The array element of the electric dipole operator $M_L^{L_0}$ transforms an atomically bonded electron with the energy state L_0 into a

free electron with the energy state L. For this transformation, the array element depends on the polarization of the incoming light. The state L is a 2-tuple of the quantum number, which is linked to the orbital angular momentum l and the magnetic quantum number m.

In the next step, the diffraction effects are calculated. This is represented in equation 3.1 by array element $\tau_{LL'}^{oj}$ of the diffraction path operator. $\tau_{LL'}^{oj}$ describes the amplitude of the scattered spherical wave $i^{l'}Y_{L'}$, which is emitted at the scatterer atom j. The atom j in this description denotes the last scatterer atom in the possible multi-scattering process before the electronic wave propagates into the vacuum level. In the calculation of τ, all previously performed scattering processes are considered. Each of the considered scatterer atoms, including the last scatterer j, are arranged within a sphere around the emitting atom. The radius of the sphere is defined in the code of the program prior to the simulation. This array element of the diffraction path operator is defined as follows:

$$\tau_{LL'}^{oj} = [(T^{-1} + G)^{-1}]_{LL'}^{oj} \tag{3.2}$$

This operator solves the problem of multiple scattering in any order. For the calculation of the diffraction path operator, the potential of the structure is approximated as a Muffin-Tin-Potential. Within the cutoff radius of each atom, the Muffin-Tin-Potential is described by the Hedin-Lundqvist-Potential. The operator G in equation 3.2 describes the propagation of the electron wave function within the constant part of the potential. In this part of the potential, the wave function between the atoms i and j can be described as:

$$G_{LL'}^{ij} = 4\pi \sum_{L''} i^{l+l''-l'} C_{LL'}^{L''} [-ih_{ll'}^{+}(kR_{ij})] Y_{L''}(\hat{R}_{ij}) \tag{3.3}$$

with R_{ij} as the vector between both atoms, $C_{LL'}^{L''}$ as the Gaunt-coefficients, and h as the Hankel-spherical wave. The diffraction effects within the potential is considered by the matrix T:

$$T_{LL'}^{ij} = e^{\delta_l^i} sin(\delta_l^i) \tag{3.4}$$

with δ_l^i as the complex phase shift of the electron wave function. In the constant part of the Muffin-Tin-Potential, the phase shift between the atoms i and j is calculated analytically. In the Hedin-Lundqvist-Potential, the phase shift is approximated numerically. The damping of the electron wave function inside the bulk is directly considered because of the complex form of the potential. Therefore the operator T includes all the scattering effects discussed in section 2.3. Finally equation 3.4 is convolved with a plain wave function. This plane waves describes the propagation of an electron through the vacuum. The propagation vector k of this planar wave is toward the detector.

After this, the overall scattering wave field is obtained from the superposition of all possible scattered wave functions in the local environment of the emitting atom. The factor $const(k, \omega)$ in equation 3.1 is dependent on the wave vector k and the frequency of the incoming light ω. These two parameters are provided to the program before the start of the simulation, because they are well known from the experimental data. The emitting orbital is provided to the program as well and the kinetic energy of the emitted electrons is inserted. From this information the program can easily calculate the energy of the incoming light. These latter two parameters are kept constant through the simulations and the experimental measurement and therefore the factor $const(k, \omega)$ is only stretching or compressing the simulated data relative to the measured data. This needs to be considered in the R-factor analysis (cf. Eq. 2.16) by normalizing both data sets.

In the MSPHD program the different steps described above are done in the following manner:

- Calculation of the Muffin-Tin-Potential
- Creation of symmetric base functions for the electron wave function of the final state
- Calculation of the complex phase shift, dipole array elements and inversion of the matrix in equation 3.2
- Calculation of the diffraction pattern using equation 3.1

This kind of simulation takes between 20 minutes and 2 hours with a standard 2.6 GHz-processor with 2 GB of memory. Most of the calculation time is needed to invert the matrix from equation 3.2. This time depends on the chosen radius around the emitting atom and on the orbital angular momentum of the final state for the electron wave function. Depending on the number of atoms chosen as emitters for the diffraction pattern, the required time must be multiplied by the number of emitters.

3.2 R-factor Minimization by Genetic Algorithms

Simulation times can increase drastically depending on the number of parameters that need to be varied in a model cluster to solve the real structure corresponding to the experimental data. As one simulation can take up to two hours, a Grid-Scan of the parameter space cannot be performed, because this would take an unrealistic amount of time. Also, a gradient-algorithm-method is not useful in this case because in a multi-dimensional parameter space, it would be necessary to calculate a lot of supporting points for the algorithm. This would drastically increase the time needed for all calculations. Additionally, gradient-algorithm-methods tend to trap themselves in local minima, instead of converting to the global minimum. Due to this fact genetic algorithms have been approved in the structure determination. Generally, a genetic algorithm creates random parameter sets as solution proposals for the problem at the beginning. Then, this algorithm tries to improve these parameter sets by combination and selection. Within the analysis of diffraction patterns a special genetic algorithm was designed to optimize the model clusters relative to the experimental data. The general functionality of this algorithm will be discussed below.

Fig. 3.1 shows a schematic view of the functionality of the genetic algorithm used:

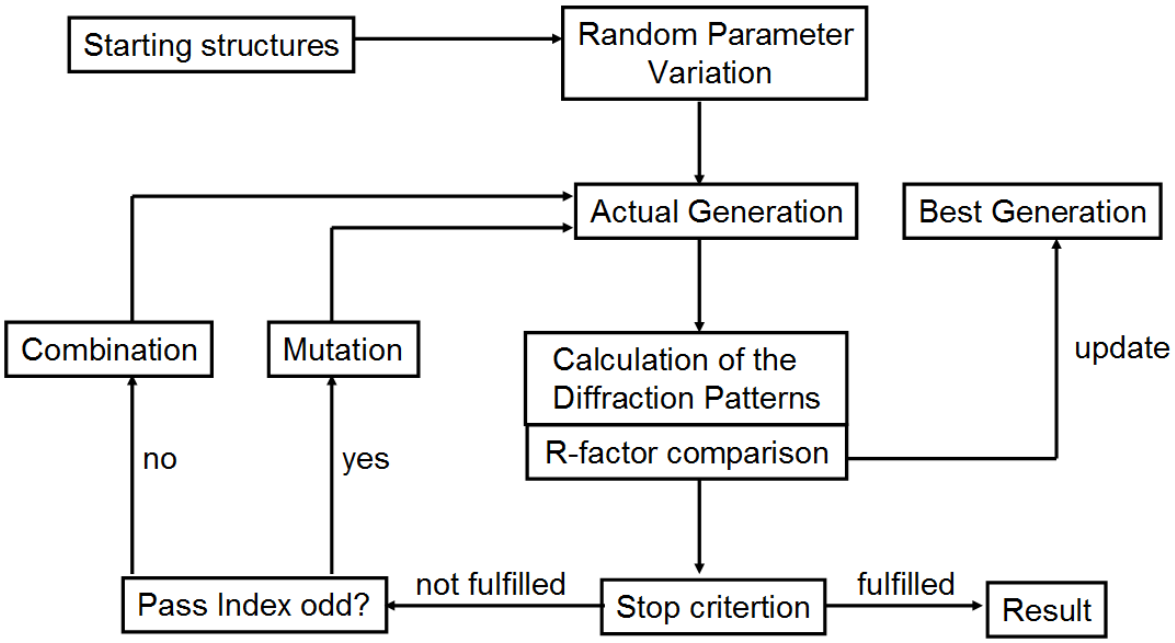

Figure 3.1: Operating mode of the genetic algorithm for structure determinations

At the beginning of the procedure, a starting structure is defined. This starting structure includes the composition of the unit cell. Additionally the static attributes assigned to each structure object are defined. In the next step, a predefined number of structure objects are created from this information. For these structure objects, completely random parameters within the boundaries of the deformation-functions are generated. This assembly of structure objects is defined as the actual generation. In our work group a computer cluster with 28 CPUs is available for simulations and therefore normally one generation consists of 28 structure objects. For the simulation calculations of the diffraction pattern, the program makes an input file for the MSPHD for each structure object. The input file contains all necessary information for a simulation, including the various positions of the atoms. Following all the simulations, all calculated patterns are compared to the experimental data. The structure objects containing the best R-factor up to that point are saved in a separate array. In this array, the same number of structure objects is stored as in a normal generation. The implementation of this best generation of structure objects should avoid the complete loss of a very promising structure object due to very unfavorable parameter variation. In this special array, all structure objects are kept until one or more better R-factors are obtained in the actual generation. In this case, the worst R-factors in the best generation are replaced by the new ones. Next, the stop criterion for the algorithm is checked. The program will stop the genetic algorithm if the R-factors fall below a pre-defined value or if the maximum number of predefined passes is reached. If the stop criterion is not fulfilled, a new set of structures is generated. The program chooses the kind of variation depending on the pass index. In the case of an even pass index, the the combination routine is chosen and for an odd pass index, the mutation routine is chosen. These two routines will be described below.

Fig. 3.2 shows a schematic view of the combination routine. In the combination routine the program randomly chooses three structure objects from either the actual generation or the best generation. The object with the best R-factor is chosen as the mother object for the combination. Both remaining structure objects are returned to the pool of possible candidates. After this the procedure is repeated and the best of the three structure objects is chosen as the father object for the combination. From a combination of the genes of the mother and father objects a new structure object is generated. For each gene (parameter) its origin from either the mother or the father object is randomly chosen. The whole process is repeated until a complete new generation of structure objects is available for simulation calculations in the MSPHD.

The mutation routine is included in the genetic algorithm to bring in new parameter

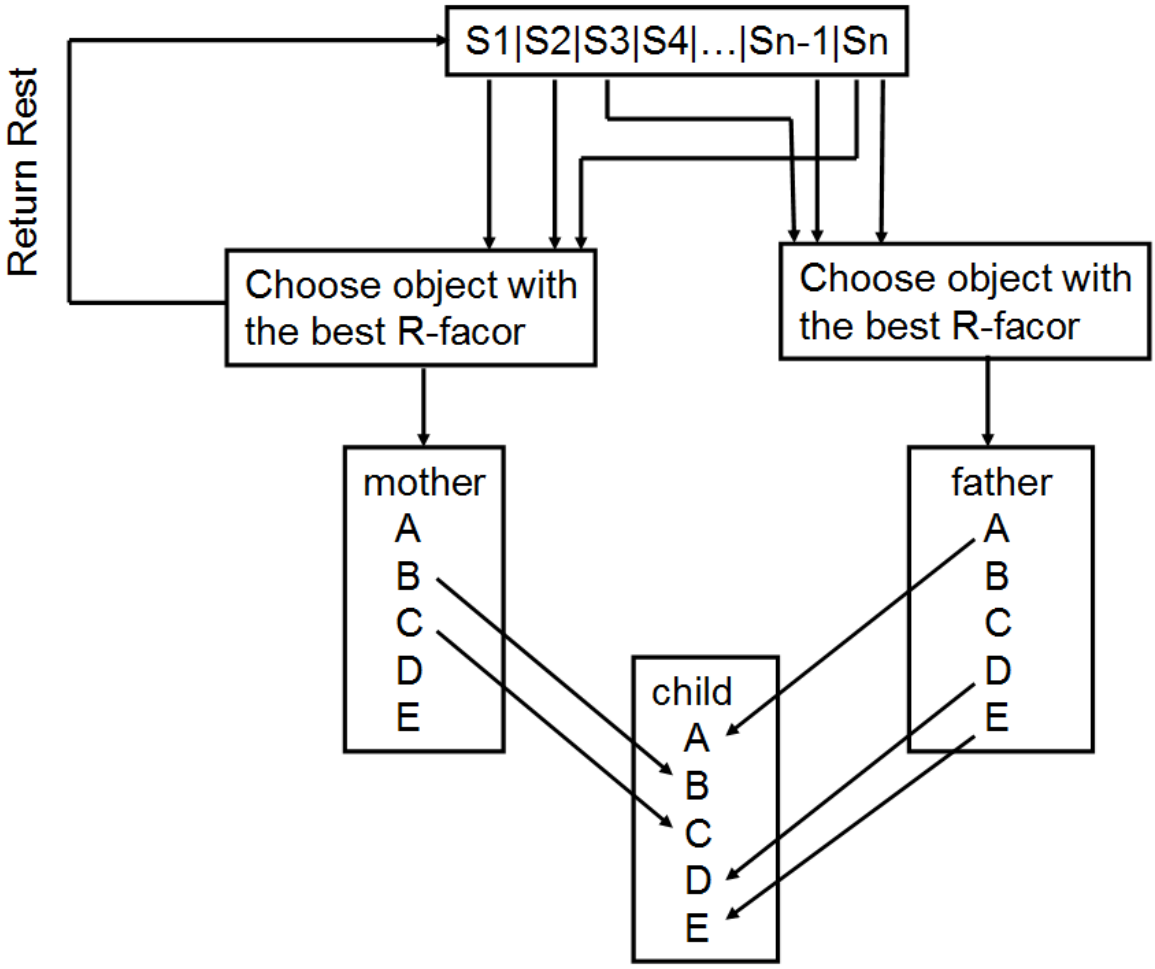

Figure 3.2: Schematic view of the combination routine

values to the optimization routine. For the mutation routine, all structure objects from the best generation are chosen. Within the routine, all genes from each structure object are varied randomly. The probability P for a variation of each gene from a value A0 to a value A1 is given by a Gaussian function:

$$P(A_1) = \begin{cases} 0, & \text{if } A_1 \notin [A_{min}, A_{max}] \\ \frac{1}{c} \exp\left(\frac{1}{2}\left(\frac{A_1 - A_0}{\sigma}\right)^2\right), & \text{if } A_1 \in [A_{min}, A_{max}] \end{cases} \tag{3.5}$$

$$c = \int_{A_{min}}^{A_{max}} \exp\left(\frac{1}{2}\left(\frac{A - A_0}{\sigma}\right)^2\right) dA \tag{3.6}$$

A normalization c is necessary to set the probability to find a new parameter in the interval [A_{min} , A_{max}] to 1. A_{min} and A_{max}, in this case, belong to the limits of the variation interval for each parameter. The variance σ of the Gaussian-function is directly linked to the R-factor of the structure object before the mutation:

$$\sigma = b \cdot R \tag{3.7}$$

Following this formula, structure objects with a low R-factor are only varied by a small amount, whereas objects with high R-factors are strongly varied. In the case of a small variation, the mutated structure object is close to the old structure object in the parameter space. This leads to an accumulation of structure objects around the minimum of the R-factor.

In general, these two processes define the whole algorithm. However, it is necessary to integrate some restrictions to avoid cloning within the algorithm. In the combination routine the parameters are only copied from different structure objects, but no variation takes place. Therefore there is a small chance that two or more structure objects with the same genes might be produced. If these clones are not filtered out, the chance for more clones increases drastically, because a combination of two clones produces another one. The probability increases even more if the clones are linked to very good R-factors and are therefore preferred in the combination process. As the structure objects with the best R-factors are kept for the following variation procedure this leads to new clones in each pass. At some point, this would mean a disruption of the algorithm because no new structure objects would be generated anymore.

Due to this, some restrictions were placed on the genetic algorithm to avoid cloning:

- In the combination process at least one gene must originate from the mother and one gene must originate from the father
- Structure objects with an identical R-factor are not allowed in a combination
- All structure objects in the best generation must hold different R-factors

These restrictions completely disable the cloning expansion. The first two restrictions lower the possibility for cloning. With these two restrictions, only one possibility is left for producing a clone. If, in two combination process the same mother and the same father are chosen and the gene sequence is transferred in the same way, two identical structure

objects can be produced. The probability for the same gene sequence is $\frac{1}{2^n}$ with n as the number of genes in each structure object. As there are typically 56 structure objects in each combination routine and more than 10 genes within each structure object, the probability for cloning is very low. If one of these cases occurs, the last restriction makes sure that only one of the identical objects remains in the procedure.

4 Experimental Setup

4.1 UHV Chamber

Very clean surfaces are required to the study of surfaces and interfaces in the soft x-ray regime. As explained in section 2.3, the mean free path of the electrons do not exceed some monolayer in the kinetic energy range around 50 eV. Therefore, even thin films of "dirt" on the sample would completely ruin the desired measurement. The unwanted contamination would reduce the total count rate in the determined XPS lines and produce chemical shifts inside the signals. Therefore, an ultra-high-vacuum (UHV) is required for these measurements.

Fig. 4.1 shows a schematic view of the UHV chamber used in this work. The UHV chamber consists of two separate chambers, which can be evacuated and vented separately. The small pre-chamber allows new samples to be brought into the main chamber without venting it each time. A transport from the pre-chamber to the main chamber is possible under vaccum conditions using a manipulator device. In principle, this devices is a two meter stick, which can be moved from the pre-chamber to the main chamber by a magnetic feed through. The sample holder (cf. 4.1.1) can be attached to the front of the stick.

The vacuum in the pre-chamber is created by a membrane pump and a turbomolecular pump. The membrane pump can reach vaccum levels of about 1 mbar within several minutes. After this, the turbomolecular pump can reach a base pressure of about $5 \cdot 10^{-9}$ mbar within two hours.

Inside the main chamber, a vaccum is achieved via a membrane pump, turbomolecular pump and a titan sublimation pump. The pressure inside the main chamber is measured independently by a hot cathode and a cold cathode ion gauge. According to the approximation of Langmuir [26], an adsorbate layer forms within one second, if the pressure is in the order of $1 \cdot 10^{-6}$ mbar. Using a residual gas analyzer (RGA), it was possible to determine the partial pressures of the residual gas species. It was found that at least

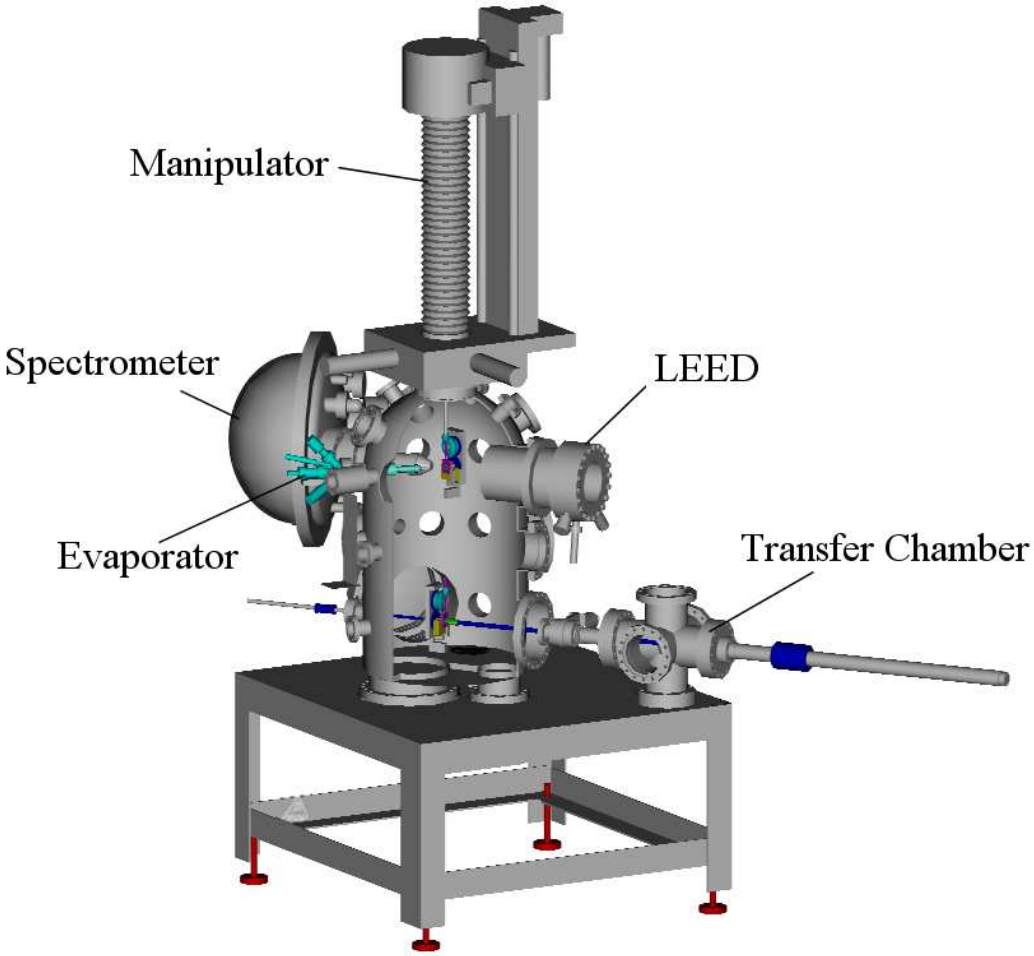

Figure 4.1: Schematic view of the UHV chamber

90% of residual gases consist of hydrogen. The partial oxygen pressure that was the major concern in the experiments was determined to be around $1 \cdot 10^{-11}$ mbar or lower. Achieving this kind of vacuum level takes about two days including a backout procedure in order to remove thin water films from the inner walls of the chamber. More precise details regarding vacuum technology and pumping systems can be found in the literature by Wutz et al. [27].

To conduct in-situ sample movements, a manipulator is built into the chamber that allows movements along all three spatial directions, as well as rotations around two main axes of the sample. Stepping motors are used to steer the movement along the z-axis, as indicated in Fig. 5.1, and along both angular directions that will be referred to as Φ and Θ, comparable to spherical coordinates. The resolution of the motorized movements is $\Delta z = 1\ \mu m$, $\Delta\Phi = 0.12°$, and $\Delta\Theta = 0.05°$.

4.1.1 Sample Holder

Fig. 4.2 shows a picture of the sample holder used in this work. This sample holder is designed specifically for XPS measurements. The base part of the sample holder is made of molybdenum, whereas the electrical contacts are made of copper. The three electrical sliding contacts allow grounding of the sample during the whole rotation process of an XPD measurement. The insulation between them is by saphire rings and balls. The complete sample holder consists of approximately 30 pieces and has a height of about 25 mm. With this height, the sample is exactly in the center of the Θ axis, which is very important for the measurements.

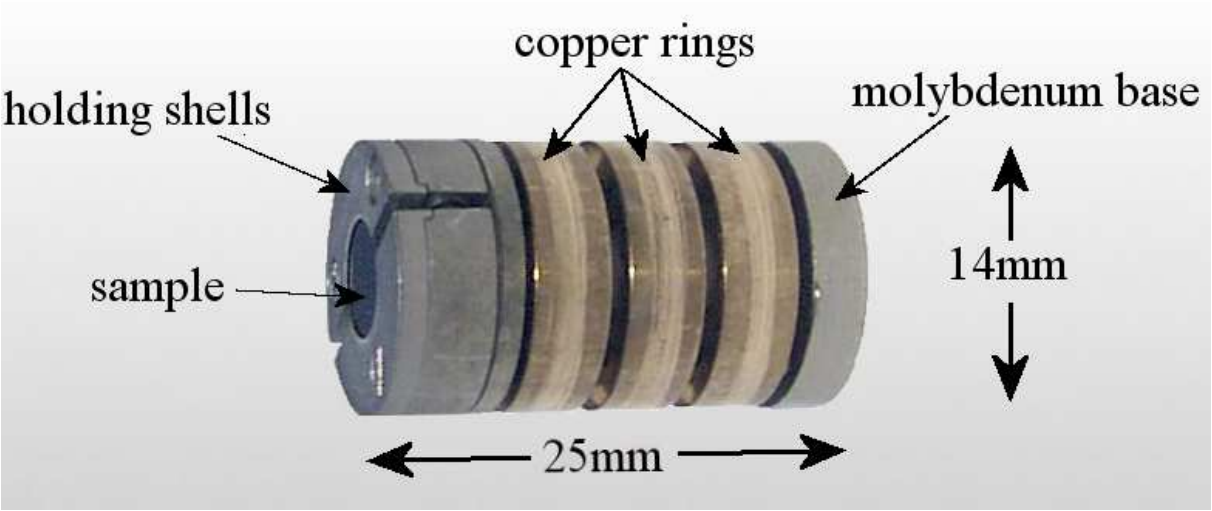

Figure 4.2: Sample holder for semiconductor samples. The sample is mounted at the front end of the holder by molybdenum clamps.

Thanks to the copper contacts semiconductor samples can be annealed by direct heating. Currents up to seven amperes can pass through the holder inside the vaccum chamber. Due to the cylindrical shape of the sliding contacts, the sample holder can be rotated around its main axis without interrupting the contact to earth.

4.1.2 Spectrometer and Detector

The UHV chamber is equipped with an energy dispersive hemisphere analyzer of the type CLAM 4 [28] to measure the kinetic energy of the electrons. An aperture at the entrance of the spectrometer determines the acceptance angle of the analyzer. The radius of the aperture defines the angular acceptance of the experiment. Fig. 4.3 shows a schematic

view of the inner part of the hemisphere analyzer. The electrons that pass through the aperture are projected onto the entrance slit of the spectrometer. In this procedure, before entering the analyzer by passing through the entrance slit, the electrons travel through a lens system and a retarding field that is used to enhance the energy resolution $\frac{\Delta E}{E}$ of the analyzer [15]. This is possible because the retarding field changes the absolute energy E of the electrons, while leaving the energy distribution ΔE untouched.

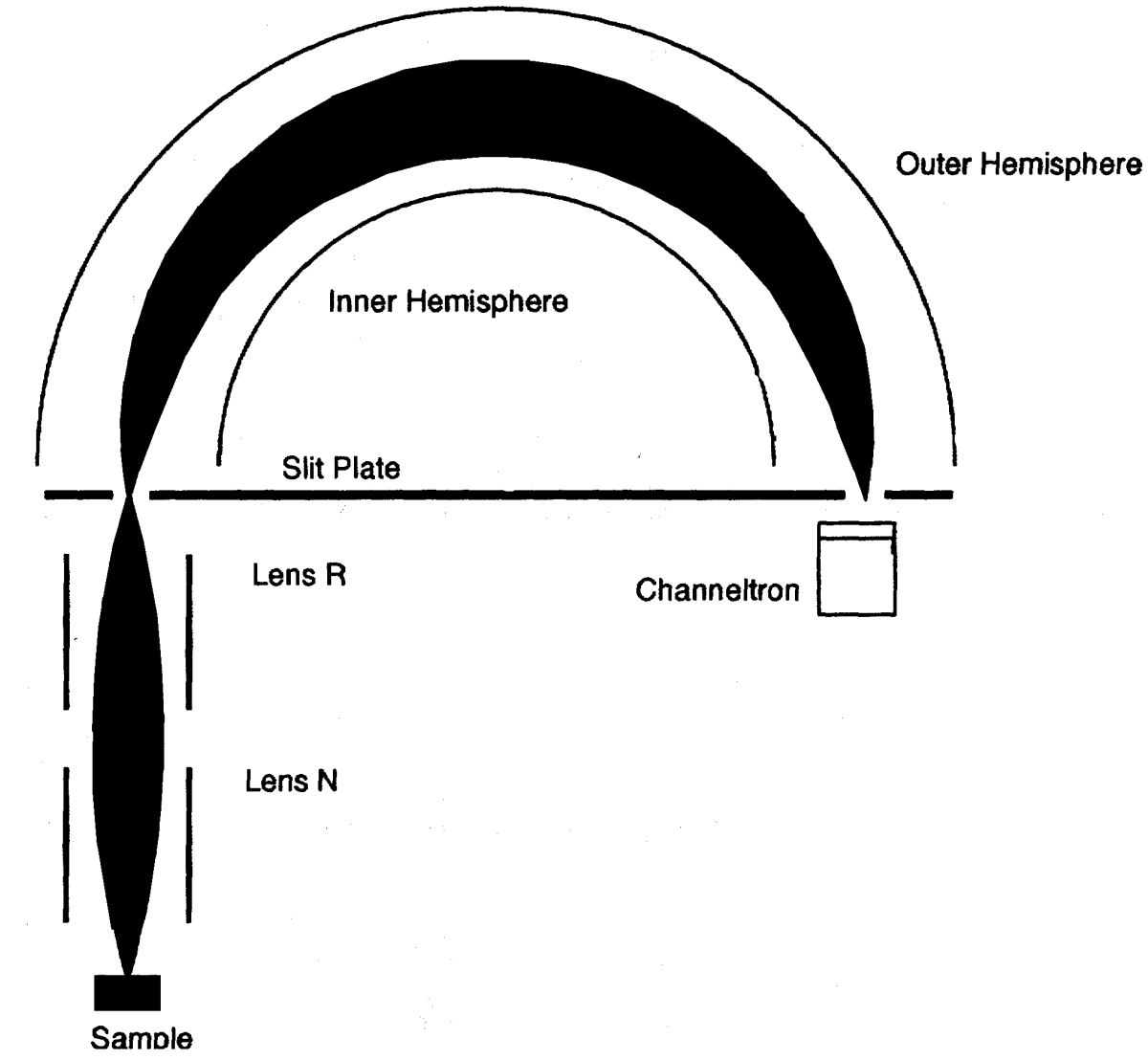

Figure 4.3: Schematic view of the inner part of the hemisphere analyzer [28]

Behind the entrance slit only electrons with a kinetic energy equal to the so called pass energy can travel through to the exit slit. The pass energy is achieved by an electrical field between the inner and outer hemispheres. Electrons without the right pass energy are adsorbed on one of the hemispheres. To vary the kinetic energy within an XPS

measurement (cf. section 2.2), the lens system outside the entrance slit exactly slows only the desired electrons to the pass energy. Behind the exit slit, the electrons are detected by a channel electron multiplier (CEM) detector unit. Analogous to a secondary electron multiplier (SEM), the impinging high-energy particles, in this case electrons, create a significant number of secondary electrons out of a low work function material. However, in contrast to an SEM, the CEM uses a continuous funnel-shaped dynode. High voltage is applied between the entrance and the end of the funnel for a further acceleration of secondary electrons towards its inner walls. Thus, a single electron can produce an avalanche of 10^8 electrons that can be detected as an electrical pulse at the rear end of the CEM. The pulses typically have an amplitude of 5-20 meV and a width of a few nano-seconds. After further amplification, the pulses are counted by a computer program. Using this setup, up to one million single electron events per second can be recorded.

4.1.3 LEED and Pyrometer

There are two analytical tools attached to the chamber that are mainly used in the preparation process: the LEED-System(Low Energy Electron Diffraction) and a pyrometer. A LEED system uses the diffraction of low-energy electrons to detect long range order at the surface. A detailed description of the theory of LEED can be found in a book by J.B. Pendry [29]. In our work, the LEED system was only used to control the periodicity of the silicon substrate material (cf. section 5.2).

The pyrometer is attached to the chamber outside the vacuum and allows the samples temperature to be determined. A pyrometer measures the wavelength of the emitted light by the sample and uses this information to determine the temperature. The wave length of the emitted light and temperature are linked by the Stefan-Boltzmann-Law. The pyrometer, unlike other methods of measuring temperature, does not require contact to the sample to conduct measurements. This is essential for XPD measurements where a fixed connection to the sample would constrict the rotation (Φ-axis) of the sample. Additionally, a wide temperature range is covered (400 K to 2300 K).

4.2 Undulator Beamline 11 at DELTA

The experiments in the soft x-ray regime took place at beamline 11 in the synchrotron DELTA (Dortmunder Elektronen Speicherring Anlage) of the Technical University Dort-

mund. This beamline is coupled to undulator 55 inside the synchrotron. Undulator beamlines deliver very high flux with very good energy resolution simultaneously. Inside the beamline, several parameters can be varied to find the best composition of flux and energy resolution. The best composition strongly depends on the experiment and must be determined specially for each experiment. Fig. 4.4 shows the schematic view of beamline 11.

For the working principles of beamlines for soft X-ray light, a more detailed description of beamline 11 at DELTA is given below. A beamline consists of several mirrors to focus the photon beam and pass it from the undulator to the experiment. However, the most important part of a beamline is the monochromator. Inside the monochromator of beamline 11, a plane grating and a plane mirror are mounted. This kind of monochromator is called PGM (Plane Grating Monochromator). The monochromator allows one special wave length to be chosen from the wavelength spectrum delivered by the undulator. Only the chosen wavelength is projected onto the exit slit of the beamline so that it reaches the experiment. As the light reaches the grating, many diffraction orders of the light appear simultaneously. Generally, the monochromator is aligned with the maximum of the first order to be projected onto the exit slit. At beamline 11, the grating inside the monochromator is blazed. This means that the slope of the grating line is aligned in a chosen direction. This results in amplification of the photon flux along the blaze direction. Experimentally, this means a high photon flux at the sample along with a very small focus of the beam. The focus size at beamline 11 is about 70μm x 30μm. For some measurements, it is advantageous to increase this diameter. An example will be given in section 5.1.

The undulator 55 delivering the photons to the beamline is equipped with permanent magnets that are set at a distance of 27.5 mm. Within an undulator, the magnetic arrangement varies between the north and south pole. Therefore, a full period between two equal magnetic states is 55 mm, which gives the undulator its name. The changing of the magnetic field results in an oscillation of the electrons inside the undulator. Due to this movement, the electrons show the characteristics of a relativistic electric dipole. As with every relativistic electric dipole, the electrons emit radiation in their propagation direction. The universal rule for the relation between the magnetic field strength and the emitted wave length inside the undulator is given as:

$$\lambda_{1.Harmonic} = \frac{\lambda_0}{2\gamma^2} \cdot (1 + \frac{K^2}{2}) \tag{4.1}$$

with

$$K = \frac{eB_z\lambda_0}{2\pi mc} = 93.4 \cdot B_z[T]\lambda_0[m] \tag{4.2}$$

and

$$\gamma = \frac{1}{\sqrt{1 - \frac{v^2}{c^2}}} \tag{4.3}$$

In this formula, B_z denotes the magnetic field strength perpendicular to the propagation direction of the electrons, λ_0 the length of one undulator period , and $\lambda_{1.Harmonic}$ the wave length of the emitted light.

As is visible in Eq. 4.1 the wavelength of the emitted light is correlated with the factor K. This factor is proportional to the magnetic field strength in the z-direction. Therefore, a variation of the magnetic field strength in z-direction will result in a change of the emitted wavelength. This variation can be achieved by changing of the distance between the undulator magnets in the z-direction. A different gap, along with higher harmonics, allows a wide energy range to be covered. At beamline 11 the gap can be varied from about 20 mm up to 300 mm, and the harmonics 1st-5th are typically used. With these variations and additional variations inside the beamline itself an energy range of 55 eV to 2000 eV can be reached.

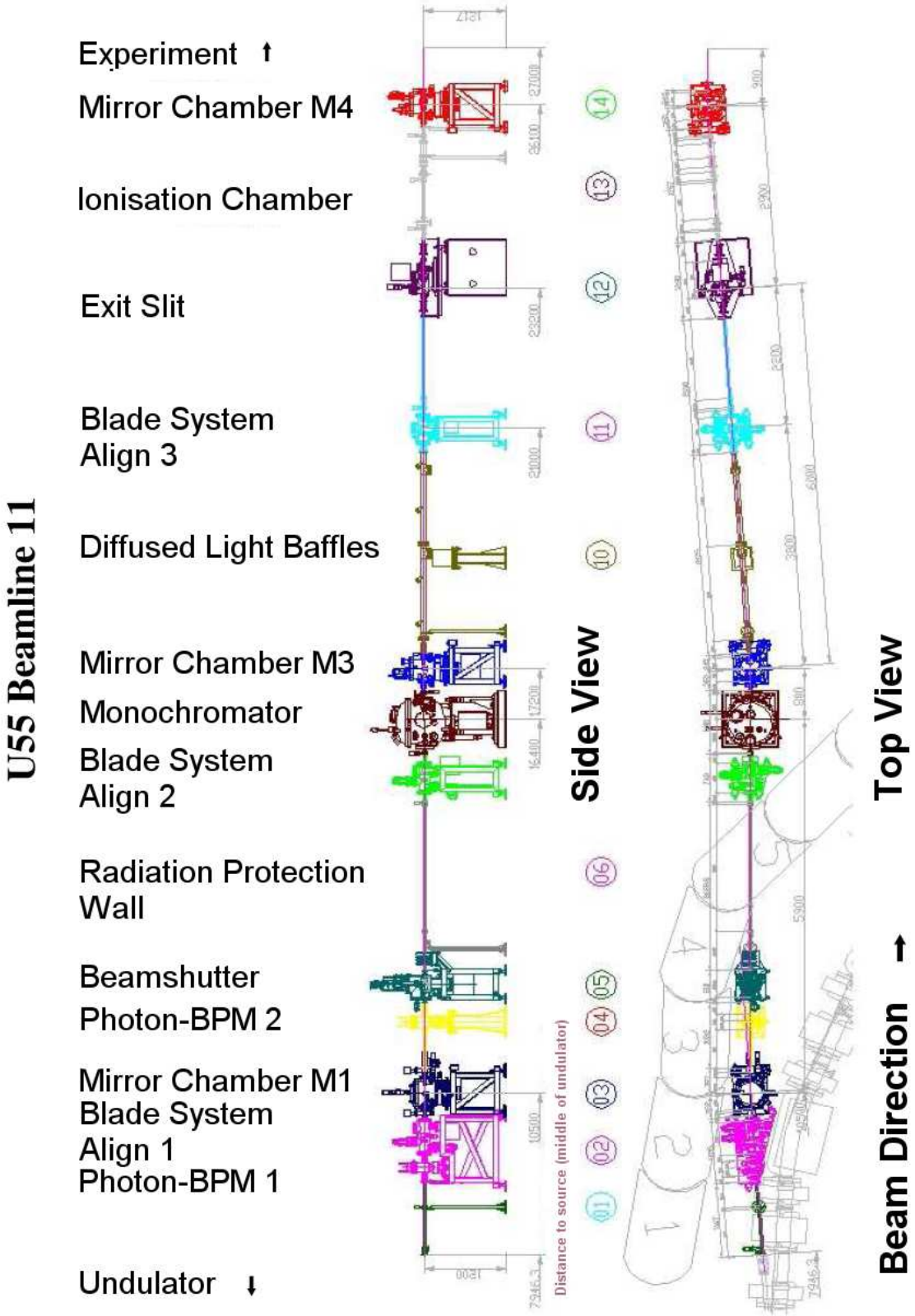

Figure 4.4: Schematic of the plane grating monochromator beamline 11 at DELTA [30].

5 Results and Discussion

5.1 Radiation Damage to Molecules in Synchrotron Light

In the context of studies on soft matter at surfaces with photons, it is always necessary to consider radiation damage. In the case of conventional X-ray tubes, the amount of incoming photons and emitted electrons per unit area is very limited and therefore radiation damage is not a big problem. However, with synchrotron radiation the amount of incoming photons per unit area is much higher. Therefore, many investigations regarding the radiation damage to molecules on various substrates have been performed [31, 32]. In the context of this investigation, it was found that many different effects are involved in the existence and the amount of radiation damage. One of the most important factors, however, is the amount of incoming photons in a defined sample area in a time window. The overall amount of incoming photons during the whole experiment seems to play a much smaller role in radiation damage [31, 32].

To take this factor into account, preliminary investigations regarding the radiation damage at beamline 11 at DELTA have been performed in order to minimize the radiation damage to the sample for the following studies. From literature, it was known that in particular alkanethiols on gold surfaces feature a high susceptibility to radiation damage in synchrotron light [31, 32]. Due to this fact, one of these systems was chosen in order to minimize the radiation damage. The possibility of reducing the radiation damage at this very sensitive system should also provide excellent improvement to the stability of the molecules studied in this work, especially because the molecules studied in section 5.4 and 5.5 are known to be much more stable in synchrotron light than the alkanethiols.

For the preparation of the system, a Au(111) sample was cleaned and annealed in multiple sputter and annealing cycles. The parameter for these sputter-annealing-cycles are well known and were taken from literature to achieve a surface quality comparable to previous experiments [33]. The quality of the surface was checked by LEED, XPS and

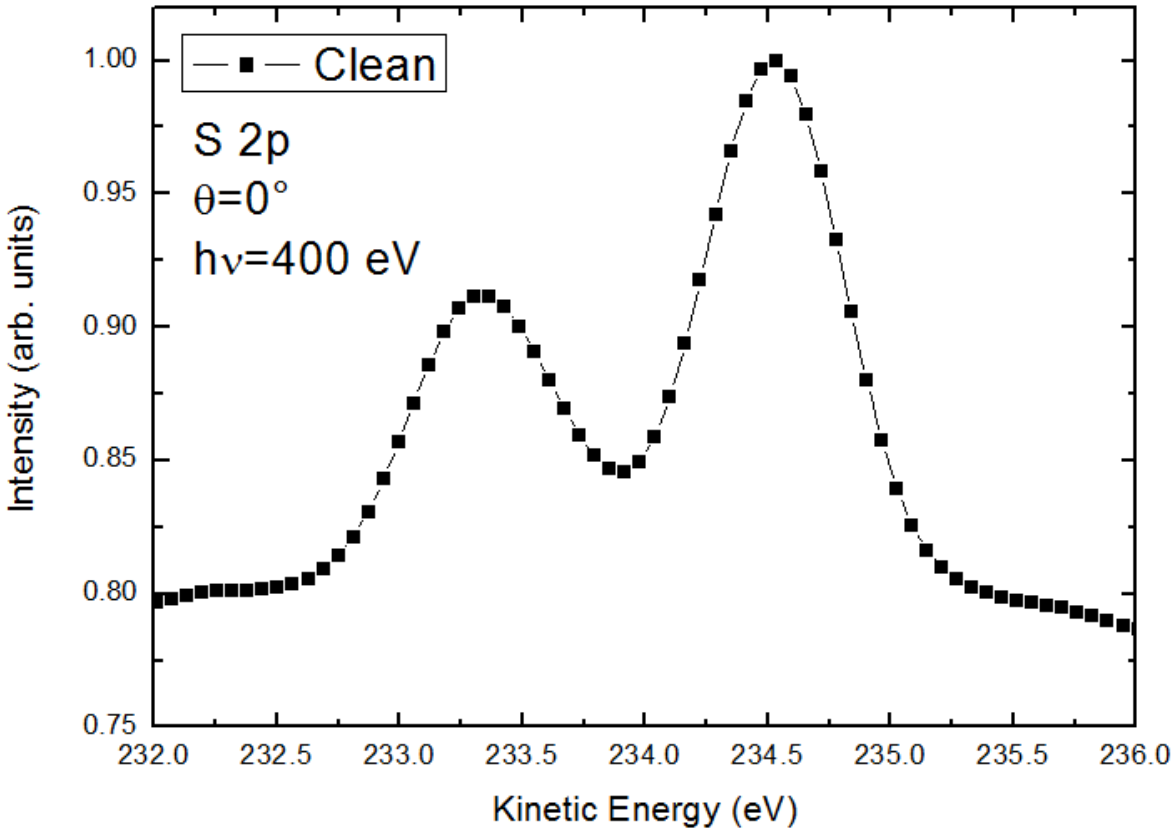

Figure 5.1: XPS spectra recorded from the S 2p signal for the unradiated surface of ethanthiol/Au(111).

STM (Scanning Tunneling Microscopy), respectively. In the next step, ethanthiol was applied to the surface. This molecule is known to form self-assembled-monolayers(SAMs) when applied to a gold surface.

A typical XPS spectrum of the Sulfur 2p signal is shown in Fig. 5.1. This spectrum was recorded immediately after the preparation procedure and therefore no radiation damage is expected. The typical spin-orbit splitting of a 2p level is intact, including the intensity ratio and the energetic difference between the $S_{1/2}$ and the $S_{3/2}$ peak. Based on observations in previous studies, a strong change in this signal is expected if radiation damage occurs. Radiation-induced damage in this system changes the bonding configuration of the sulfur and therefore the line shape of the signal.

Our first measurements were conducted at the focus position of the beamline. At this position, the size of the photon beam is 70 x 30 μm^2 (FWHM) and all photons are "packed" in this area. The results of these measurements showed strong radiation damage occurring at the molecule-substrate interface due to the high photon flux per area. This

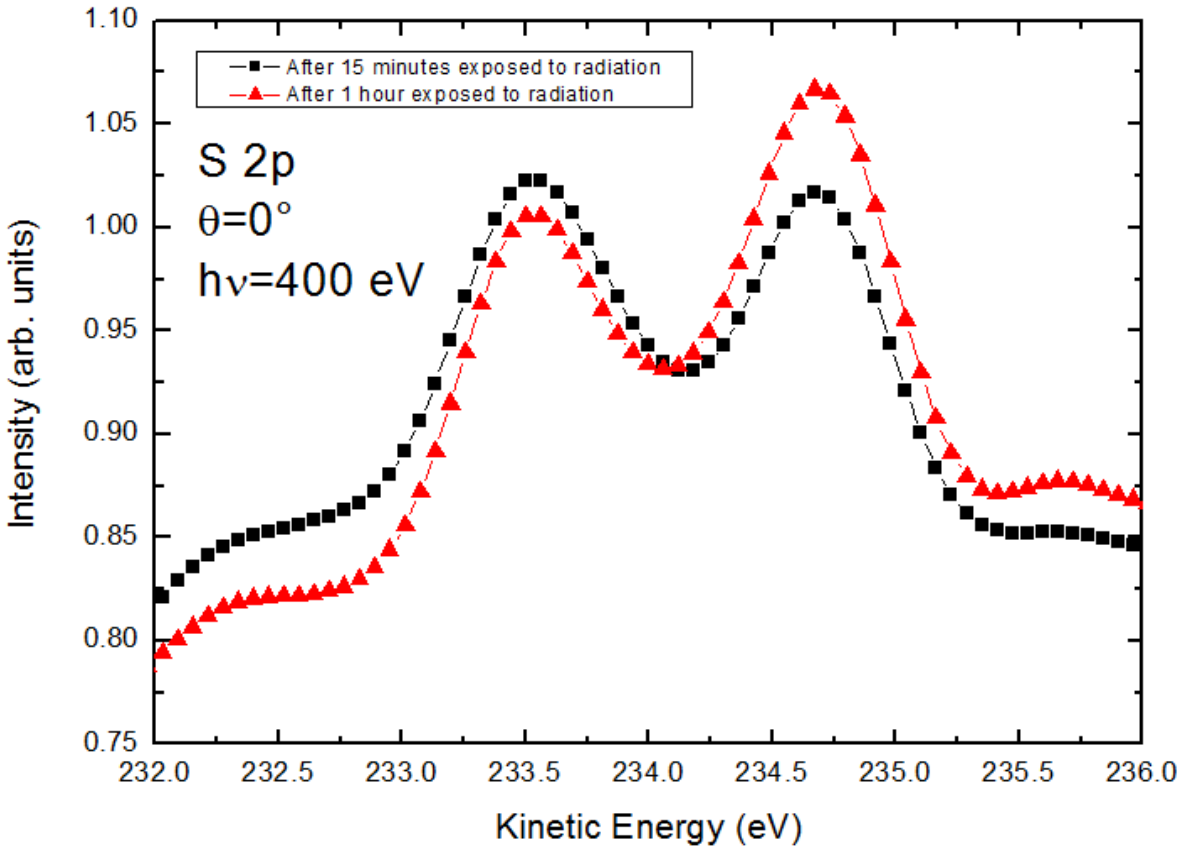

Figure 5.2: XPS spectra recorded from the S 2p signal for a irradiated surface inside the focus of the beamline. Spectra for 15 minutes and one hour of exposure are shown.

effect begins even after a short radiation time. Fig. 5.2 shows the XPS spectra of the S 2p signal after one hour of permanent exposure to radiation. The spectrum shows strong variation in comparison to the unradiated surface shown in Fig 5.1. This leads to the conclusion that even after a short period of time inside the focus, a large amount of molecules is influenced by radiation damage. This strong effect must be attributed to the very brilliant radiation inside the focus at beamline 11 at DELTA.

To reduce the high amount of radiation damage at the surface, it is necessary to reduce the amount of photons per unit area without losing count rate in the detector. Therefore, the idea was developed to reduce the amounts of photons per unit area by moving the experiment setup behind the focus of the beamline. Theoretically, at this position behind the focus, the beamsize should broaden up and thereby reduce the amount of photons per unit area. Fig 5.3 shows calculations for the beamshape of beamline 11 inside the focus and 200 mm behind the focus. The calculations were performed with the program

RAY which was developped at BESSY (Berliner Elektronen-Speicherring Gesellschaft für Synchrotronstrahlung) especially for optical pathways in beamlines.

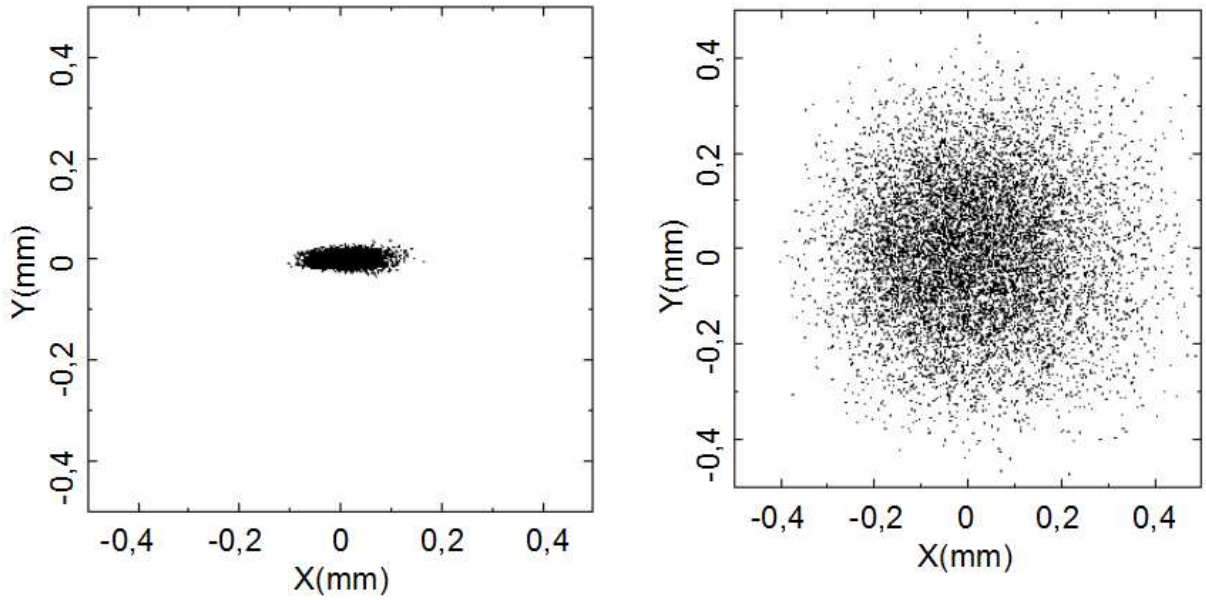

Figure 5.3: Calculated beamshape parameters for the beamline 11 at DELTA inside the focus(left) and 200 mm behind the focus(right).

In Fig. 5.3 it is clearly visible that the beamshape is broadened drastically. The overall intensity of photons at the experiment, however, is not reduced, because the electron analyzer (cf. section 4.3) gathers all emitted electrons in a circular shape of approx. 2 mm around the center of the sample. A variation of the distance to the focus and an observation of the overall count rate showed that it was possible to move the experiment 500 mm behind the focus without losing intensity. At this position, the size of the beamshape was approx. 1 x 0.8 mm^2. This size was determined by a fluorescence screen which was mount at the position of the sample.

At this position, the measurement for the S 2p signal was repeated with a new sample to gather information about the radiation damage there, compared to at the in-focus position. Fig. 5.4 shows the S 2p signal after one hour of exposure to radiation behind the focus.

It is clearly visible that after this procedure the spectrum is almost identical with the spectrum recorded for the unradiated sample shown in Fig. 5.1. This means that at 0.5 m behind the focus, there is almost no radiation damage to the sample. Especially the comparison of Fig. 5.2 and Fig. 5.4 shows the strong change of the radiation damage for the in- and out-of-focus measurements. It should be noted however that after much

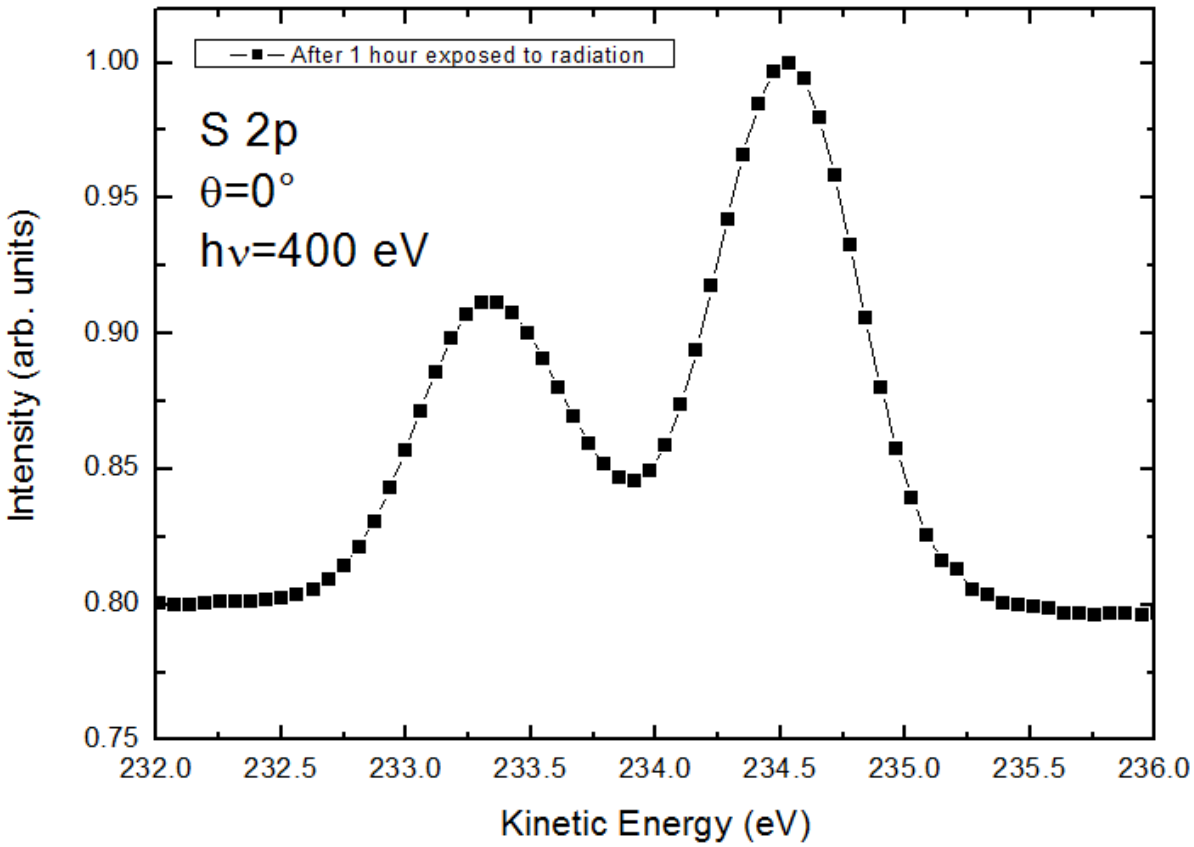

Figure 5.4: XPS spectra recorded from the S 2p signal for a irradiated surface out of the focus of the beamline. The sample was irradiated for one hour

longer radiation times ($> 24h$) the out-of-focus measurement shows a visible change in the spectrum as well. The reduction of radiation damage and therefore capacity for improved measurement provided by out-of-focus measurement is unmistakable, especially if since the molecules studied in this work, cyclopentene and pyridine, are much more stable under radiation. The improvement in stability that this provides should be sufficient to perform radiative-unchanged measurements. For this reason, all measurements presented in this work have been recorded 0.5 m behind the focus of the beamline.

5.2 Clean Silicon

In the analysis of interfaces between an adsorbate and a substrate, it is of great importance to know the exact properties of the substrate used. Especially the quality of the surface and its geometric properties are of great interest. In the case of photoelectron diffraction, it is also important to know the diffraction characteristics of the substrate.

This information is necessary to distinguish between diffraction signals of the substrate and diffraction signals of the interface and adsorbate.

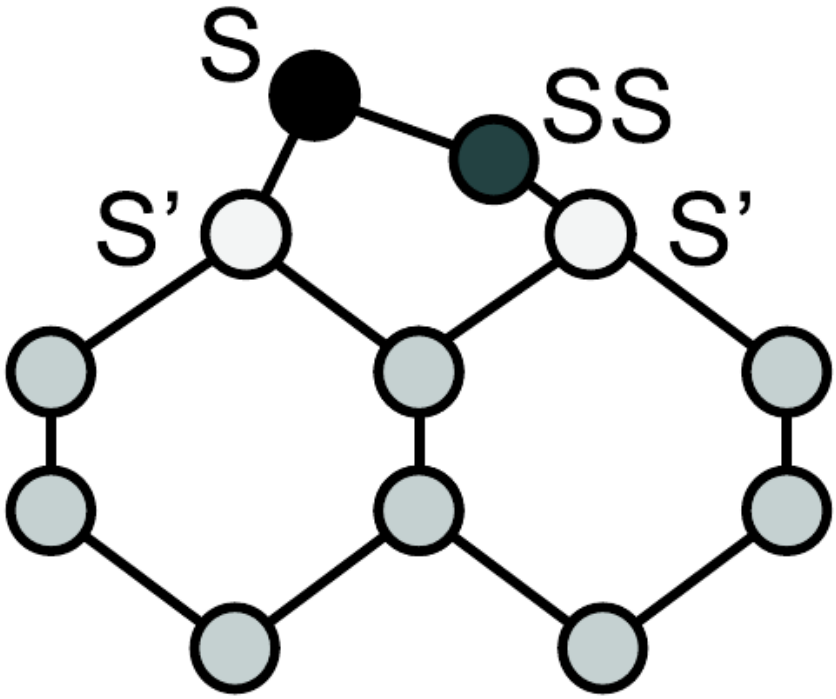

Figure 5.5: Side view of the asymmetric silicon dimer. The uppermost atom is labeled S (Surface), the second atom SS (SubSurface), the second layer S'. The unlabeled atoms belong to the normal bulk structure of a silicon crystal.

For this reason, the clean silicon(100) surface and its reconstruction was studied prior to each experiment. The surface was investigated for impurities with XPS. The reconstruction of the surface was checked by LEED and XPD. A silicon(100) surface typically reconstructs into the so-called 2x1 reconstruction. This reconstruction originates from an asymmetric dimer formed in the uppermost layer of the silicon crystall. The dimer forms because the continuation of the bulk structure is not possible at the transition to the vacuum. Fig. 5.5 schematically shows a side view of such a dimer, including the upper atom (S), the lower atom (SS) and the first layer after the dimer (S') and the bulk. As shown in the figure, the two uppermost atoms building the dimer are tilted and therefore arranged asymmetrically. This asymmetric ordering is energetically favorable over the symmetric arrangement. This was already proposed 30 years ago by Chadi et al [34]. This assumption of asymmetric dimers was afterwards supported by many different experimental methods, including ion-scattering [35–38] , x-ray diffraction [39], transmission

electron diffraction [40] and Scanning Tunneling Microscopy (STM) [41–43]. From the theoretical point of view, many total energy calculations (TEC) [44–49] showed that the asymmetric dimer is energetically favorable by approx. 0.1 eV over the symmetric setup.

This (2x1) reconstruction can be observed by LEED in our experimental setup. Fig. 5.6 shows a LEED-pattern of the reconstructed Si(100) surface for an energy of the incoming electrons of 100 eV. As is visible in the pattern, each second reflex which would belong to a symmetric (1x1) pattern is missing. Additionally, the spots in the LEED are not surrounded by smaller superstructures, which would be an indication for a contamination of the sample or a high roughness. If a LEED pattern of this quality is not observed, the sample is not completely reconstructed or is contaminated and therefore a new sample needs to be prepared.

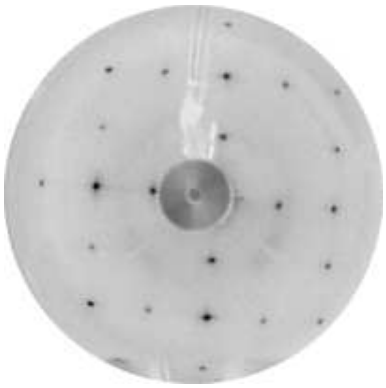

Figure 5.6: Inverted LEED pattern auf the Si(100)-2x1 reconstructed surface recorded for an energy of 55 eV

Fig 5.7 shows the XPS spectrum of the Si 2p signal for the clean and reconstructed surface. Within the energy resolution of the experiment, the spectum could be divided into three components. The components originate from the different atomic environments of the atoms shown in Fig. 5.5. The atoms SS and S' are in this connection combined to one component S', because a separation of these two components is not possible at room temperature. It was shown by Landemark et al. [50] that in the case of low temperature experiments, a separation of this additional component is possible. A spectrum of this quality is an additional precondition to having an adequate sample for the following preparation process. A more detailed discussion of the subcomponents in the spectrum and the fitting parameters will be given in the sections 5.4 and 5.5, along with the discussion of changes due to the adsorbates.

As the final criterion for an excellent substrate surface an XPD is recorded. This pattern gives information about the quality of the surface and the orientation of the

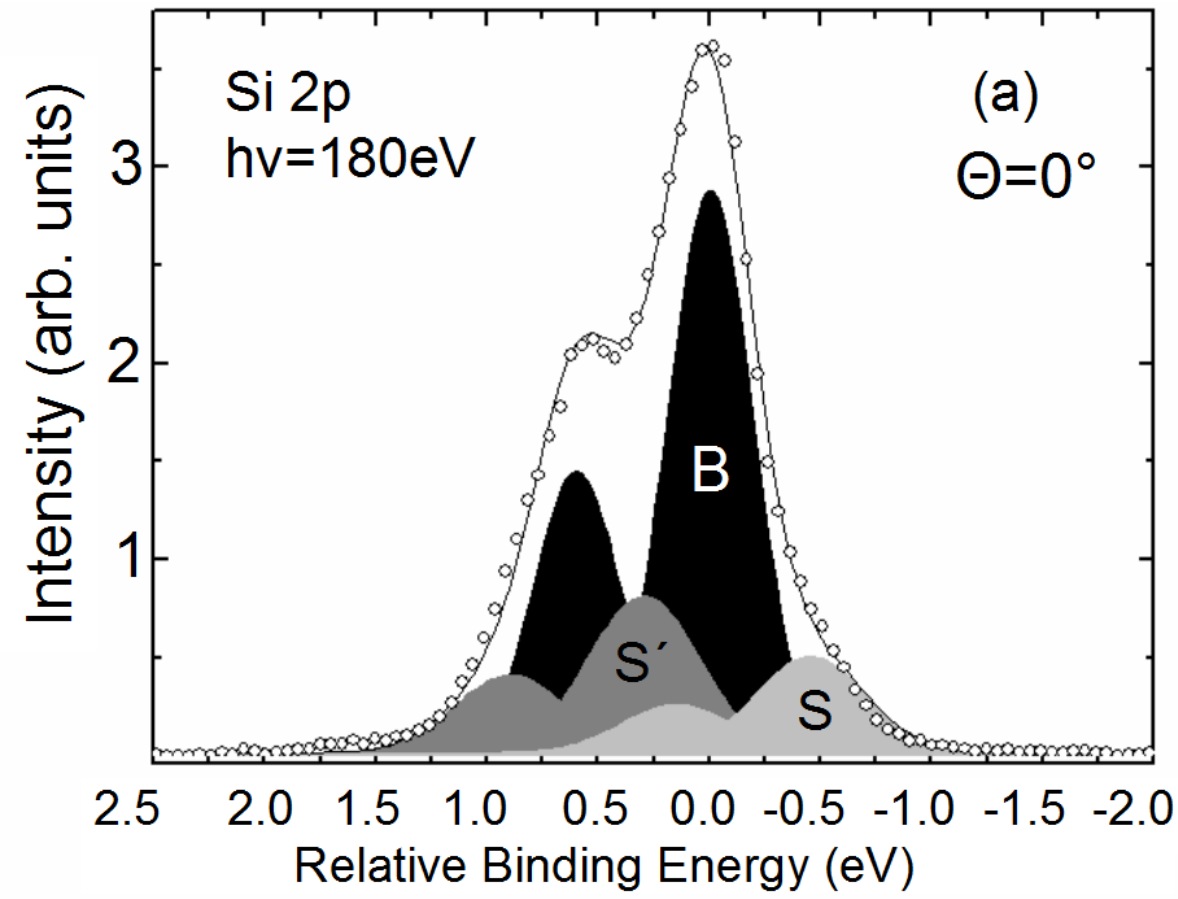

Figure 5.7: Silicon 2p photoelectron signals recorded with a photon energy of $h\nu$=180 eV. The spectra was taken for the clean surface at normal emission

crystal with respect to the analyzer. This information is very important for the following simulation calculation, including, among other things the calculated orientation of the adsorbed molecules. Fig. 5.8 shows a typically diffraction pattern of the clean and (2x1)-reconstructed Si(100) surface recorded for an energy of $h\nu = 240eV$.

The characteristic signature of the diffraction pattern, particularly the fine structure elements, are a reliable criterion for the quality of the surface and the reconstruction. The forward scattering events at approx. $\Theta = 30°$ and $54°$ are performed along the (110)-axis and are therefore a criterion for the orientation of the sample.

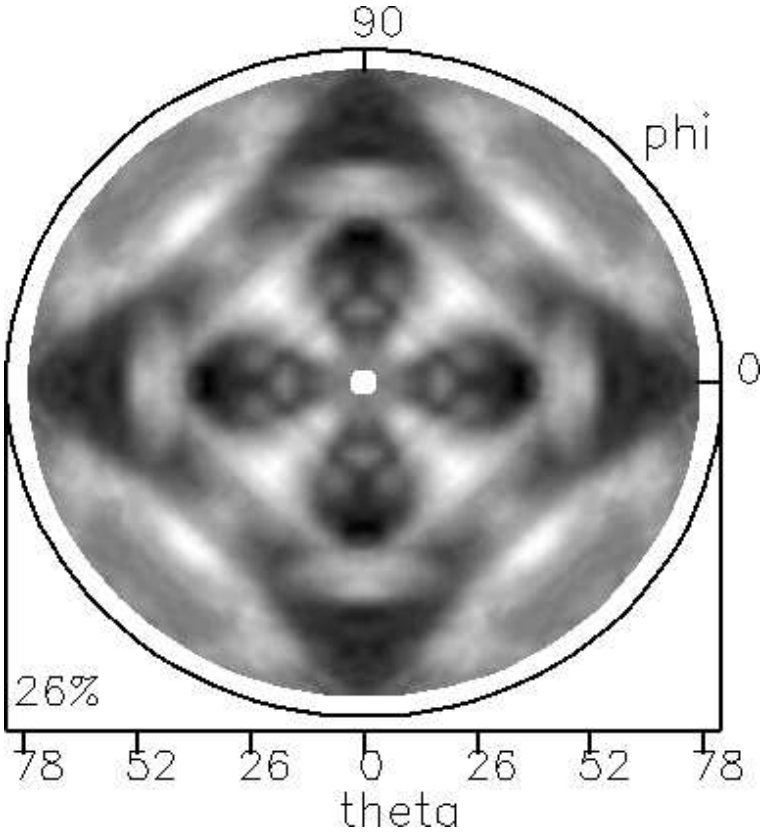

Figure 5.8: XPD pattern of the clean Si(100) 2x1 reconstructed surface recorded at a photon energy of $h\nu$=240 eV [51]

5.3 General Reactions between Organic Molecules and Si(100)

5.3.1 Hydrocarbons

Organic reactions like cycloaddition reactions could be applied to explain surface functionalization [1]. For the formation of carbon-carbon bonds, during the synthesis of new molecules, cycloaddition reactions are widely used because of their high stereoselectivity and versatility [52–54]. During a cycloaddition reaction, two π bonded molecules form a new cyclic molecule while losing two π bonds and creating two new σ bonds. The reactions are characterized by how many π electrons are involved in the reaction. In Fig. 5.9 an example for the [2 + 2] and the [4 + 2] cycloaddition reactions is depicted. One line represents a single bond, while a double line indicates a double bond between the atoms, respectively. In the [2 + 2]-reaction, two π electrons of each ethylene molecule are involved in the reaction. The [4 + 2]-reaction (Diels-Alder reaction [52]) is shown in Fig.

5.9 on the right for a "diene" molecule with two conjugated π bonds, butadiene, and one alkene, ethylene, to form a six-member ring.

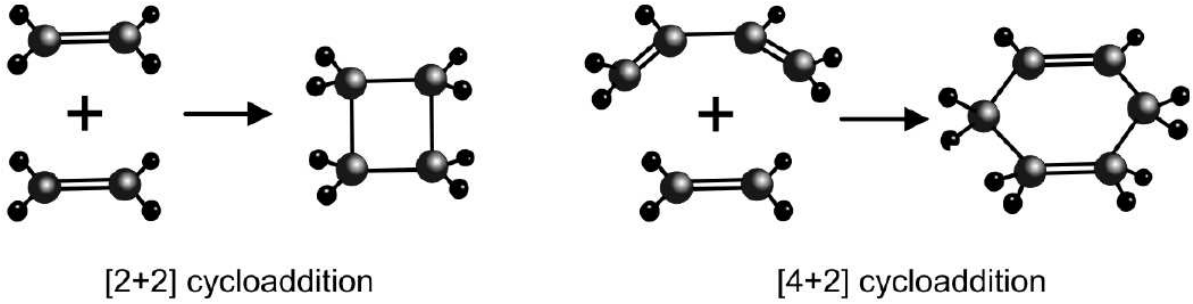

Figure 5.9: Examination of two cycloaddition reactions by frontier orbital analysis. The [2+2] cyloaddition between two alkenes resutls in a four membered ring, wheres as the [4+2] cycloaddition between an alkene and a diene resutls in a six membered ring [1].

Cycloaddition reactions follow the "Woodward-Hoffman" selection rules, which stem from an analysis based on the frontier orbital theory. It deals with the symmetries of the highest occupied (HOMO) and the lowest unoccupied molecular orbital (LUMO) of the reactants during the formation of a new reaction product. This theory about the frontier orbital theory was composed by Woodward and Hoffman, and they are widely used for the prediction of how readily an organic reaction will occur, see [55].

Regarding the "Woodward-Hoffman" selection rules, the light and dark gray lobes in Fig. 5.10 represent positive and negative lobes and have to overlap "in phase". This means for a "symmetry allowed" reaction the lobes must have the same color. This is not the case for the [2 + 2] cycloaddition reaction which is "symmetry forbidden" be- cause of the particular properties of the [2 + 2] reaction (see Fig. 5.10). This reaction does not occur without a significant activation energy and in organic chemistry is largely limited to synthesis involving photochemical activation. The [4 + 2] cycloaddition, however, instead is allowed by the frontier orbital symmetry. The Diels-Alder reactions are commonly used for the formation of new C-C bonds in organic synthesis [1]. An analogy discussion of a cycloaddition reaction occurring between an organic molecule and the Si(001)(2 x 1) reconstructed surface is given below.

The first examples of what can be categorized as [2+2] type cycloaddition reactions occurring between an alkene and a silicon surface were reported the late 1980's. Alkenes such as ethylene, as well as the related alkyne (triply bonded) molecule acetylene, were reacted with the clean Si(100) 2x1 surface in vacuum [56–62]. The alkenes were found to

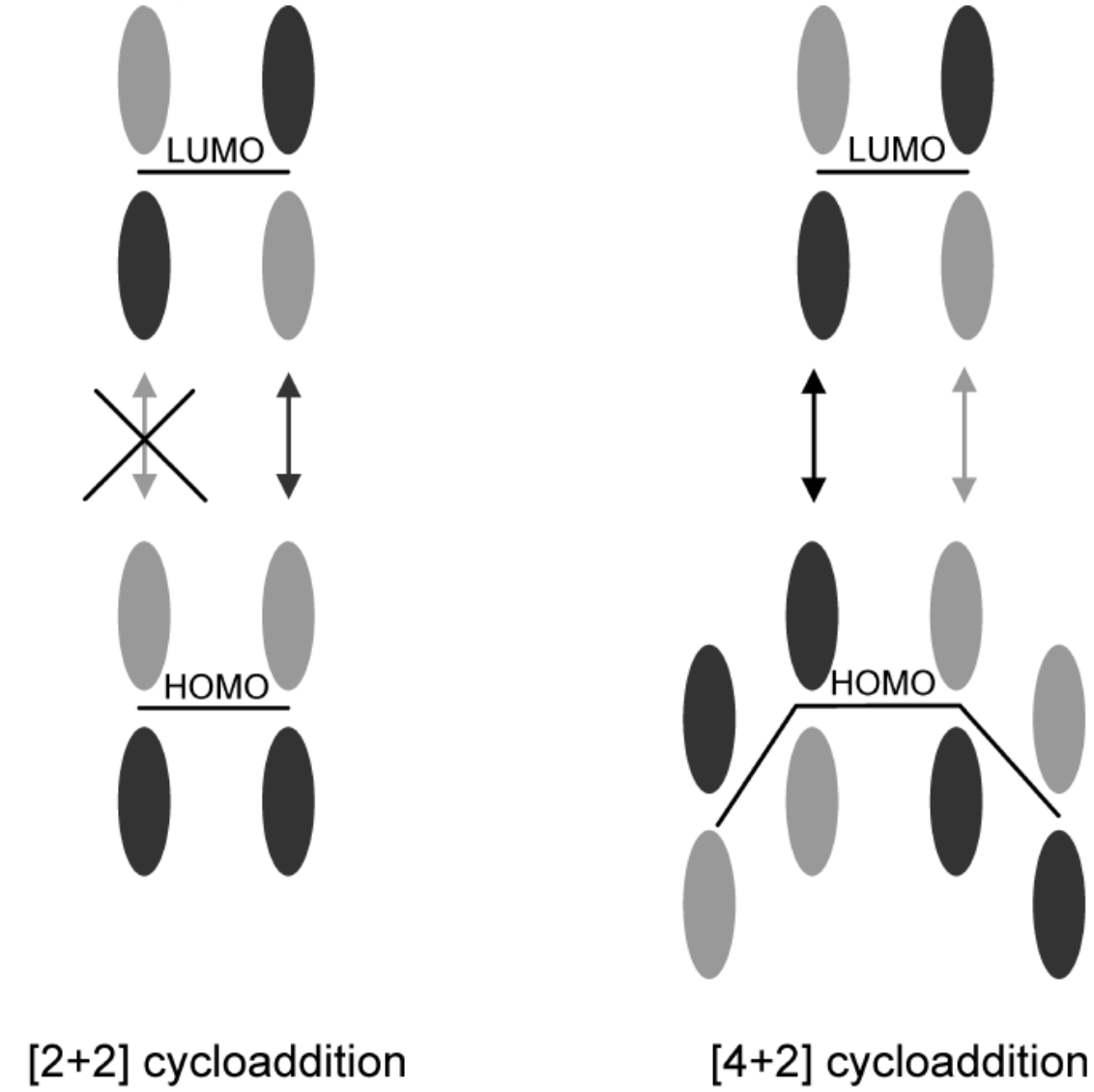

Figure 5.10: Schematic drawing of reaction kinetics follwowing the frontier orbital theory. The highest occupied (HOMO) and lowest occupied (LUMO) molecular orbits are represented by the dark and light gray lopes. Following the frontier orbital theory only slopes of the same color are allowed for a combination. [1]

chemisorb at room temperature, forming stable species like that shown in Fig. 5.11(c) that "bridge-bonded" across the silicon dimers on the surface. The reaction proceeded by formation of two new σ bonds between Si and C atoms, hence the bonding was referred to as di-σ bonding. In addition, it was shown that while the π bonds of the alkene and of the Si-Si dimer are broken, the σ bonds remain intact [63–65]. With this kind of reaction product formed, one can draw a direct analogy with the surface adsorption of the alkene (Fig. 5.11) and the [2+2] cycloaddition reaction shown in Fig. 5.9(a). Just

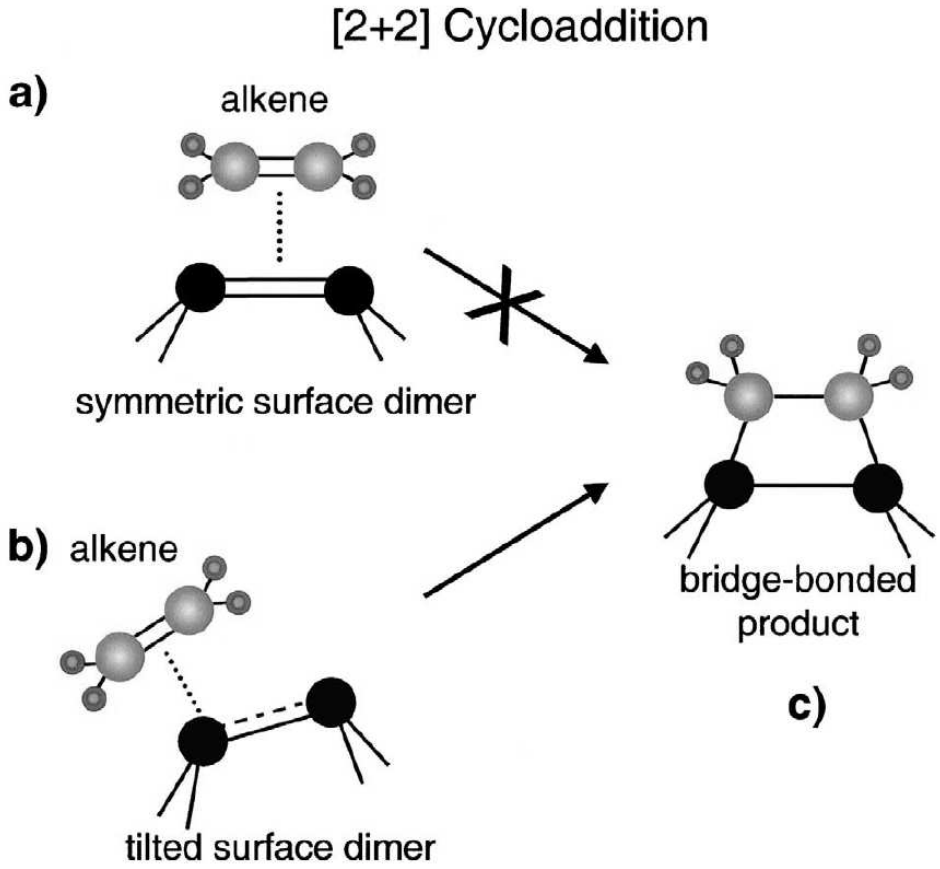

Figure 5.11: A [2+2] reaction at the silicon surface occurs between an alkene molecule and the silicon dimer. The product is bridge-bonded across the dimer. [1]

as two ethylene molecules (CH2=CH2) react to form a four-membered cyclobutane ring, ethylene reacts with the silicon dimer (Si=Si) on the Si(100)-2x1 surface to form a four-membered $Si_2(CH_2)_2$ ring with the surface. Interestingly, the surface [2+2] cycloaddition is a relatively fast reaction, occurring readily with most alkenes at room temperature [66]. This high reactivity would not be expected for a true symmetric [2+2] reaction, which formally is symmetry forbidden and is slow for the analogous homogeneous reaction [54,55]. The symmetry analysis shown in Fig. 5.10, however, applies to a system in which the Si dimer is symmetric and closely mimics an alkene. This is the pathway illustrated in Fig. 5.11(a). However, the Si dimer is not symmetric in its lowest energy configuration. The lowest energy state of the Si(100)-2x1 surface is actually one in which the silicon dimers are tilted. It has been proposed that this low symmetry (tilted) geometry allows the reaction to proceed through an asymmetric pathway in which the alkene approaches the dimer from one side, as shown in Fig. 5.11(b) [67,68]. This asymmetric approach is of a lower symmetry and can occur with little or no energetic barrier. This example serves as an interesting case of a solid state effect in the silicon (tilting of the dimers) controlling a

surface reaction (via relaxation of the symmetry constraints). The result of the [2+2]-like reaction is a tightly bonded organic group, directly attached to the silicon surface through strong Si-C bonds (82kcal/mol each [69]), as illustrated in Fig. 5.11(c). Furthermore, as reported above, the reaction occurs readily for many alkenes. Consequently, [2+2] cycloaddition has attracted much attention as a means to functionalize the Si(100)-2x1 surface.

5.3.2 Nitrogen Containing Molecules and Si(100)

Although it is now established that the π-bonds of the Si(100)-2x1 surface react with a wide range of organic molecules, there has been less investigation into utilizing the zwitterion-like diradical character of the silicon dimers. The tilting of dimers on the surface results in a charge separation between the two Si atoms in a dimer. The down atom of the tilted dimer has a slight positive charge relative to the up atom, introducing some zwitterionic characteristics into the weak π-bond of a dimer. The interaction of methylamine NH_2CH_3 with the Si(100)-2x1 surface provides an example of a zwitterionic-type reaction. Previous experimental and theoretical studies have shown that methylamine first adsorbs molecularly onto the Si(100)-2x1 surface into an NH_3 precursor state, followed by scission of an N-H bond to produce surface $NHCH_3$ and H species. The formation of the NH_2CH_3 (Fig. 5.12 (left)) precursor state involves the interaction between the lone pair of the NH_3 molecule and the electron-deficient down atom of the Si dimer, and the molecular adsorption is essentially a Lewis acid-base reaction.

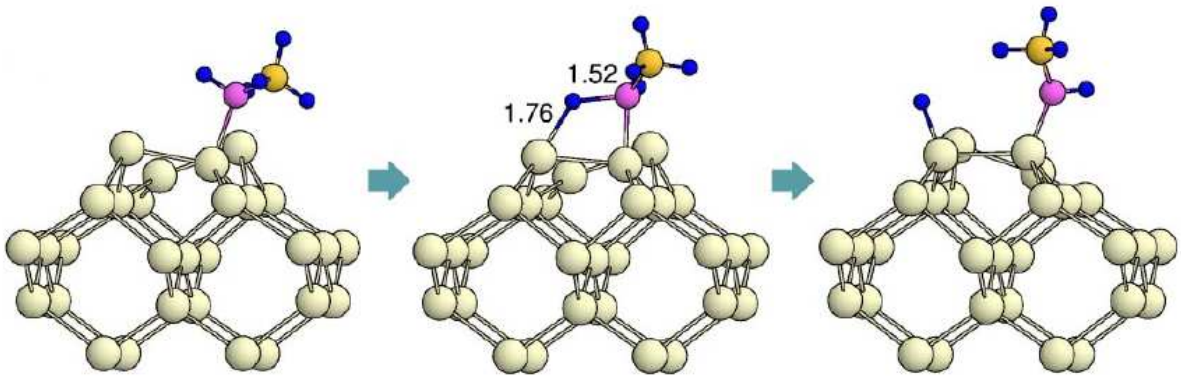

Figure 5.12: Atomic geometries of the molecular (left), transition (middle), and dissociative (right) states along the reaction pathway of an N-H dissociation. [70]

Afterwards, the interaction follows the reaction pathway leading to the energy minimizing state of the system. The same type of starting reaction was observed for the simpler system ammonia (NH_3), however, the final adsorption state still consists of an NH_3 and buckling configuration of Si dimers is unchanged. This adsorbate-induced buckling switch allows an alignment of the dissociated $NHCH_3$ species along the dimer row, contrasting with a zigzag structure observed in ammonia dissociation. This interesting difference between very similar molecules lead to the assumption that in the case of more complex molecules, the adsorption geometry can differ a lot, due to competing adsorption effects at the dimers. In the case of pyridine, which is studied in this work, the competing effects of the zwitterionic characteristics of a dimer and the cycloaddition process (cf. section 5.3.1) leads to twelve possible adsorption geometries, which must all be included in the analysis.

5.4 Cyclopentene on Silicon

Among the many possible combinations of unsaturated hydrocarbons on the Si surface, cyclopentene is one of the interesting systems where key questions of the hydrocarbon adsorption on Si can be studied in detail. The bonding of the molecules to the surface occurs very often as a chemisorption process, which may appear for selected systems in defined molecular adsorption sites. This feature is highly desirable for the detailed study of the driving forces between the molecules and the surface, in order to understand the adsorption process and to contribute to the development of molecular devices [66]. The chemisorption of unsaturated hydrocarbons on the Si(100) surface results in the so called [2+2]-cycloaddition [71, 72], where one C=C double bound reacts with a silicon dimer. Generally, the cycloaddition describes the reaction of two unsaturated systems resulting in a ring closure. The prefix [2+2] denotes the number of participating π-electrons from each molecule. In a [2+2] cycloaddition, two π-electrons of the hydrocarbon molecule react with two π-electrons of the Si-dimers (for a more detailed description cf. section 5.3.1).

If two C=C double bonds of the same molecule react with Si-surface dimers, a so-called dual [2+2]-reaction is obtained [73]. Consequently, the [2+2] cycloaddition reaction is believed to result in an upright configuration of the molecule at the surface, whereas the dual [2+2]-reaction leads to a flat configuration. Another possible bonding of the molecule to the surface is a "Diels-Alder"-reaction, a [4+2]-cycloaddition of benzene on

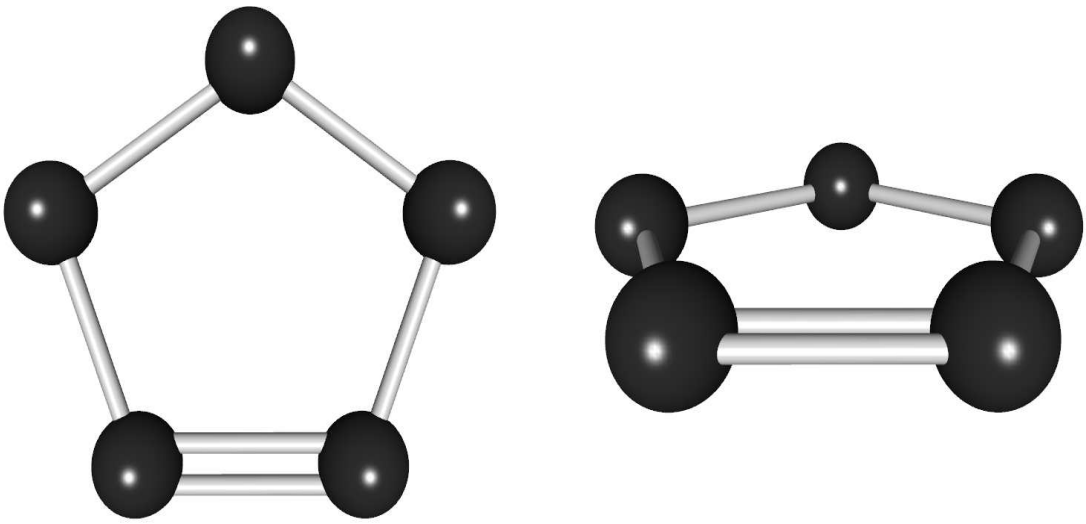

(a) top view (b) side view

Figure 5.13: Schematic of the cyclopentene molecule

silicon [74]. This [4+2]-reaction path leads to a mixture of standard butterfly ([2+2]) and a tilted bridge([4+2]) configuration [75, 76]. Although the principal reaction types of the different molecules are understood quite well, a more detailed experimental observation of the adsorption geometry and chemical bonding is missing for most of the molecules. From the scientific point of view, this information is important for continuing experiments on these systems [77].

In the present work, cyclopentene was chosen for the systematic study of the hydrocarbon to the Si surface because it contains only one C=C double bond, and therefore the competitive dual [2+2]- and [4+2]-reactions are not possible. In the case of cyclopentene on Si(100), a direct [2+2] cycloaddition reaction is thermally forbidden according to the frontier orbital theory [55]. Even so, the final adsorption state of the reaction is [2+2]-like, the reaction is mediated in two steps conducted by the asymmetric silicon dimers. The dimers act as a Lewis base and Lewis acid [78]. Several experimental and theoretical studies including STM, XPS, and infrared adsorption spectroscopy [79,80] as well as DFT calculations [81] have been performed at this system, but the structure at the interface is still unknown.

A very powerful method to study the interface of adsorbed molecules on surfaces is x-ray photoelectron diffraction [6–8]. The combination of core-level photoemission with

polar- and azimuthal-angle variation provides an excellent tool to investigate surface and interface properties in terms of bonding and structure. Additionally, high-resolution XPS-spectra recorded with synchrotron radiation provide sufficient resolution for a detailed analysis. The analysis of the angle-scanned Si 2p and the C 1s XPS signals clearly provides information about the chemically shifted components on the system, the remaining density of silicon dimers, and the vibrational states of the carbon atoms. The comparison of experimental XPD patterns with simulations for various possible structures allows a detailed picture of the local structure around the carbon atoms' bond to the silicon surface to be obtained. In this experimental study, the geometric parameters of the system are determined for the first time, including atomic distances and tilting angles between the different layers. These parameters allowed us to draw a coherent picture of this system, including adsorption sites and structural parameters.

5.4.1 XPS Analysis

All samples were cut from a single-crystalline, boron-doped Si(100) wafer with an orientation better than 0.5°. The in-situ preparation procedure was started by degassing sample and sample holder at approximately 700°C for 6 hours. Afterwards the sample was flash heated at 1050°C in order to remove the native SiO_2 and cooled down slowly to prepare a (2x1)-reconstructed silicon surface. During the procedure the pressure was kept below $5 \cdot 10^{-10}$ mbar. The surface reconstruction and the absence of any impurities were checked by LEED, XPS, and XPD, respectively (cf. section 5.2). The sample was exposed to $1 \cdot 10^{-6}$ mbar partial pressure of cyclopentene for 10 minutes at room temperature which is an efficient pressure to achieve a saturation coverage [79]. A survey spectra which was recorded for the clean surface after the preparation procedure, is shown in Fig. 5.14.

Figure 5.15 shows Si 2p XPS spectra of the clean surface (a,b) and after the adsorption of cyclopentene (c,d). Normal emission spectra and spectra recorded with 60° with respect to the surface normal are compared. Three doublets are contained in the spectra of the clean surface and will be discussed below. After cyclopentene adsorption, a fourth doublet arises due to an additional Si-C bond. Within a doublet, the intensity ratio of the Si $2p_{3/2}$:Si$2p_{1/2}$ component was set to 2:1. The binding energy separation within a doublet was set to 0.60 eV. These values were kept constant through our analysis and they are in excellent agreement with values available in literature for room temperature studies [82, 83]. The relative binding energy shifts for the different doublets are summarized in Table 5.1.

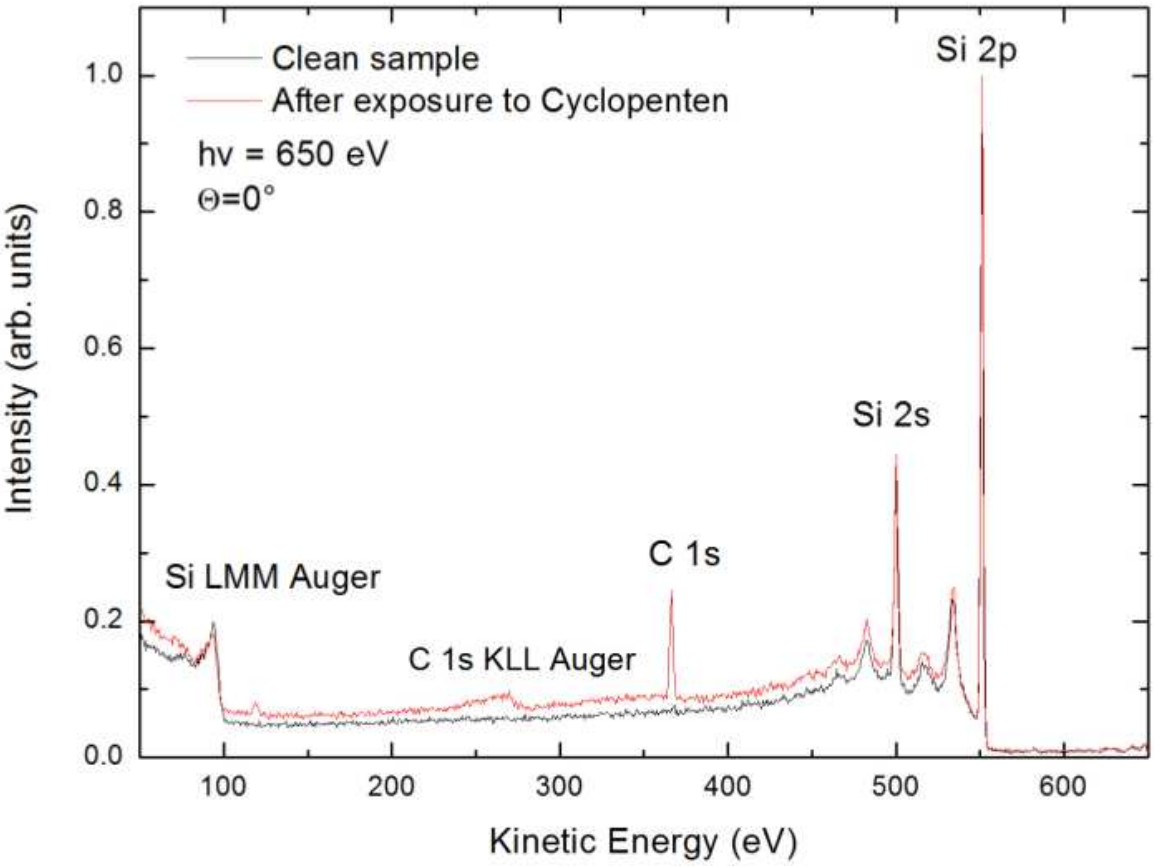

Figure 5.14: Survey spectra for the clean silicon surface and after the preparation was finished.

Silicon	B	S	S'	Ad
relative shift (eV) 0°	0.0	-0.45	0.30	
relative shift (eV) 60°	0.0	-0.45	0.30	
Silicon+Cyclopentene				
relative shift (eV) 0°	0.0	-0.45	0.30	0.78
relative shift (eV) 60°	0.0	-0.41	0.30	0.74

Table 5.1: Relative binding energy shifts of the spectral components displayed in Fig. 5.15. All energy shifts are related with respect to the Si 2p bulk component.

The four components B, S, S', and Ad are attributed to the bulk, upper dimer atom, lower dimer atom + sub-surface, and the adsorbed cyclopentene, respectively. The spectra of the clean surface are displayed in Fig. 5.15(a) and (b). The observed relative energy shifts with respect to the bulk signal are 0 eV, -0.45 eV, and 0.30 eV for the (B), (S), and (S') components, respectively. These values are in excellent agreement with previously

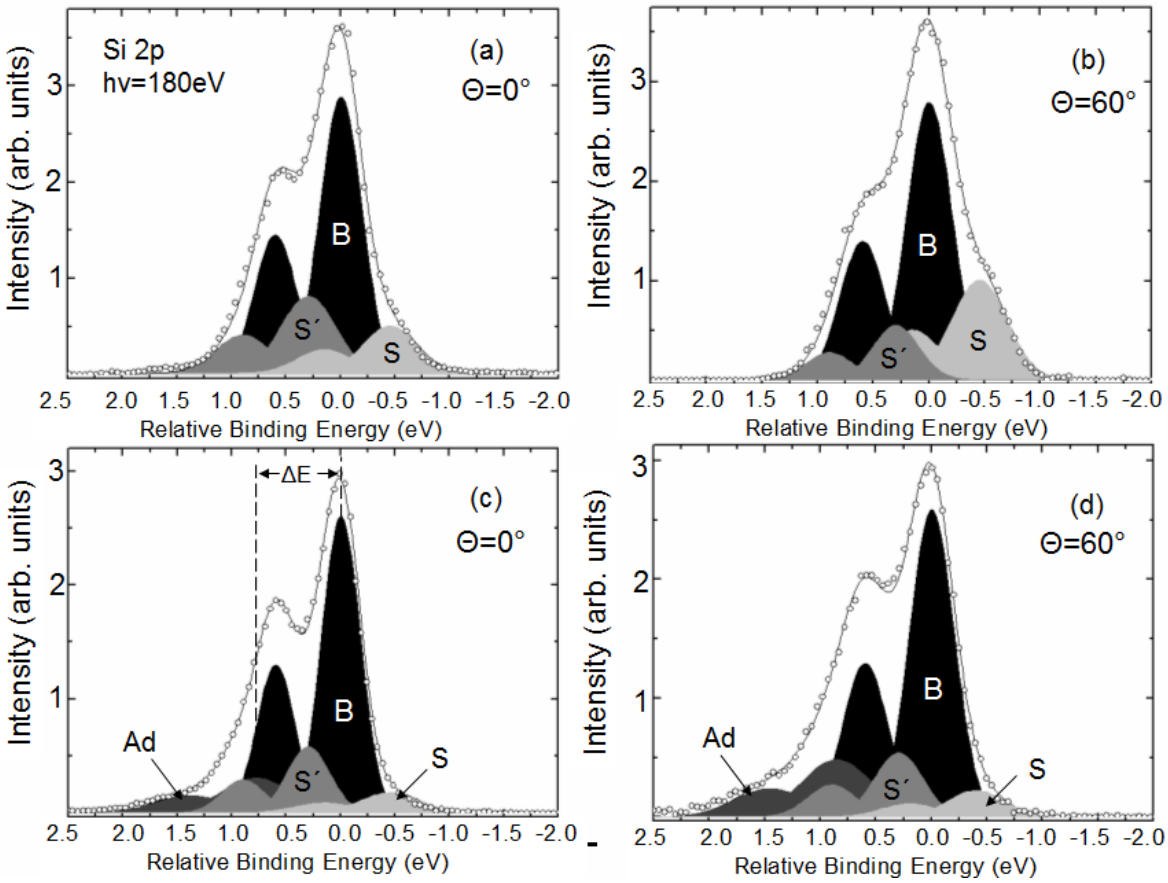

Figure 5.15: Silicon 2p photoelectron signals recorded with a photon energy of $h\nu$=180 eV The spectra were taken for the clean surface at normal emission (a), the clean surface at 60° with respect to the surface normal (b), cyclopentene-coated surface at normal emission (c), and for the cyclopentene-coated surface at 60° with respect to the surface normal (d). The different components are discussed in the text. The fitting parameters are displayed in Tab. 5.1

reported results [82,83]. Also, we tried a deconvolution into five components, as suggested by Landemark [50] for studies at 200 K. In our investigation, the residuum was not improved when trying five instead of three components in the least squares fit. A possible explanation for this finding could be that our spectra were recorded at room temperature while studies of Landemark et al. [50] were performed at 200 K. As expected, the relative intensity of the upper dimer atom compared to the bulk intensity increases at higher polar angles due to higher surface sensitivity. For the chemisorbed surface, the line-shape of the Si 2p intensity changes drastically. First, an additional component resulting from the adsorbed cyclopentene appears in the spectra, and secondly, the components belonging to the silicon dimers are strongly quenched. However, the relative energy shifts

of the remaining components B, S, and S' are the same as observed for the clean surface. The new component "Ad" is shifted by ΔE=+0.78 eV to higher binding energies. The experimental finding of only one additional component in the spectra is a hint of only one adsorption site of the carbon silicon bonding. In the spectra, different photoelectron intensities are displayed at emission angles of $\Theta = 0°$ and $\Theta = 60°$. The very small energy shift observed in the components S and Ad for the spectra recorded at 60° in comparison to the spectra recorded at 0° may be explained due to the different electronic environment of electrons emitted in normal emission and at higher polar angles. The differences in the spectra before and after adsorption at various angles contains additional information. Before cyclopentene adsorption, the intensity ratio of the S peak to the bulk signal is ∼17% and ∼36% for normal emission and for $\Theta = 60°$, respectively. After adsorption, the ratios change to ∼6% and ∼9%, respectively. This observation clearly indicates that about ∼75% of the silicon dimers are destroyed during the adsorption process. It is a first spectroscopic indication of the cyclopentene reacting with silicon dimers during the adsorption process. However, some of the silicon dimers seem to remain intact even after adsorption. A comparison of the "Ad" peak recorded at normal emission and at $\Theta = 60°$ shows a strongly increased intensity at higher polar angles. This finding can be explained by a bonding of cyclopentene carbon atoms to silicon atoms in the topmost layer only. Further, this also indicates a nearly complete surface coverage, because the existence of small islands of adsorbed molecules would result in a much smaller change in the intensity ratio of the different components.

Figure 5.16(a) and (b) show the C 1s XPS spectra for normal emission and $\Theta = 60°$, respectively. In the analysis of the carbon 1s signal of unsaturated hydrocarbons vibrational splittings resulting from the C-H molecular bonds have to be included. The effect of vibrational splittings on the spectroscopic signal was shown both for gaseous [16–19] and adsorbed molecules [20,21]. An accepted argumentation explaining this effect in XPS spectra can be achieved by the application of a linear coupling model with a Frank-Condon process [20] as the excitation process. For the fitting procedure the linear coupling model is realized via a composition of three Voigt functions that are equally spaced by ΔE in energy. The intensity of each function is given by $I_n = e^{-S}S^n/n!$, where the factor S is defined as $S = \delta^2\mu\omega/2\hbar$ [20] and n=0,1,2. The parameters δ, μ, and ω describe the normal coordinate of the core excitation, the reduced mass, and the vibrational frequency, respectively. A more detailed description of the line shape profiles can be found in section 2.2.2. Within the linear coupling approximation the carbon 1s line is divided into two chemically different components. The component found at higher

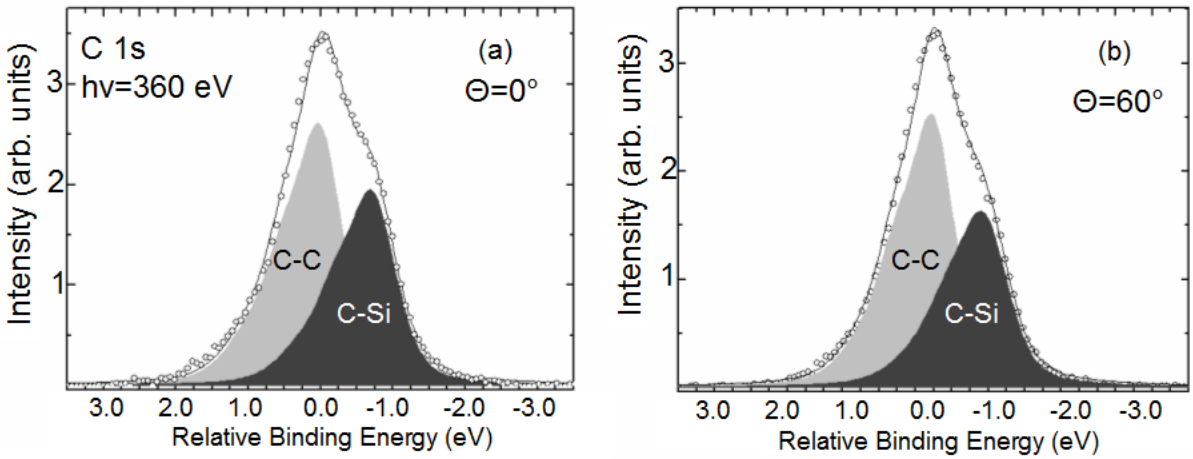

Figure 5.16: (a) Carbon 1s photoelectron signals recorded at a photon energy of $h\nu$=360 eV. The spectrum recorded at normal emission (a) is compared with the spectrum obtained at 60° with respect to the surface normal. A summary of the different components is presented in Tab. 5.2 and in the text.

binding energies is assigned to the carbon-carbon (C-C) bonds and the component at lower binding energies to silicon-carbon (Si-C) bonds. The parameters used for the fitting procedure are presented in Table 5.2.

	relative shift (eV)	ΔE (eV)	S	W_G (eV)	W_L (eV)
C-C	0.00	0.45	0.40	0.30	0.16
Si-C	-0.71	0.45	0.42	0.30	0.16

Table 5.2: Relative binding energy shift of the spectral components as presented in Fig. 5.16. The relative energy shift is given with respect to the C-C position. The parameters W_G and W_L are the FWHM of the Gaussian- and Lorentzian part of the Voigt profile. The parameters ΔE and S resulting from vibrational effects [20] are discussed in the text.

Within the fitting procedure, over 7000 individual spectra which had been recorded within this photoelectron diffraction pattern were evaluated. The diffraction pattern were recorded for an azimuthal and polar range of 0° to 358° and 0° to 80°, respectively. The step-width of 2° was kept constant for both angular settings. Results from our fitting procedure agree well with previous studies for C-H stretching modes [16–21]. The Si-C and C-C intensity ratio was determined to be ∼70% and ∼60% for $\Theta = 0°$ and

$\Theta = 60°$ emission angles, respectively. The observed lower value at a high polar angle can be explained by the increased surface sensitivity at these angles. This dependence of the photoelectron intensity on the emission angle indicates that the C-C bonds are presumably located in a different layer to those carbon atoms bound to silicon, which in fact is an adsorption site above the Si-C layer. At normal emission the intensity ratio is nearly 2:3 which shows that two of the carbon atoms are bound to silicon, while the remaining three carbon atoms are not bound to silicon. Summarizing these findings and the absence of further components in the spectra strongly indicates that only an upright configuration of the molecules is realized at the Si(100) surface.

5.4.2 XPD Analysis

Figure 5.17 shows the experimental and simulated photoelectron diffraction patterns of the Si-C component discused above. The diffraction pattern is a plot of the anisotropy function $\chi = [I(\Theta, \Phi) - I_0(\Theta)]/I_0(\Theta)$ [8], where $I(\Theta, \Phi)$ and $I_0(\Theta)$ denote the intensity at the emission direction (Θ, Φ) and the average intensity at emission direction (Θ), respectively. The maximum anisotropy is defined by $\max\chi(\Theta, \Phi)$-$\min\chi(\Theta, \Phi)$, and it is an indication for the strength of the diffraction effects displayed by the XPD pattern. Its percentage is displayed in the lower left corner of the pattern. A detailed description of the XPD procedure and plotting details is also given in sections 2.3 and 3.1.

The experimental pattern presented in Figure 5.17(a) clearly shows strong diffraction effects, with a maximum anisotropy of 21%. In order to obtain structural information from the experimental photoelectron diffraction patterns, simulations were performed using varying starting structures. In order to compare the experimental data with the simulated data an R-factor analysis [84] as an analytical measure was introduced. The R-factor is defined as $R = \sum_i \frac{(\chi_{th} - \chi_{exp})^2}{\chi_{th}^2 + \chi_{exp}^2}$, where χ_{exp} and χ_{th} denote the experimental and simulated diffraction patterns, respectively. In the simulations many different structure models were tested and a certain number of parameters was varied, including bond-length between the atoms and tilt-angles between the bonding directions. The simulations were performed with the MSPHD [9] package, which is an excellent tool for structure investigation. The structure determination was conducted by means of an R-factor minimization with a genetic algorithm. Genetic algorithms are very suitable tools for minizing the R-factor because they avoid local minima and have been widely used with great success in structure determination [85].

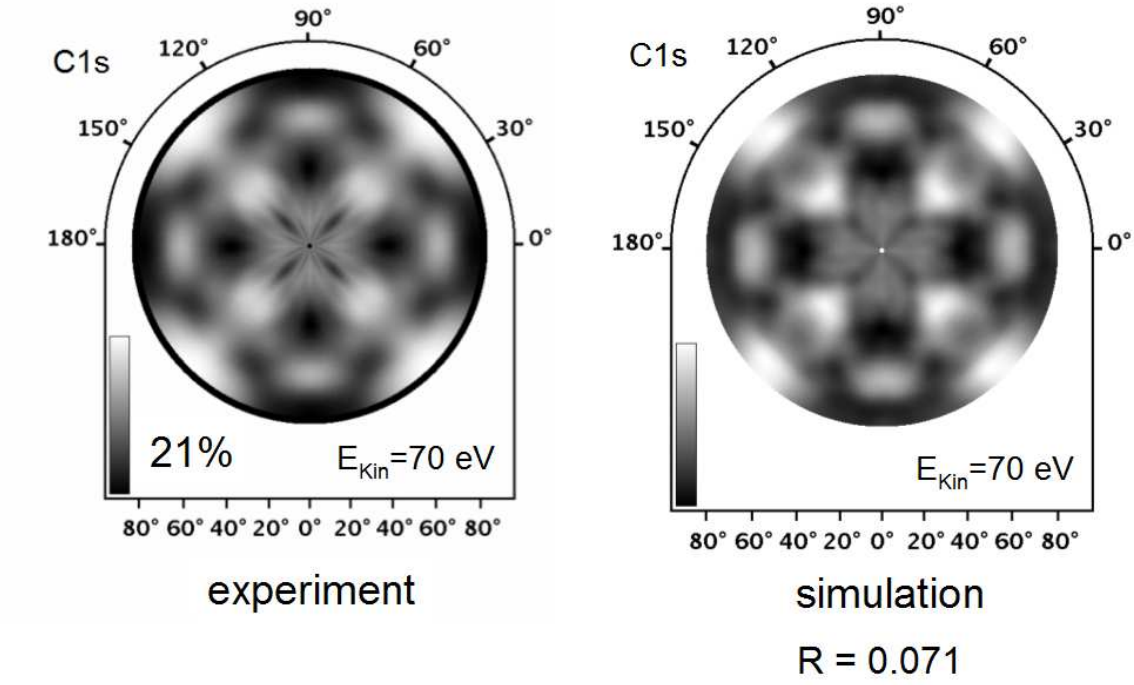

Figure 5.17: Experimental photoelectron diffraction pattern for the C-Si signal discussed in Tab 5.2 (a) and simulated pattern obtained for the structural parameters with the lowest R-factor (b).

In Figure 5.17(b), the best simulated pattern with the lowest R-factor is displayed. This pattern with a minimized R-factor was obtained by the genetic algorithm for various starting parameters of the simulation. All maxima and minima as displayed in the experimental pattern are clearly contained in the simulated patterns. In addition, an R-factor of R=0.07 supports the excellent agreement between experimental and simulated pattern. Figure 5.18 shows the corresponding model structure obtained as a result of the simulation. Fig 5.18 (a) displays a three-dimensional structure model of adsorbed cyclopentene on the Si(100) surface. Two carbon atoms of the cyclopentene are attached to two silicon atoms within a dimer configuration. Figure 5.18 (b) and (c) show the three-dimensional model in a side-view and top-view of the molecule, respectively. Fig. 5.18 (d) displays the two-dimensional projection of the side view of the molecule presenting the definition of the tilt angles between the different layers.

The upright molecule confirms the results of the previous line shape analysis. Also, numerical [81] and experimental [79] studies report an upright molecule. A second indication for this bonding geometry is the decrease of the silicon dimers' signal, as directly

observed in the XPS data and discussed in the previous chapter. The two silicon dimer atoms, which establish the bonding to the cyclopentene molecule are only slightly relaxed from their standard dimer sites. They nearly remain in a dimer site with a shortened distance to each other. The two silicon dimers can be separated into upper and lower dimer atoms at the clean surface, while these atoms are located in the same layer after cyclopentene adsorption. The bonding parameters obtained from the simulations are listed in Table 5.3. The errors reported in Tab. 5.3 are calculated using a 10% variation of the R-factor around the minimum for each of the parameters. For comparison, parameters obtained from a DFT calculation [81] and the parameters of a free molecule [86] are presented, too.

	free C_5H_8	this work	DFT [81]
$d_{C=C}$ (Å)	1.35	1.52 (0.06)	1.58
$d_{C(L1)-C(L2)}$ (Å)	1.51	1.49 (0.08)	1.54
$d_{C(L2)-C(L3)}$ (Å)	1.51	1.53 (0.08)	1.54
d_{Si-C} (Å)		1.88 (0.04)	1.96
d_{Si-Si} (Å)		2.50 (0.15)	2.37
Φ_1 [°]		15.0 (2)	15.0
Φ_2 [°]		24.0 (5)	23.5
Φ_3 [°]		15.0 (9)	13.8

Table 5.3: Distances of the absorbed molecule and the relaxed dimers as obtained from the R-factor analysis. The values of the free cyclopentene molecule and for adsorbed cyclopentene obtained by DFT calculations [81] are shown for comparison.

The difference of the atoms' distance between the first and second layer of carbon atoms is almost the same for the free molecule and for the adsorbed molecule. For the free molecule, the carbon double-bond length is around 1.35 Å; this length is relaxed to 1.52 Å for the adsorbed molecule. A carbon double-bond length of $\sim$ 1.35 Å is the typical value for carbon double-bonds and can be found for many molecules [86]. An increase of the carbon-carbon distance strongly indicates the transition of the double-bond to a single bond, accompanied with the formation of silicon-carbon bond. Another result obtained from the simulation is that the planar geometry of the molecule is lost during the adsorption at the surface. As displayed in Fig. 5.18, the carbon atom assigned as No. "5" is bent above the (110) plane, while atoms No. "3+4" are bent below the (110) plane. The carbon atoms No. "1+2" are directly bound to silicon and they are bent above the (110) plane. The three different angles $\phi_1 = 15°$, $\phi_2 = 24°$, and $\phi_3 = 10°$

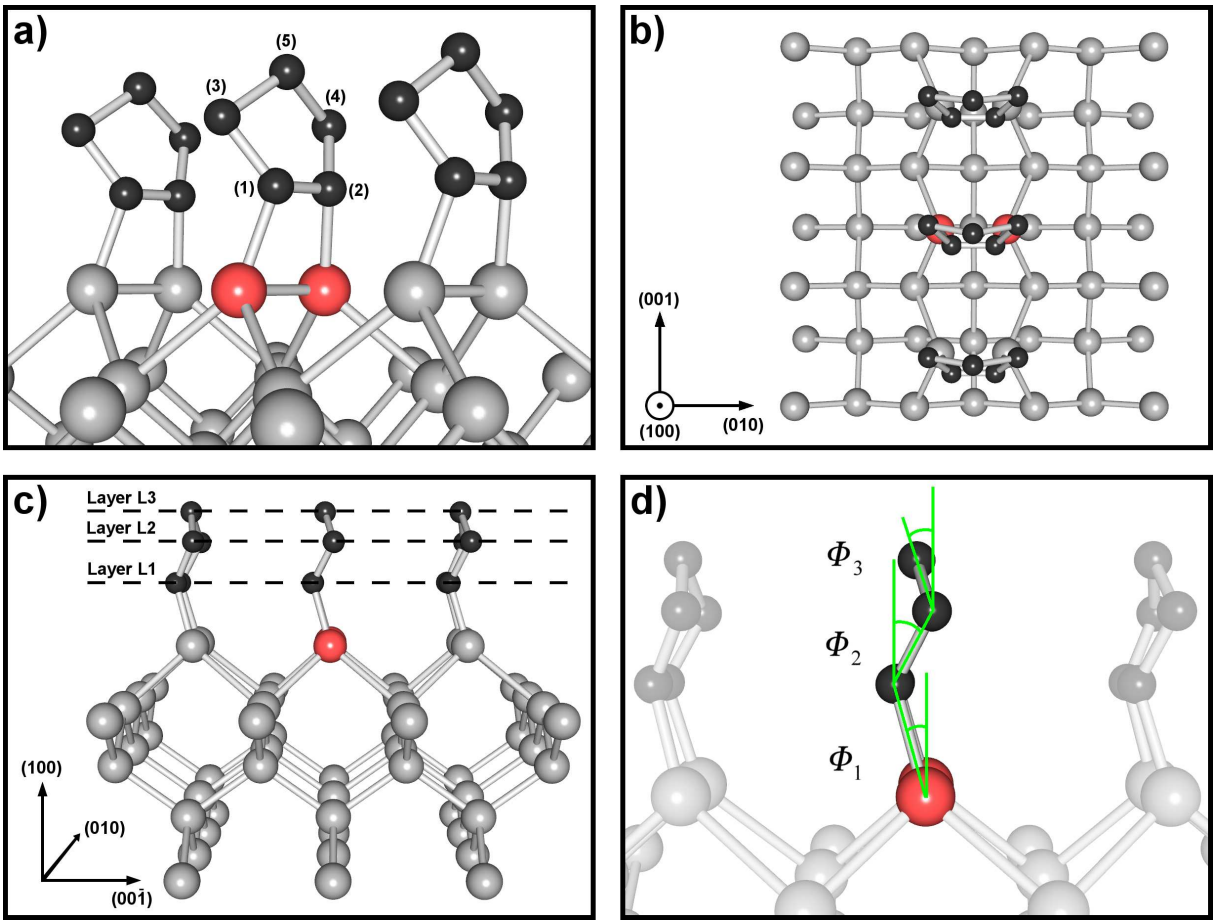

Figure 5.18: Optimized model structure obtained within the R-factor analysis. The hydrogen atoms at the C-atoms are omitted for simplification.

are defined with respect to the (110) plane. A further important finding is the different tilting directions of ϕ_1 and ϕ_3 to the left and ϕ_2 to the right. An inspection of the R-factor analysis regarding the dependence on the tilt angles ϕ_1, ϕ_2, ϕ_3 of the molecule showed a very sensitive variance.

Figure 5.18 shows the dependence of the R-factor on the angles ϕ_1 and ϕ_2. Minima were found at tilt angles of $\phi_1 = 15°$ and $\phi_2 = 24°$. It is clearly visible that a variation of the angles rapidly worsens the R-factor. Apparently, the tilt angles ϕ_1 and ϕ_2 are rather sensitive structure parameters of the adsorbed cyclopentene in Si(100). This is a considerable difference in comparison to other hydrocarbons adsorbed onto silicon where the tilting direction is the same for each layer. For example in the case of cyclohexadiene [21] the molecule conserves its planar geometry after the adsorption onto the surface. When the molecule is adsorbed to the surface, the molecular plane is also kept. Further, all molecules are tilted in the same angle direction with respect to the surface normal.

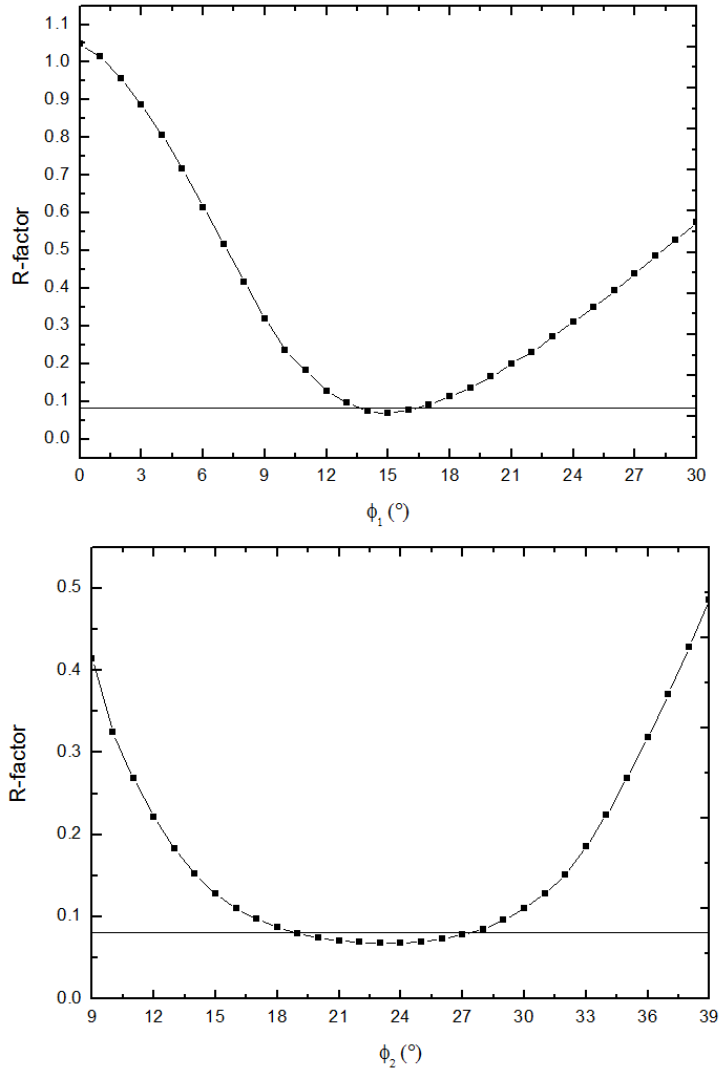

Figure 5.19: R-factor dependence on the angles ϕ_1 and ϕ_2. The variation is shown for $\pm 15°$ around the angle of the best R-factor. The horizontal lines indicates the 10% R-factor variation used for the error determination

5.4.3 Conclusion on Cyclopentene on Silicon

The adsorption of the molecule is mediated by a reaction to silicon dimer atoms. In the XPS spectrum, the Si 2p signal clearly showed a diminished dimer photoelectron signal after adsorption. An analysis of the carbon 1s core level spectra was carried out within the linear coupling model with asymmetric line shape parameters. The line shape confirmed established parameters for the C-H stretching mode and the existence of two chemically different components. We could not find an experimental indication for a third component in the spectra. Within the XPD-analysis, results obtained from model

structures were compared with the experimental diffraction pattern. The XPD-analysis included an automated search for the model structure, including a genetic algorithm for the structure search and an R-factor analysis. From these results we propose an adsorption structure of cyclopentene on Si(100) with an upright configuration.

5.5 Pyridine on Silicon

Among many possible combinations of unsaturated hydrocarbons on the Si surface, molecules containing only carbon atoms have been the most studied. These molecules were used to study key questions of the hydrocarbon adsorption on Si. However inserting an non-carbon atom into the cyclic hydrocarbon ring changes the electric characteristics of the molecule drastically. Therefore, the adsorption behavior of these molecules on Si(100) could differ greatly from the standard molecules and needs to be studied in detail. One very interesting candidate for these molecules is pyridine, which is a benzene-like hydrocarbon with one carbon atom replaced by an nitrogen atom. Pyridine is a six-membered heteroatomic aromatic molecule. Each of the constituent C and N atoms contributes one electron to form a conjugated π system, leaving one lone pair of electrons on its nitrogen atom. A schematic view of the molecule is shown in Fig. 5.20.

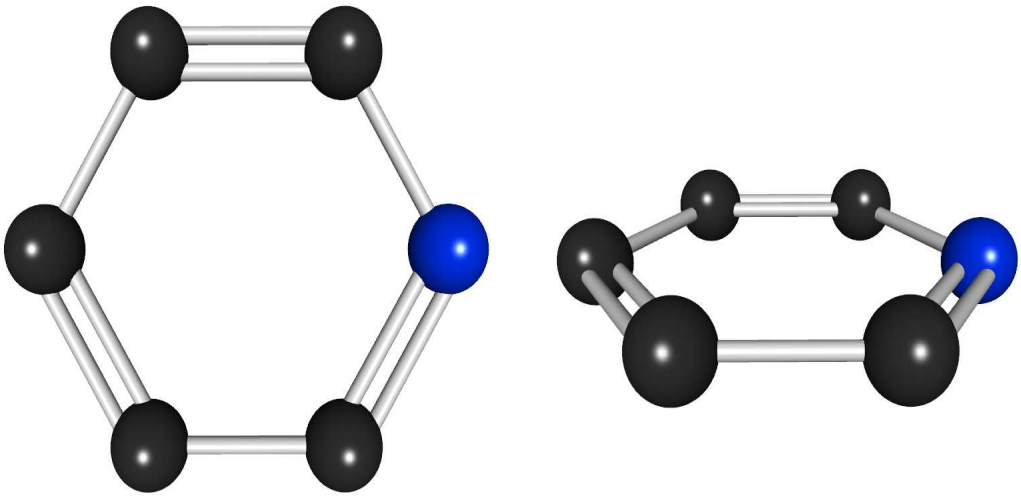

(a) top view (b) side view

Figure 5.20: Schematic of the pyridine molecule

The bonding of the molecules to the surface occurs very often as a chemisorption process, which results in defined molecular adsorption sites. This feature is highly desirable for the detailed study of the driving forces between the molecules and the surface, in order to understand the adsorption process and to contribute to the development of the molecular devices [66]. Due to the benzene like structure of pyridine the adsorption on Si(100) could be expected through [4+2]-like and/or [2+2]-like cycloaddition pathways, where the pyridine could be expected to react with Si(100) through the established [4+2]-like and/or [2+2]-like cycloaddition, forming two Si-C and/or Si-N sigma bindings. In addition, the lone-pair electrons localized on the nitrogen atom may possibly act as an electron donor to form the dative bond with the electron-deficient buckled-down Si atom in a Si=Si dimer (cf. section 5.3.2). Thus, the coexistence of the different bindings of pyridine on Si(100) may be possible. Although the principle reaction types of the different molecules are understood quite well, a more detailed experimental observation of the adsorption geometry and chemical bonding is missing for most of the molecules. This information is important for continuing experiments in these systems [77].

Several experimental and theoretical studies including STM, AES, NEXAFS, and TDS [61, 87–89] as well as DFT calculations [81] have been performed in this system, but the structure at the interface is still heavily discussed. The different possible adsorption pathways are leading to twelve different possible structures for the molecule on the Si(100) surface [61, 89]. Depending on different kinds of preparation techniques three main kind of structures have been found for studies at room temperature. Witkowski et al. proposes a 1,4,5,6-tetra-σ-bonded structure (Fig. 5.21 Mode VII) from their fully resolved polarization near-edge x-ray adsorption fine-structure spectroscopy studies [89]. In a combined study of thermal desorption spectroscopy (TDS), x-ray photoelectron spectroscopy (XPS), high-resolution electron energy loss spectroscopy (HREELS), and DFT theoretical calculations Xu et al. determined that a standard butterfly structure with a Si-C and Si-N bonding is the structure (Fig. 5.21 Mode IV) after the adsorption. Leung et al. assumed that pyridine is adsorbed in three adsorption modes (Fig. 5.21 mode IV, V, XII) due to the behavior in their thermal desorption spectrometry experiments [88]. DFT calculations by Cho et al. [81] and STM measurements by Lopinski et al. [87] predict an adsorption in mode VIII and claim the mode VII to be less stable. The different results for the adsorption states using different analysis techniques leads to the conclusion that more fundamental studies need to be done to finally solve the real structure.

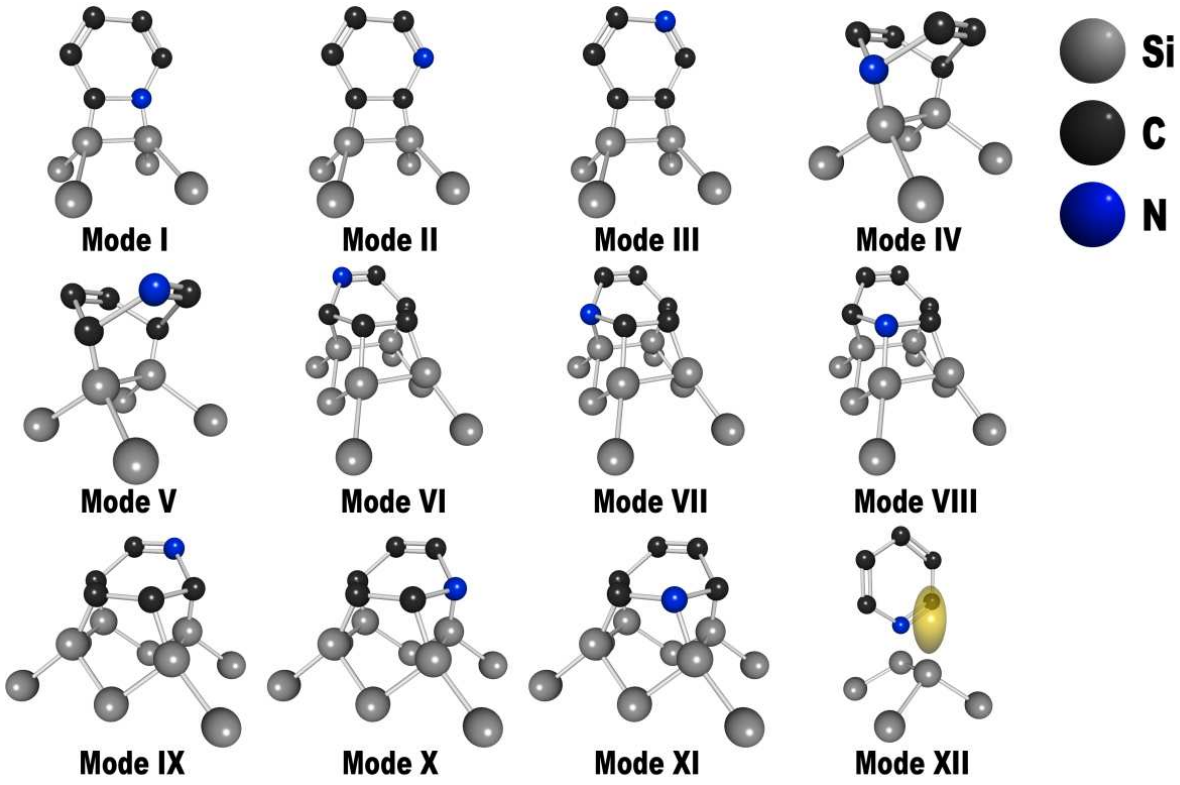

Figure 5.21: Schematic drawing of possible adsorption geometries of pyridine on Si(100) [89]

The analysis of the Si 2p XPS signal and analysis of the C 1s signal provides information about the chemically shifted components in the system, the remaining density of silicon dimers, and the vibrational states of the carbon atoms. The comparison of experimental XPD patterns with simulations for various possible (cf. Fig.5.21) models allows a detailed picture of the local structure. This study allowed us to achieve experimental results and isolate one adsorption geometry of this system, including atomic distances and tilting angles between the different layers. These parameters allows us to draw a coherent picture of this system including adsorption sites and structural parameters.

5.5.1 XPS Analysis

The in-situ preparation procedure was started by degassing sample and sample holder at approximately 700°C for 6 hours. Afterwards the sample was flash heated at 1050°C in order to remove the native SiO_2 and cooled down slowly to prepare a (2x1)-reconstructed silicon surface. During the procedure the pressure was kept below $5 \cdot 10^{-10}$ mbar. The surface reconstruction and the absence of any impurities were checked by LEED, XPS,

and XPD, respectively(cf. section 5.2). The sample was exposed to $1 \cdot 10^{-6}$ mbar partial pressure of pyridine for 5 minutes at room temperature which is an efficient pressure to achieve a saturation coverage [88]. Additionally exposition of the samples to pyridine didn't change the relative C1s-Si2p intensity which leads to the conclusion that a saturation coverage was achieved. Between the preparation procedure and the measurements of the XPS signals the system was left untouched for about six hours to allow the system to reach its energy minimizing state. Fig. 5.22 shows a survey spectra of the sample after the preparation procedure was finished. The N 1s and C 1s signals resulting from the molecule adsorption are clearly visible.

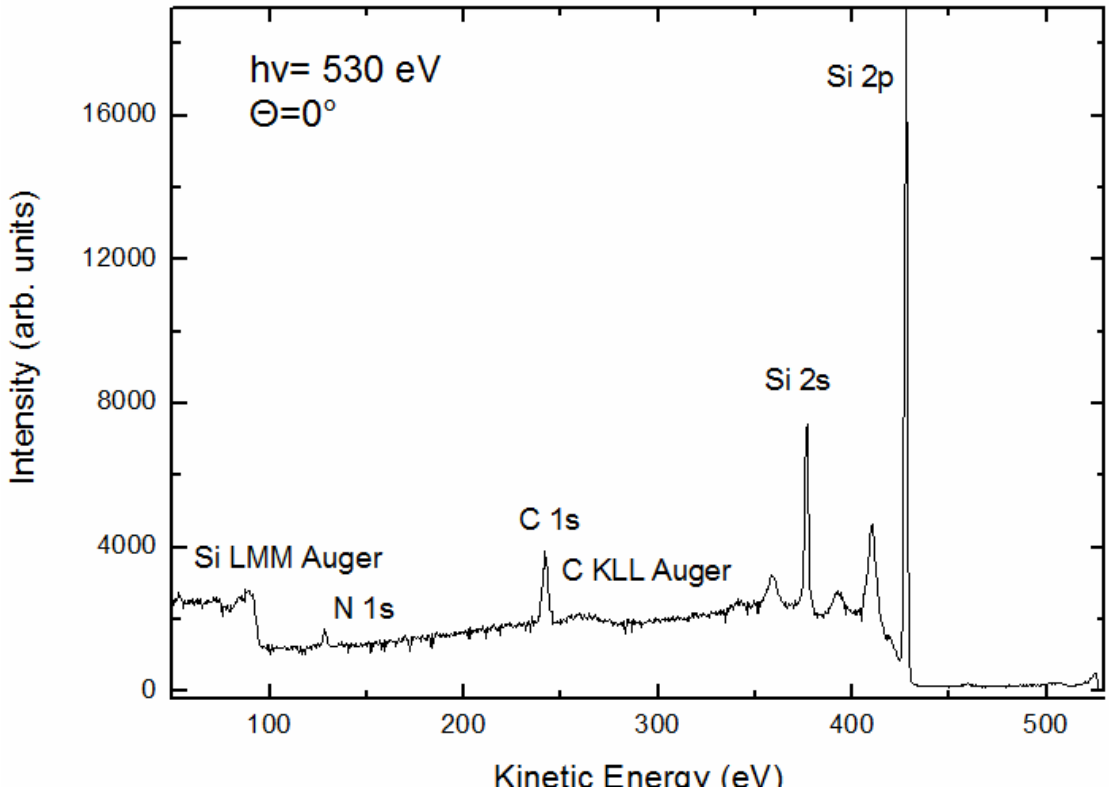

Figure 5.22: Survey spectra after the preparation was finished

The twelve different structures shown in Fig. 5.21 feature different bonding types (Si-C, Si-N) between the silicon substrate and the absorbed molecules. Therefore a careful analysis of the line shape of the Si 2p line could help to exclude some of the structures. A helpful procedure for analyzing the XPS spectra is the comparison to adsorbed molecules on the silicon surface that contain only carbon atoms. In these systems, only carbon silicon bonds are possible and therefore only one additional component is seen in the spectrum. One example of this systems is cyclopentene on silicon(100) [90]. Fig 5.23

shows the line shapes of clean silicon (a), cyclopentene on silicon (b), and pyridine on silicon (c).

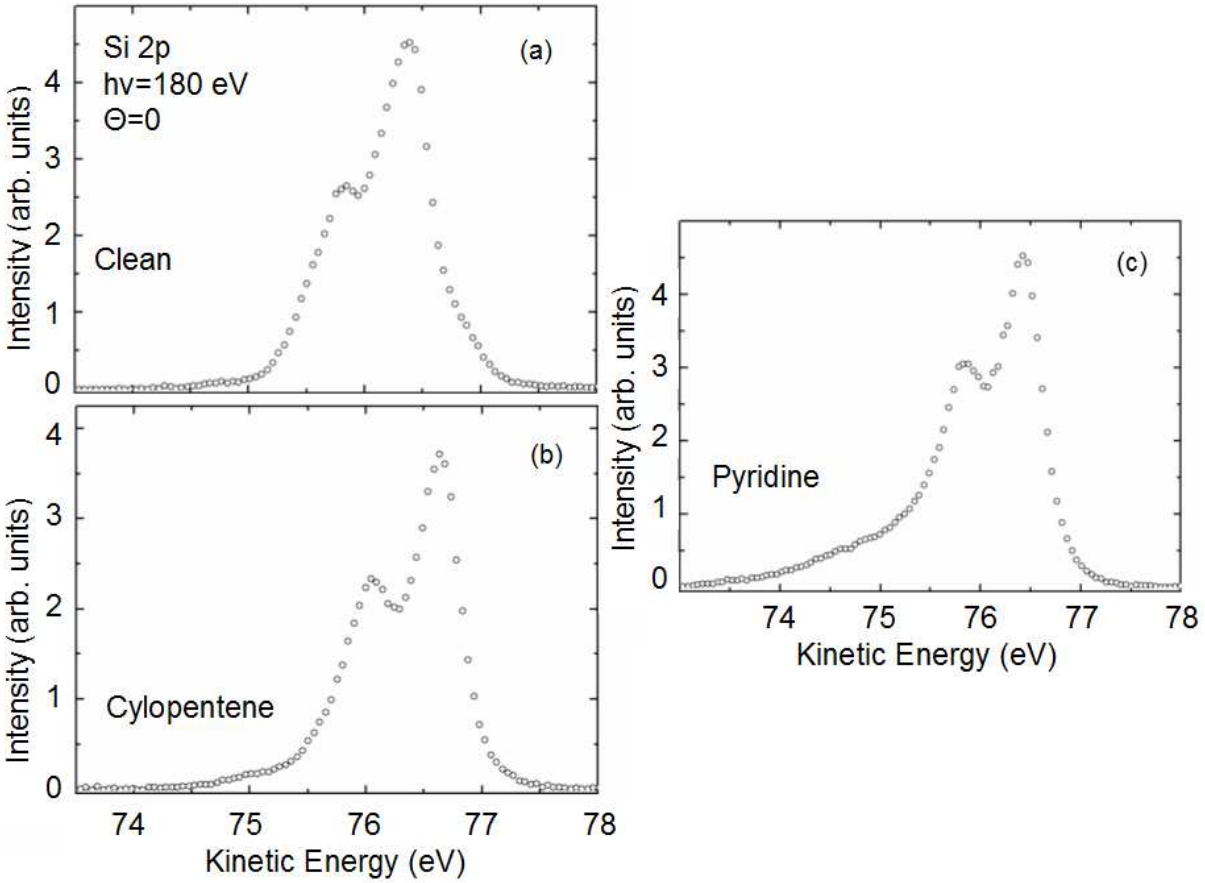

Figure 5.23: Silicon 2p photoelectron signals recorded with a photon energy of $h\nu$=180 eV and at normal emission. The spectra were taken for the clean surface (a), cyclopentene/Si(100) (b), and pyridine/Si(100) (c).

In the comparison to the clean silicon (a) and cyclopentene+silicon (b), only additional carbon silicon bonds can be expected, because the cyclopentene molecule only contains carbon atoms. The new silicon-carbon bonds results in an additional component in the XPS signal, which is clearly visible in the line shape of the spectra. If one of the structures from Fig. 5.21 containing only Si-C bonds (II, III, V, VI, IX) is the final adsorption structure of the system, the silicon 2p line shape of pyridine should look like the silicon 2p signal of the cyclopentene+silicon system. However the comparison of the line shape of Fig. 5.23 (b) and Fig. 5.23 (c) shows a clearly visible difference. Therefore, at least one additional component is included in the signal. The silicon 2p peak for the clean (2x1)-reconstructed surface consists of three doublets with a spin orbit splitting of 0.6 eV and an intensity ratio of 2:1 as known from the literature [82, 83]. The three components

are attributed to the bulk, upper dimer atom and lower dimer atom + sub surface, respectively [82, 83]. In the case of cyclopentene adsorption on the silicon(100) surface, one additional component arises, which is shifted by ΔE=+0.78 eV to higher binding energies whereas the components belonging to the dimers decreases drastically [90]. For the adsorption of pyridine on silicon, a decomposition of five components is necessary to improve the residuum of the least squares fit. The best fits obtained for the clean surface and for the pyridine+silicon system are presented in Fig. 5.24(a)+(b). The five components are named B, S, S', Si-C, and Si-N, which are attributed to the bulk, upper dimer atom, lower dimer atom + sub surface, silicon-carbon bond, and the silicon-nitrogen bonds, respectively. During the fitting procedure, the binding energy separation within a doublet was set to 0.60 eV. Within a doublet, the intensity ratio of the Si $2p_{3/2}$:Si$2p_{1/2}$ component was set to 2:1. The relative binding energy shifts for the different doublets are presented in Table 5.4.

Silicon	B	S	S'	Si-C	Si-N
Relative Shift (eV) 0°	0.0	-0.45	0.30		
Silicon+Pyridine					
relative shift (eV) 0°	0.0	-0.45	0.30	0.78	1.58

Table 5.4: Fitting parameters for the spectra shown in Fig. 5.24. Energy shifts for the different components are given with respect to the bulk component.

The observed relative energy shifts with respect to the bulk signal are 0 eV, -0.45 eV, 0.30 eV, 0.78 eV, and 1.58 eV for the (B), (S), (S'), (Si-C), and (Si-N) components, respectively. The existence of two additional components leads to the conclusion that the adsorption geometry of the molecule must contain silicon-carbon bonds, as well as silicon-nitrogen bonds. Therefore, we can exclude the exclusive existence of the modes II, III, V, VI, IX due to the existence of Si-N bonds and the mode XII due to the existence of Si-C bonds. The intensity ratio of approximately 3:1 between the component Si-C and Si-N yields additional information. Corresponding to this information, the number of silicon-carbon bonds exists three times as often as silicon-nitrogen bonds. This intensity ratio favors the tetra-σ-bonded structures in Fig. 5.21 (VII, VIII, X, XI) where these kind of bindings are visible. A comparison of the component S, which belongs to the upper dimer atom of the silicon, shows that the signal is decreasing after the adsorption of pyridine. However, the component is still visible after the adsorption. This leads to the conclusion that some dimers remain intact and that the saturation coverage pyridine on silicon(100) did not cover all atoms of the surface. These findings are in very good agreement with the XPD results shown in the next chapter.

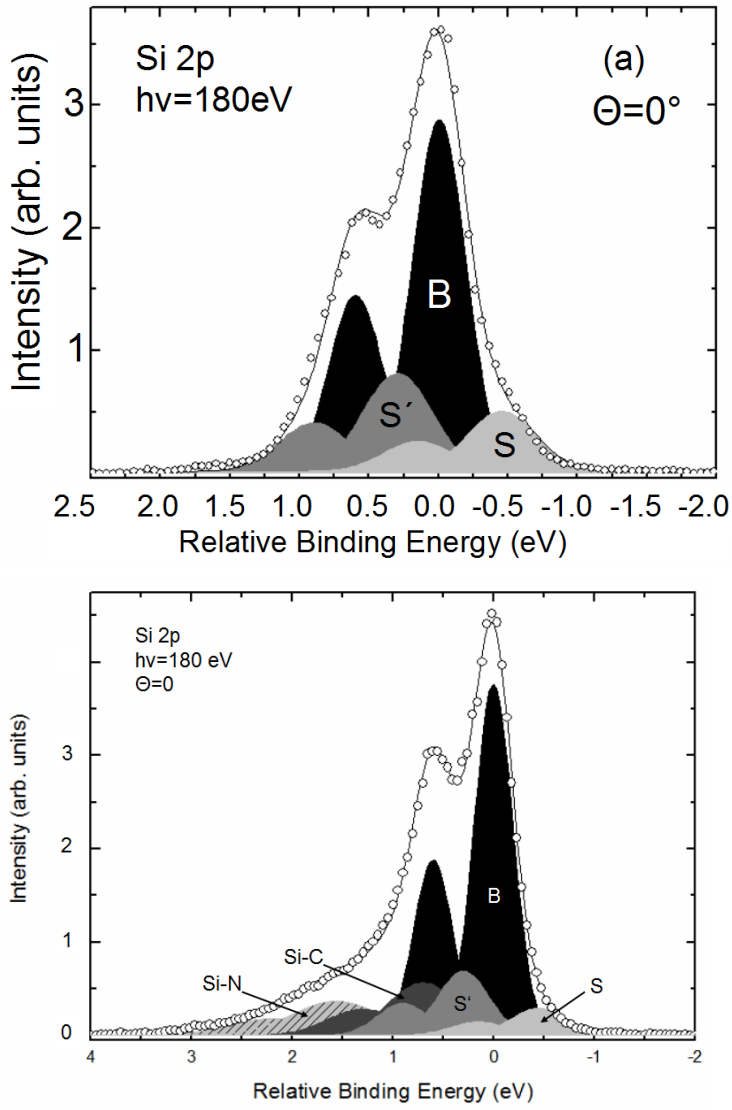

Figure 5.24: Results of the least squares fit of the spectra of clean Si(100) (a) and pyridine/Si(100) (b). The fitting components are discussed in the text. Fitting parameters are presented in Tab.5.4

Fig 5.25 shows high resolution spectra of the C 1s spectra after the adsorption of pyridine. The line shape of the spectrum indicates at least three components in the spectrum with a shoulder at higher and at lower binding energies to the main peak. In the analysis of the C 1s signal of unsaturated hydrocarbons vibrational splittings resulting from the C-H molecular bonds have to be included. This effect was shown both for gaseous [16–19] and adsorbed molecules [20, 21]. An accepted theory explaining this effect in XPS spectra is the application of a linear coupling model with a Frank-Condon process [20] as the excitation process. A detailed description of the line shape

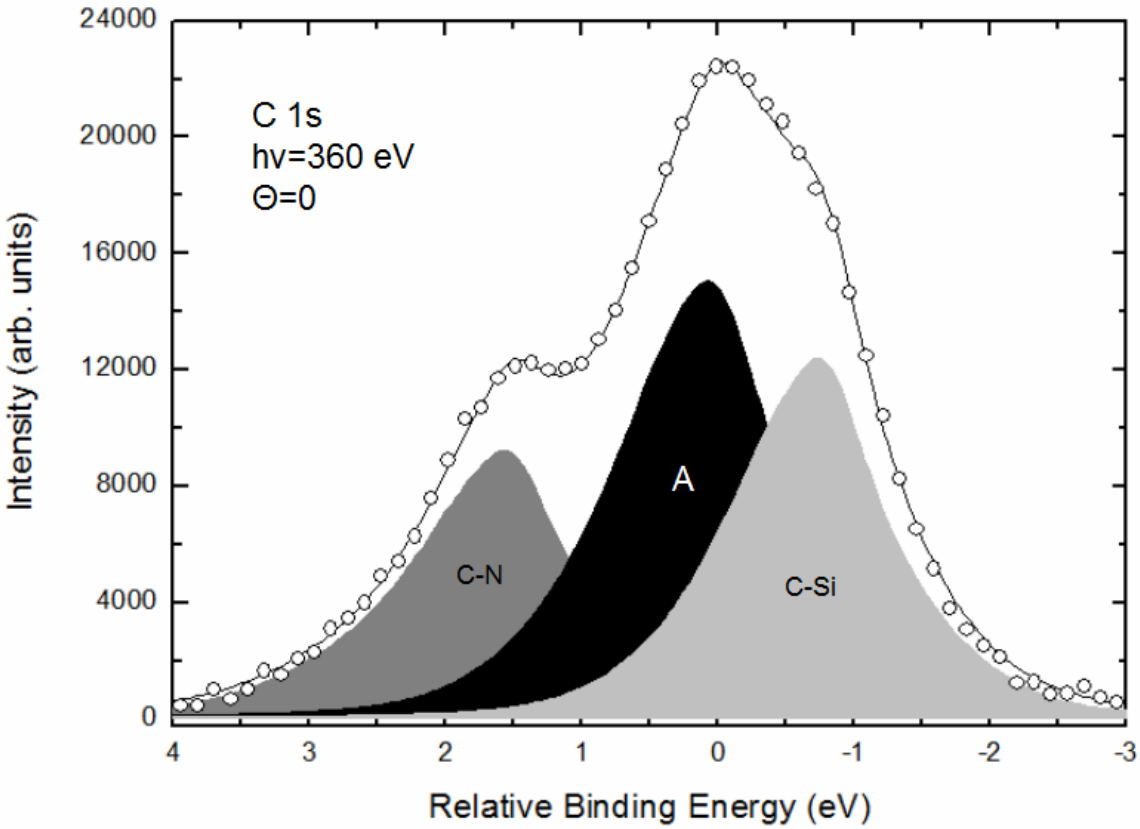

Figure 5.25: Carbon 1s photoelectron signals recorded at a photon energy of $h\nu$=360 eV at normal emission. The fitting components are denoted in Tab. 5.5 and in the text.

profiles can be found in section 2.2.2. Within the linear coupling approximation the C 1s line is divided into three different chemical components. The component C-N, C-Si, A are assigned to C-N, C-Si and C=C+Si-C-N bonds, respectively. The parameters used for the fitting procedure are displayed in Tab. 5.5.

Within the fitting procedure over 4000 individual spectra which had been recorded within this photoelectron diffraction pattern were evaluated. The diffraction pattern were recorded for an azimuthal and polar range of 0° to 358° and 30° to 76°, respectively. The step-width of 2° was kept constant for both angular settings. Results from our fitting procedure agree well with previous studies for C-H stretching modes [16–21]. The component C-Si belongs to the carbon atoms C(1) and C(3) in Fig. 5.27(a), which have single bonds to carbon and single bonds to silicon. Atom C(5) is corresponding to the component C-N, where the carbon has a double bond with a carbon atom and a single bond to the nitrogen. Finally the component A belongs to the atoms C(2) and C(4).

	Relative Shift (eV)	ΔE (eV)	S	W_G (eV)	W_L (eV)
A	0.00	0.45	0.40	0.30	0.16
C-Si	-0.63	0.45	0.42	0.30	0.16
C-N	1.50	0.45	0.42	0.30	0.16

Table 5.5: Fitting parameters for the spectra shown in Fig. 5.25. The relative energy shift is given with respect to the component A's position. The parameters W_G and W_L are the FWHM of the Gaussian- and Lorentzian part of the Voigt profile. The parameters ΔE and S resulting from vibrational effects [20] are discussed in the text.

These atoms features different bonding neighbors, but their the relative binding energy position of these carbon atoms is the same. The atom C(2) is shifted to higher binding energies by its nitrogen neighbor, but shifted to lower binding energies by its silicon neighbor. Due to the stronger chemical shift by the nitrogen, this results in a small shift to higher binding energies. The atom C(5) is shifted to a higher binding energy because of the C=C double bond. This effect of double bonds in comparison to single bonds is well known. These two resulting components could not be clearly separated within the energy resolution. Therefore, for our XPD analysis, theses two atoms are combined in one component.

5.5.2 XPD Analysis

Figure 5.26 shows the experimental and simulated photoelectron diffraction patterns of the C-N, A, and C-Si component discussed above, respectively. The diffraction pattern is a plot of the anisotropy function $\chi = [I(\Theta, \Phi) - I_0(\Theta)]/I_0(\Theta)$ [8], where $I(\Theta, \Phi)$ and $I_0(\Theta)$ denote the intensity at the emission direction (Θ, Φ) and the average intensity at emission direction (Θ), respectively. Its percentage is displayed in the lower left corner of the pattern. A detailed description of the XPD procedure and plotting details is also given in sections 2.3 and 3.1.

The experimental patterns presented in Figure 5.26(a) clearly show strong diffraction effects, with a max. anisotropy of 21%, 18% and 19%, respectively. In order to obtain structural information from the experimental photoelectron diffraction patterns, simulations were performed using varying starting structures following the structures shown in Fig. 5.21. In order to compare the experimental data with the simulated data an R-factor analysis [84] was introduced as an analytical measure. The R-factor is defined as

$R = \sum_i \frac{(\chi_{th}-\chi_{exp})^2}{\chi_{th}^2+\chi_{exp}^2}$, where χ_{exp} and χ_{th} denote the experimental and simulated diffraction patterns, respectively. In the simulations, many different structure models were tested and a certain number of parameters were varied, including bond length between the atoms and tilt angles between the bonding directions.

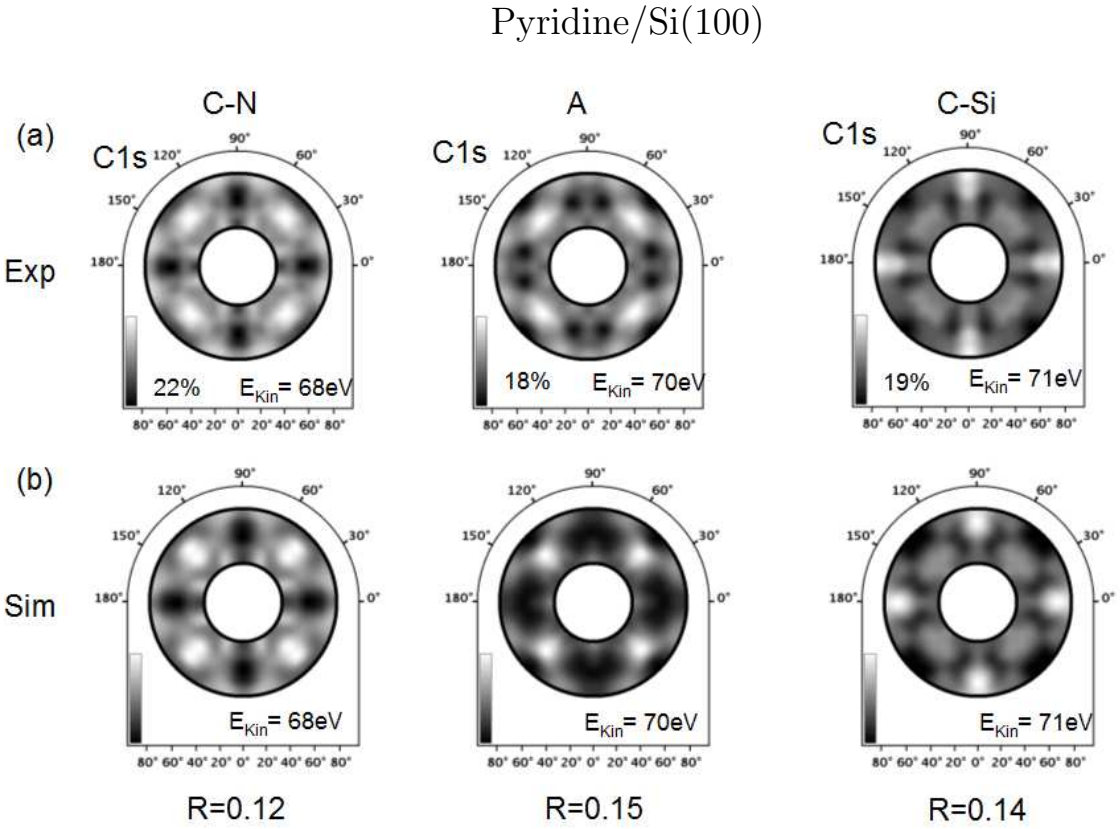

Figure 5.26: Experimental photoelectron diffraction pattern for the C-Si, C-N, and A signals discussed in Tab 5.5 (a). Simulated pattern obtained for the structural parameters with the lowest R-factor (b).

In Figure 5.26(b) the best simulated patterns with the lowest R-factors for each pattern are displayed. These patterns with a minimized R-factor were obtained by the genetic algorithm for various starting parameters of the simulation. All maxima and minima as displayed in the experimental pattern are clearly contained in the simulated pattern. In addition, R-factors of R=0.12, R=0.15 and R=0.14 support the excellent agreement between experimental and simulated pattern. Each pattern was simulated independently, but the best R-factor for each pattern is obtained with the same structure model. The structural parameters within the model obtained from the three independent simulations were averaged to achieve the best information. The structural parameters obtained can be found in Tab. 5.6.

	this work
$d_{Si(1)-Si(2)}$ (Å)	1.88 (0.04)
$d_{Si(3)-Si(4)}$ (Å)	2.34 (0.08)
$d_{Si(1,2)-C(1,2)}$ (Å)	1.95 (0.04)
$d_{Si(3)-C(3)}$ (Å)	1.91 (0.04)
$d_{Si(4)-N}$ (Å)	1.91 (0.04)
$d_{C(1)-C(3)}$ (Å)	1.63 (0.04)
$d_{C(2)-N}$ (Å)	1.57 (0.04)
$d_{C(3)-C(4)}$ (Å)	1.58 (0.04)
$d_{N-C(5)}$ (Å)	1.58 (0.04)
$d_{C(4)=C(5)}$ (Å)	1.36 (0.03)
Φ_1 [°]	52.0 (5.0)
Φ_2 [°]	72.0 (8.0)
Φ_3 [°]	41.0 (5.0)
Φ_4 [°]	26.0 (3.0)

Table 5.6: R-factor minimizing distances of the absorbed molecule and the relaxed dimers. The estimated errors are obtained within the 10% R-factor criterion [21] for each structure and the averaging of these.

All the atomic assignments used in Tab. 5.6 can be seen in Fig 5.27(a). The resulting structure model is shown in Fig. 5.27, with a a three-dimensional structure model of the adsorbed pyridine molecule on the Si(100) surface (a), the top view of the structure (b), side view along the (010)-axis (c), and the side view along the (001)-axis (d), respectively. In Fig. 5.27(e) the angles Φ_1 to Φ_4 are also presented. The adsorption structure of the molecule is found to be Mode VII from Fig 5.21, which is a tetra-σ-bonded structure. The underlying silicon dimers serve as the adsorption sites for the atoms C(1), C(2), C(3), and N. The dimer which is attached to the two carbon atoms C(1) and C(2) is approached to each other with a distance of 1.88 Å in comparison to the standard dimer distance. However, the distance of the silicon dimer attached to the atoms C(3) and N is broadened with a distance of 2.34 Å in comparison to the standard distance. The atomic distances between the substrate and the adsorbed molecule is around 1.9 Å which is in good agreement with distance observed for other hydrocarbons on silicon(100) substrates [21, 90]. The atomic distances inside the molecule are in good agreement with the atomic distance for free hydrocarbons [86]. This means the bindings inside the molecule are all single bonded, except the bond between C(4) and C(5). The bond length between these two atoms is much shorter, and is a result of a localized carbon double bond at

this position. In Fig. 5.27(e), it is clearly visible that the molecule loses the planar geometry observed for a free molecule. The atoms C(3) and N are bent slightly upwards in comparison to the atoms C(1) and C(2). The atoms C(4) and C(5) are strongly bent upwards in comparison to the C(3) and N atom.

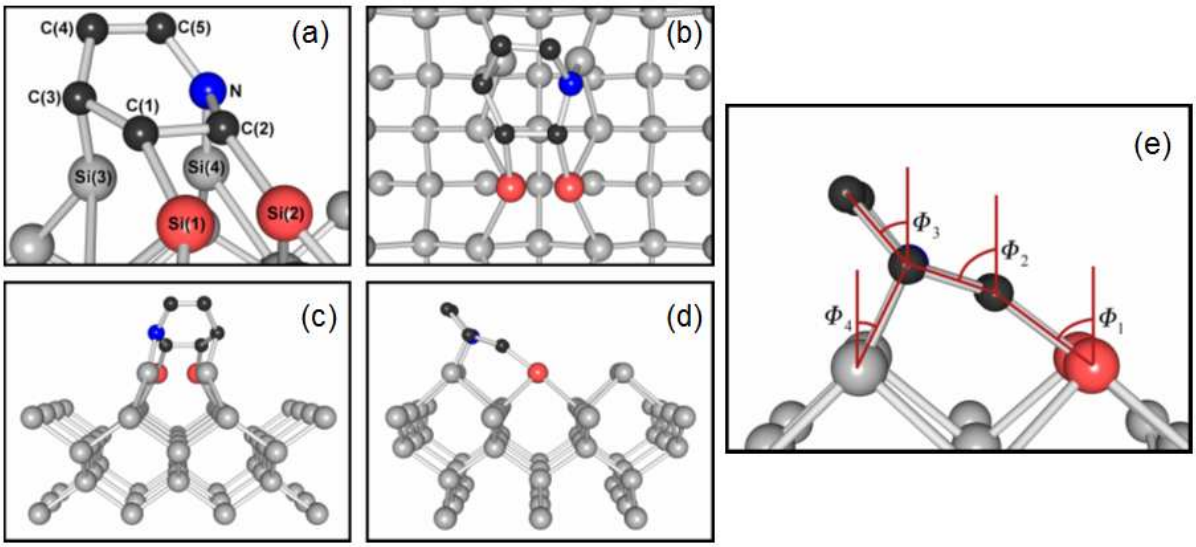

Figure 5.27: Structure model obtained within the R-factor minimization. Hydrogen atoms are not included.

Our best structure model is also in line with our high resolution XPS analysis of the silicon 2p line (cf.. Fig. 5.24) where we observed silicon-nitrogen and silicon-carbon bonds. From the whole analysis of our data, we find that the adsorption geometry for pyridine on silicon is given by mode VII. Additionally, our R-factor analysis shows that only two out of three silicon dimers are coated directly with the molecule which can be seen in Fig. 5.27(d). This indicates that intermolecular reactions near the saturation coverage disfavors the use of each dimer. The amount of molecules at the surface might be the one of the most important parameters for the final adsorption structure. Comparing our results to results obtained before for this system suggests this should be taken into account. The results by Witkowski et al [89] at a saturation coverage favor the mode VII, but they also report some minor species of other adsorption sides. Our R-factor analysis for adding other species, however, always worsens the R-factor. Therefore, we conclude that if there are other modes than mode VII they should be much less prevalent than the mode VII. The STM studies done by Lopinski et al. [87], which favors mode VIII, focus

on selective adsorption sides of pyridine on silicon, which means their studies did not deal with molecular interaction at all. Also, the DFT studies by Cho et al. [91] favors mode VIII at low coverage. However, they point out that if some of the adsorption energy of the initial adsorption state remains undissipated, a transition to the final state of mode VII is possible [91]. As they also studied low coverage of pyridine, a molecular interaction at higher coverages could lead to this result.

5.5.3 Conclusion on Pyridine on Silicon

In conclusion, we have studied the adsorption site of pyridine on a double-domain silicon(100) surface by means of XPS and XPD. The adsorption of the molecule is mediated by a reaction to silicon dimer atoms. In the XPS spectrum of the Si 2p signal, two additional components appeared after the adsorption belonging to Si-C and Si-N bonds. An analysis of the carbon 1s core level spectra was carried out in the linear coupling model with asymmetric line shape parameters in the fitting procedure. The line shape confirmed established parameters for the C-H stretching mode and the existence of three chemically different components, which belong to four different bonding configurations. Within the XPD-analysis, results obtained from model structures were compared to the experimental diffraction pattern. The XPD-analysis included an automated search for the model structure, including a genetic algorithm for the structure search and an R-factor analysis. From these results, we propose an adsorption structure of pyridine on Si(100) in a 1,4,5,6-tetra-σ-bonded structure.

6 Conclusion and Outlook

The results presented within this thesis were the first interface investigation at hybrid devices using XPD in synchrotron light. The studied system included hydrocarbon molecules as well as cyclic molecules with functionalized atoms. In particular the systems cyclopentene on Si(100) and pyridine on Si(100) were investigate regarding their structure, interface properties and adsorptions sides. A complete structure model for both of the systems was given including atomic distances and tilting angles regarding the different layers.

At the beginning of the investigations the challenge of radiation damage in soft matter experiments was examined. For this reason the system of ethanthiol on Au(111) was investigated. This system is well known for its susceptibility to radiation damage in the focus point of undulator beamlines. The amount of radiation damage could be lowered drastically by reducing the amount of photons per area unit. This was achieved by positioning the sample 0,5 m behind the focus point of the beamline. At this position the beamsize is broadened to approx. 1 x 0.8 mm^2 in comparison to 70 x 30 μm^2 within the focus of the beamline. Using this setup it was possible to reduce the number of photons per area unit by a factor of approx. 400 without losing overall count rate. This results in much less radiation damage to the molecules and therefore allowed stable experimentel conditions for the following investigations.

The new experimental setup was applied for all following investigations and allowed us to study the system cyclopentene on Si(100). Firstly the system was investigated by means of XPS and the saturation coverage and the degradation of the dimers at the substrate were examined. About $\sim$75% of the silicon dimers were destroyed during the adsorption process (cf. Chap. 5.4.1). In the ongoing XPD studies we were able to record a diffraction pattern of the C 1s peak of the system. The characteristic behaviour of this system in the C 1s peak due to C-H stretching modes was carefully considered(cf. Chap. 5.4.1). The experimentel diffraction pattern was compared to simulated patterns of various cluster models. Within the clusters models the experimentel and simulated patterns were compared within a comprehensive R-factor analysis. The minimization

of the R-factor was achieved by genetic algorithm routines (cf. Chap. 3.2). The final structure model results in an upright standing molecule with various tilting angles between the different layers (cf. Chap. 5.4.2). This was the first time this structure could be observed, because other methods like STM could only access the uppermost layer.

For the following experiments the adsorbed molecule was changed from an hydrocarbon molecule to a cyclic molecule with a functionalized atom. In our study pyridine was chosen which is a benzene-like molecule in which one carbon atom is replaced by a nitrogen atom. Previous investigations showed twelve different structures which were discussed as possible candidates in literature. Within our analysis we could exclude eleven of these structure models and solve the real structure of the system. Firstly our XPS results of the Si 2p signal, in combination with the XPS results obtained from the system cyclopentene on Si(100), allowed us to exclude six of the suggested structures (cf. Chap. 5.5.1). Within the following XPD analysis we were able to separate the C 1s signal into 3 chemically different components. For the fitting procedure the C-H stretching modes were again carefully considered. We were able to achieve a diffraction pattern for each of the three components in the C 1s signal. Simulations of diffraction patterns were performed for all six remaining structures including each experimental pattern. Finally only one structure model was found to minimize the R-factor for all three diffraction patterns (cf. Chap. 5.5.2) at the same time. The adsorption structure was found to be a 1,4,5,6-tetra-σ-bonded structure which is mode VII in Fig. 5.21. Furthermore the atomic distances and tilt angles were obtained within the analysis.

The results presented within this work showed that it is possible to investigate the structure of hybrid devices by means of photoelectron spectroscopy and photoelectron diffraction. The examined systems formed well ordered films, but with strong differing adsorption geometries. However, it was possible to solve both of the adsorption and interface structures with our analytic methods. This fundamental investigations regarding XPD studies at hybrid devices showed that it will be possible to study more complex hybrid devices systems with XPD in the future.

Possible candidates for investigations in this regime can be found easily, because as mentioned in the beginning 95% of all chemical components belong to the organic regime. Therefore interesting single layer systems on Si(100) will be attracting much interest in the future. However, the method of XPD is not limited to single layer systems. Multi-layer organic films on semiconductor surfaces gain more and more attention. Within the multi-layer systems the structure of the uppermost molecule can be seen by real space

imaging. However, the structure between the different molecular layers and the lowermost molecule and the substrate cannot be accessed. At present, these burried interfaces may only be accesses by diffraction methods. In addition a possible change of the atomic geometry in the interface region due to further molecular layers may be observed.

A further interesting area of research includes molecular reaction at surfaces. For example the molecules of Furan (C_4H_4O) and Pyrrol (C_4H_4N) can be adsorbed to the silicon surface. In chemical catalysis it is known that a transfer from Furan to Pyrrol is easily possible by providing Ammonia (NH_3) to the system. An interesting question is weather it is possible to adsorb Furan to the surface and than achieve a switching to Pyrrol by providing Ammonia. If it is possible it will be very interesting to examine the adsorption and interface structure of "changed-pyrrol" compared to directly adsorbed Pyrrol. This kind of reaction would provide accessibility to molecular switches on surfaces by just using well known chemical reactions.

Bibliography

[1] S. Bent, Surf. Sci. **500**, 879 (2002).

[2] Semiconductor Industry Association, *International Technology Roadmap for Semiconductors*, 1999.

[3] W. Wang, A. Scott, N. Gergel-Hackett, C. Hacker, D. Janes, and C. Richter, ACS Nano Letters **8**, 478 (2008).

[4] N. Gergel-Hackett and C. Richter, J. Am. Chem. Soc. **130**, 4259 (2008).

[5] J. Hill and D. Kolb, *Chemistry for Changing Times* (Englewood Cliffs NJ, 1995).

[6] C. Fadley, *Synchrotron Radiation Research: Advances in Surface Science* (Plenum Press New York, 1992).

[7] D. Woodruff and A. Bradshaw, Rep. Prog. Phys. **57**, 1029 (1994).

[8] C. Westphal, Surface Science Reports **50**, 1 (2003).

[9] R. Gunnella, F. Solal, D. Sebilleau, and C. Natoli, Comput. Phys. Commun. **132**, 251 (2000).

[10] H. Hertz, Ann. Physik u. Chemie **31**, 983 (1887).

[11] A. Einstein, Ann. Physik (Leipzig) **17**, 132 (1905).

[12] M. Henzler and W. Goepel, *Oberflächenphysik des Festkörpers* (Teubner, 1991).

[13] P. Auger, C.R. Acad Sci. **177**, 169 (1923).

[14] D. Briggs and M. Seah, *Practical Surface Analysis by Auger and X-Ray Photoelectron Spectroscopy* (Sohan Wiley & Sons, 1985).

[15] S. Hüfner, *Photoelectron Spectroscopy* (Vieweg, 1992).

[16] S. Osborne, S. Sundin, A. Ausmees, S. Svensson, L. Saethre, O. Svaeren, S. Sorensen, J. Vegh, J. Karvonen, S. Aksela, and A. Kikas, J. Chem. Phys. **106**, 1661 (1997).

[17] H. Köppe, A. Kilcyne, J. Feldhaus, and A. Bradshaw, J. Electron Spectrosc. Relat. Phenom. **75**, 97 (1995).

[18] B. Kempgens, A. Kivimaki, B. Itchkawitz, H. Koppe, M. Schmidbauer, M. Neeb, K. Maier, J. Feldhaus, and A. Bradshaw, J. Electron Spectrosc. Relat. Phenom. **93**, 39 (1998).

[19] S. Sorensen, M. Wiklund, S. Sundin, A. Ausmees, A. Kikas, and S. Svensson, Phys. Rev. A **58**, 1897 (1998).

[20] Y. Yamashita, S. Machida, M. Nagao, S. Yamamoto, K. Mukai, and J. Yoshinobu, Chem. Phys. Lett. **374**, 476 (2003).

[21] R. Gunnella, M. Shimomura, F. D'Amico, T. Abukawa, and S. Kono, Phys. Rev. B **73**, 235435 (2006).

[22] K. Siegbahn, U. Gelius, H. Siegbahn, and E. Olson, Physics Letters A **32**.

[23] A. Liebsch, Phys. Rev. Lett. **32**, 1203 (1974).

[24] M. Seah and W. Dench, Surf. and Interface Anal. **1**, 2 (1979).

[25] F. Salvat and R. Mayol, Comput. Phys. Commun. **74**, 358 (1993).

[26] I. Langmuir, J. Am. Chem. **38**, 2221 (1916).

[27] Wutz, Adam, and Walcher, *Theorie und Praxis der Vakuumtechnik* (Vieweg, 1992).

[28] VG company, *CLAM 4 MCD Analyser System Operating Manual* (VG, 1996).

[29] J. Pendry, *Low Energy Electron Diffraction* (Academic (London), 1974).

[30] U. Berges, M. Krause, M. Schürmann, S. Dreiner, R. Follath, F. Schäfers, and C. Westphal, Synchrotron Radiation Instrumentation: Eight International Conference **1**, 424 (2004).

[31] K. Heister, M. Zharnikov, M. Grunze, L. Johanson, and A. Ulman, Langmuir **17**, 8 (2001).

[32] P. Feulner, T. Niedermayer, K. Eberle, R. Schneider, D. Menzel, A. Baumer, E. Schmich, A. Shaporenko, Y. Tai, and M. Zharnikov, Phys. Rev. Lett. **93**, 178302 (2004).

[33] A. Ulman, Chem. Rev. **96**, 1533 (1996).

[34] D. Chadi, Phys. Rev. Lett. **43**, 43 (1979).

[35] R. Tromp, R. Smeenk, F. Saris, and D. Chadi, Surf. Sci. **137**, 137 (1983).

[36] M. Aono, Y. Hou, C. Oshima, and Y. Ishizawa, Phys. Rev. Lett. **49**, 567 (1982).

[37] I. Stensgaard, L. Feldmann, and P. Silverman, Surf. Sci. **102**, 1 (1981).

[38] R. Tromp, R. Smeenk, and F. Saris, Phys. Rev. Lett. **46**, 9392 (1981).

[39] N. Jedrecy, M. Sauvage-Simkin, R. Pinchaux, J. Massis, N. Greiser, and V. Etgens, Surf. Sci. **230**, 197 (1990).

[40] G. Jayaram, P. Xu, and L. Marks, Phys. Rev. Lett. **71**, 3489 (1993).

[41] R. Tromp, R. Hamers, and J. Demuth, Phys. Rev. Lett. **55**, 1303 (1985).

[42] R. Hamers, R. Tromp, and J. Demuth, Phys. Rev. B **34**, 5343 (1986).

[43] R. Wolkow, Phys. Rev. Lett. **68**, 2636 (1992).

[44] N. Roberts and R. Needs, Surf. Sci. **236**, 112 (1990).

[45] J. Dabrowski and M. Scheffler, Appl. Surf. Sci. **56**, 15 (1992).

[46] P. Krüger and J. Pollmann, Phys. Rev. B **38**, 10578 (1988).

[47] P. Krüger and J. Pollmann, Phys. Rev. B **47**, 1889 (1993).

[48] J. Northrup, Phys. Rev. B **47**, 10032 (1993).

[49] A. Ramstad, G. Brocks, and P. Kelly, Phys. Rev. B **51**, 14504 (1995).

[50] E. Landemark, C. Karlsson, Y. Chao, and R. Uhrberg, Phys. Rev. Lett. **69**, 2757 (1990).

[51] D. Weier and C. Flüchter and A. de Siervo and M. Schürmann and S. Dreiner and U.Berges and M.F. Carazzolle and A. Pancotti and R. Landers and G.G. Kleiman and C. Westphal, Mater. Sci. Semicond. Process. **9**, 1055 (2006).

[52] A. Wassermann, *Diels-Alder Reactions: Organic Background and Physio-Chemical Reactions* (Elsevier, New York, 1965).

[53] G. Gill and R. Gillis, *Pericyclic Reactions* (Chapman and Hall, London, 1974).

[54] W. Carruthers, *Cycloaddtion Reactions in Organic Synthesis* (Pergram Press, New York, 1990).

[55] R. Woodward and R. Hoffmann, Angew. Chem. **81**, 797 (1969).

[56] H. Liu and R. Hamers, J. Am. Chem. Soc. **119**, 7593 (1997).

[57] A. Mayne, A. Avery, J. Knall, T. Jones, G. Briggs, and W. Weinberg, Surf. Sci. **284**, 247 (1993).

[58] C. Huang, W. Widdra, and W. Weinberg, Surf. Sci. **315**, 953 (1994).

[59] L. Clemen, R. Wallace, P. Taylor, M. Desser, W. Choyke, W. Weinberg, and J. Y. Jr., Surf. Sci. **268**, 205 (1992).

[60] W. Widdra, C. Huang, S. Yi, and W. Weinberg, J. Chem. Phys. **105**, 5605 (1996).

[61] S. Xu, M. Keeffe, Y. Yang, C. Chen, M. Yu, G. Lapeye, E. Rotenberg, J. Denlinger, and J. Y. Jr., Phys. Rev. Lett. **84**, 939 (2000).

[62] D. Sorescu and K. Jordan, J. Phys. Chem. B **104**, 8259 (2000).

[63] B. Craig and P. Smith, Surf. Sci. **276**, 174 (1992).

[64] A. Fisher, P. Blöchel, and G. Briggs, Surf. Sci. **374**, 298 (1997).

[65] B. Meng, D. Maroudos, and W. Weinberg, Chem. Phys. Lett. **278**, 97 (1997).

[66] R. Wolkov, Annu. Rev. Phys. Chem. **50**, 413 (1999).

[67] Q. Liu and R. Hoffmann, J. Am. Chem. Soc. **117**, 4082 (1995).

[68] G. Lopinski, D. Moffat, D. Wayner, and R. Wolkov, J. Am. Chem. Soc. **122**, 3548 (2000).

[69] C. Mui, S. Bent, and C. Musgave, J. Phys. Chem. **104**, 2457 (2000).

[70] J. Cho and L. Kleinman, Phys. Rev. B **67**, 201301 (2003).

[71] R. Koneceny and D. Doren, Surf. Sci. **417**, 169 (1998).

[72] J. Yoshinobu, H. Tsuda, M. Onchi, and M. Nishijima, J. Chem. Phys. **87**, 7332 (1987).

[73] F. Rochet, F. Bournel, J.-J. Gallet, G. Dufour, L. Lozzi, and F. Sirotti, J. Phys. Chem. B **106**, 4976 (2002).

[74] Y. Kim, M. Lee, and H. Yeom, Phys. Rev. B **71**, 115311 (2005).

[75] G. Nisbet, C. Lamont, M. Polcik, R. Terborg, D. Sayago, M. Kittel, J. Hoeft, R. Toomes, and D. Woodruff, J. Phys.: Condens. Matter **20**, 304206 (2008).

[76] M. Kong, A. Teplyakov, J. Lyubovitsky, and A. Bent, Surf. Sci. **411**, 286 (1998).

[77] R. Hamers, Nature **412**, 489 (2001).

[78] J. Yoshinobu, Y. Yamashita, F. Yasui, K. Mukai, K. Akagi, S. Tsuneyuki, K. Hamaguchi, S. Machida, M. Nagao, T. Sato, and M. Iwatsuki, Surf. Sci. **417**, 169 (1998).

[79] R. Hamers, J. Hovis, H. L. S. Lee, and J. Shan, J. Phys. Chem. B **101**, 1489 (1997).

[80] S. Machida, K. Hamaguchi, M. Nagao, F. Yasui, K. Mukai, Y. Yamashita, H. Kato, and H. Okuyama, J. Phys. Chem. B **106**, 1691 (2002).

[81] J. Cho and L. Kleinman, Phys. Rev. B **64**, 235420 (2001).

[82] X. Yang, R. Cao, J. Terry, and P.Pianette, J. Vac. Sci. Technol. B **10**, 2013 (1992).

[83] D. Lin, T. Miller, and T. Chiang, Phys. Rev. B **44**, 10719 (1991).

[84] Y. Chen and M. V. Hove, *MSCD-package, Lawrence Berkeley National Laboratory* (http://electron.lbl.gov/mscdpackage.htm, 1998).

[85] R. Doell and M. Hove, Surf. Sci. **355**, 393 (1996).

[86] D. Linde, *Handbook of Chemistry and Physics* (Chemical Rubber Company Roca Raton, 1995).

[87] J. Miwa, B. Eves, F. Rosei, and G. P. Lopinski, J. Phys. Chem. B **109**, 20055 (2005).

[88] Q. Li and K. Leung, Surf. Sci. **541**, 113 (2003).

[89] R. Coustel and N. Witkowski, J. Phys. Chem. C **112**, 14102 (2008).

[90] D. Weier, A. Beimborn, T. Lühr, F. Schönbohm, S. Döring, U. Berges, and C. Westphal, Surf. Sci. (accepted for publication) (2009).

[91] H. Kim and J. Cho, J. Chem. Phys. **120**, 8222 (2004).

Publications

A. de Siervo, C.R. Flüchter, D. Weier, M. Schürmann, S. Dreiner, M.F. Carazzolle, A. Pancotti, R. Landers, G.G. Kleiman, and C. Westphal, *The hafnium silicide formation on Si(100) upon annealing*, Phys. Rev. B **74** (2006) 75319

C.R. Flüchter, A. de Siervo, D. Weier, M. Schürmann, U. Berges, S. Dreiner, M.F. Carazzolle, R. Landers, G.G. Kleiman, and C. Westphal, *Structure analysis of the system Hafnium/Silicon(100) by means of X-ray photoelectron spectroscopy and X-ray photoelectron diffraction (XPD)*, Mater. Sci. Semicond. Process. **9** (2006) 1049

D. Weier, C. Flüchter, A. de Siervo, M. Schürmann, S. Dreiner, U. Berges, M.F. Carazzolle, A. Pancotti, R. Landers, G.G. Kleiman, and C. Westphal, *Photoelectron spectroscopy (XPS) and photoelectron diffraction (XPD) studies on the system hafnium silicide and hafnium oxide on Si(100)*, Mater. Sci. Semicond. Process. **9** (2006) 1055

C.R. Flüchter, A. de Siervo, D. Weier, M. Schürmann, U. Berges, S. Dreiner, M.F. Carazzolle, R. Landers, G.G. Kleiman, and C. Westphal, *Photoelectron diffraction study and structure determination of ultrathin hafnium silicide layers on silicon(100) using Mg K_α radiation and synchrotron light*, J. Electron Spectrosc. Relat. Phenom. **156** (2007) 92

M.F. Carazzolle, M. Schürmann, C.R. Flüchter, D. Weier, U. Berges, A. de Siervo, R. Landers, G.G. Kleiman, and C. Westphal, *Structural and electronic analysis of Hf on Si(111) surface studied by XPS, LEED and XPD*, J. Electron Spectrosc. Relat. Phenom. **156** (2007) 393

C.R. Flüchter, D. Weier, M. Schürmann, U. Berges, S. Döring, and C. Westphal, *Evolution of chemical states within the HfO_2/Si(100) interface upon annealing, prepared by direct electron beam evaporation*, Surf Sci. **602** (2008) 2623

C.R. Flüchter, A. de Siervo, D. Weier, M. Schürmann, A. Beimborn, S. Dreiner, M.F. Carazzolle, R. Landers, G.G. Kleiman, and C. Westphal, *Structure determination of three-dimensional hafnium silicide nano structures on Si(100) by means of x-ray photoelectron diffraction*, Surf. Sci. **602** (2008) 3647

M.F. Carazzolle, C.R. Flüchter, A. de Siervo, D. Weier, R. Landers, G.G. Kleiman, and C. Westphal, *Stability of HfO_2 on Si(100) mediated by Si_3N_4 buffer layers*, J. Appl. Phys. **107** (2010) 1

F. Schönbohm, C.R. Flüchter, D. Weier, U. Berges, S Döring and C. Westphal, *Thermal stability of ultrathin ZrO_2 films and structure determination of $ZrSi_2$ islands on Si(100)*, Phys. Rev. B **80** (2009) 165323

Sven Döring, Frank Schönbohm, Daniel Weier, Felix Lehmkühler, Ulf Berges, Metin Tolan, Charles S. Fadley, and Carsten Westphal, *Standing-wave excited photoemission experiments on $Si/MoSi_2$ multilayer mirrors in the soft x-ray regime: An analytical modeling approach*, J. Appl. Phys. **106** (2009) 124906

D. Weier, T. Lühr, A. Beimborn, F. Schönbohm, S. Döring, U. Berges, and C. Westphal, *Photoelectron spectroscopy (XPS) and photoelectron diffraction (XPD) studies on the local adsorption of cyclopentene on Si(100)*, Surf. Sci. (2009) (accepted for publication)

D. Weier, T. Lühr, A. Beimborn, F. Schönbohm, S. Döring, U. Berges, and C. Westphal, *Structural analysis of the system pyridine/Si(100) by means of photoelectron spectroscopy and photoelectron diffraction*, Phys. Rev. B (2009) (submitted)

Acknowledgments

Zuerst möchte ich mich bei Herrn Prof. Westphal bedanken, der mir die Möglichkeit gegeben hat diese Dissertation innerhalb seiner Arbeitsgruppe durchzuführen. Er hatte, trotz seiner vielfältigen Verpflichtungen für die Arbeitsgruppe, stets ein offenes Ohr für meine Probleme. Außerdem unterstützte er mich mit seiner Fachkenntnis und seinem Sachwissen im experimentellen und theoretischen Bereich bei allen meinen Fragen.

Außerdem geht man Dank an Herrn Prof. Weis, welcher sich freundlicher Weise bereit erklärt hat das Zweitgutachten für diese Arbeit anzufertigen.

Weiterhin möchte ich mich bei allen Mitgliedern der Arbeitsgruppe E1b bedanken, ohne die die erfolgreiche Durchführung dieser Arbeit nicht möglich gewesen wäre. Im speziellen möchte ich mich bei Dr. Mark Schürmann und Dr. Stefan Dreiner bedanken, welche mich zu Beginn meiner Tätigkeit in die experimentelle Welt der Photoelektronenspektroskopie und Photoelektronenbeugung eingeführt haben. Außerdem geht mein Dank an Frank Schönbohm, Axel Beimborn, Sven Döring und Dr. Ulf Berges für die hervorragende Unterstützung während meiner Messzeiten und die anregenden Diskussion zu den Ergebnissen.

Dr. Ulf Berges als zuständiger Beamlinescientist an der Beamline 11 und dem gesamten DELTA Personal möchte ich dafür danken, dass sie es immer irgendwie geschafft haben uns Nutzer mit Synchrotronstahlung zu versorgen, auch wenn sich noch so hohe Hürden aufgetan haben.

Ein besonderer Dank geht an Herrn Dipl.-Phys. Tobias Lühr welcher mir mit seinen Kenntnissen über verschiedene Programmiersprachen, Unix Systemen und Algorithmen sehr geholfen hat. Gemeinsam konnten wir letztendlich sogar den Angriff der Klonkrieger abwehren ;)

Zuletzt möchte ich mich auch noch bei den Leuten außerhalb der Universität besonders bedanken. Besonders hervorzuheben sind hier meine Eltern, welche mir erst die Möglichkeit

des Physikstudiums eröffnet haben und mir in all den Jahren immer mit Hilfe zur Seite gestanden haben. Außerdem bei allen meinen Freuden, welche mir immer wieder gezeigt haben, dass es auch ein interessantes Leben außerhalb der Universität gibt.